

CONSTRUCTION AND COMMISSIONING OF GAS ELECTRON
MULTIPLIER (GEM) DETECTORS IN ADVANCED ASSEMBLY
DESIGN FOR LOW-ENERGY APPLICATIONS AT HIGH RATES
AND ANALYSIS OF GEM DATA FROM THE MUSE EXPERIMENT
AT PSI

A Dissertation

by

SAHARA JESMIN MOHAMMED PREM NAZEER

Submitted to the Graduate College of Hampton University in
partial fulfillment of the requirements for the degree of

DOCTOR OF PHILOSOPHY

August 2023

This dissertation submitted by Sahara Jesmin Mohammed Prem Nazeer in partial fulfillment of the requirements for the degree of Doctor of Philosophy at Hampton University, Hampton, Virginia is hereby approved by the committee under whom the work has been completed.

Michael Kohl, Ph.D.
Committee Chair

José L. Goity, Ph.D.

Paul Guèye, Ph.D.

Al Amin Kabir, Ph.D.

Jerald Dumas, Ph.D.
Dean, The Graduate College

Date

Copyright by

SAHARA JESMIN MOHAMMED PREM NAZEER

2023

ABSTRACT

Construction and commissioning of Gas Electron Multiplier detectors in advanced assembly design and analysis of scattering data from the MUSE experiment at PSI

(August 2023)

Sahara Jesmin Mohammed Prem Nazeer, B.Sc., University of Peradeniya;

Ph.D. Hampton University

Chair of Advisory Committee: Dr. Michael Kohl

The search beyond the Standard Model explores dark matter and a potential fifth force. DarkLight@ARIEL investigates the dark photon as a mediator between ordinary and dark matter. The experiment aims to measure the process $e^-Ta \rightarrow e^-TaX \rightarrow e^-Ta(e^-e^+)$, by detecting a charged lepton pair in the final state. The spectrometers will be instrumented with Gas Electron Multiplier (GEM) detectors with minimal material budget for tracking.

A novel GEM construction technique is employed for fabricating 25 cm x 40 cm GEM detectors, where all layers are mechanically stretched and assembled within a double frame. The dissertation outlines physics motivation, methods, experimental setup, and the role of GEM detectors in DarkLight. A comprehensive discussion on GEM detectors, focusing on the "NS2" technique, including design, parts, assembly, testing, and performance evaluation will be discussed.

The proton has garnered attention due to discrepancies in measuring its charge radius using muonic hydrogen and electron-based methods. The 2010 muonic hydrogen measurement of the proton charge radius $R_p = 0.84184(67)$ fm, showed a significant 7σ discrepancy compared to the previously known value of $R_p = 0.8775(51)$ fm, giving rise to the proton radius puzzle. Through simultaneous measurements of $e - p$ and $\mu - p$ elastic scattering, MUSE facilitates a precise and direct comparison of the

proton radius. The physics background of the proton radius puzzle, measurement techniques, the approach adopted by the MUSE experiment, its significance and the experimental setup will be discussed. Furthermore, the role of GEM detectors, along with an in-depth analysis of their data and efficiency will be discussed and evaluated.

Dedicated to my beloved parents, husband and children.

ACKNOWLEDGEMENTS

I would like to express my sincere gratitude to all those who have supported me throughout my journey of completing this thesis.

First and foremost, I am deeply grateful to my advisor, Dr. Michael Kohl. Not only did he provide guidance and support throughout my research, but he went above and beyond by assisting me in securing two fellowships that greatly contributed to the success of my thesis. His dedication to my academic growth and career development has been truly invaluable. I am particularly thankful to Dr. Kohl for his unwavering support during a challenging periods in my life. His compassion and belief in my abilities played a crucial role in my determination to complete this thesis.

I would also like to extend my gratitude to the members of my thesis committee, Dr. José Goity, Dr. Paul Guèye and Dr. Al Amin Kabir, for their time, support, and constructive feedback. Their contributions have helped me to improve the quality of my research.

I would like to thank the department chair Dr. Jaetae Seo, lecturers at Hampton University Dr. Michael Kohl, Dr. Liguang Tang, Dr. Alberto Accardi, Dr. José Goity, Dr. Eric Christy and Dr. Paul Guèye. Their expertise and dedication in delivering coursework and guiding my learning have been instrumental in shaping my knowledge. I am thankful for their commitment to providing a comprehensive education and fostering an environment of intellectual growth. Also I'd like to thank Department assistants Ms. Edna Hogan-Hilton and Ms. Monique Howard for their support in handling the administrative paperwork.

I am thankful to my colleagues and friends, including Dr. Anusha Liyanage, Dr. Aruni Nadeeshani, Dr. Tongtong Cao, Tanvi Patel, Dr. Bishoy Dongwi, Dr. Ishara Fernando, and all the other friends who have provided me with the motivation and encouragement I needed to complete this project. Their unwavering support has been

invaluable throughout this process, and I deeply appreciate their contributions to my success.

I would also like to extend my thanks to the International Office, specifically Ms. Ebony Majeed, for their support and assistance. Their guidance in navigating the international student requirements and providing resources has been invaluable. Additionally, I would like to express my gratitude to the Graduate College, especially Ms. Kristy Cansler and Ms. Karen Rankin for their assistance with administrative processes and ensuring the smooth operation of the graduate program.

I would like to express my sincere gratitude to Hampton University and Thomas Jefferson National Accelerator Facility for their support and provision of resources and facilities that have been crucial to the successful completion of my research. Additionally, I am grateful to the Department of Energy and the National Science Foundation for their funding and support, which made this research possible.

I would also like to extend my appreciation to the MUSE collaboration and Dark-Light Collaboration for their valuable insights and contributions to my research. The collective efforts and expertise of the collaboration members have enriched my work and expanded its scope.

Finally, I would also like to acknowledge the support and understanding of my family, especially my mom, dad and husband. Their love and encouragement have been a source of strength for me, and I could not have completed this thesis without their support. Despite the demands of this project, they were always there to provide me with the motivation and encouragement I needed to keep going. My beloved sons, Shevin, Shevon, and Shaheen; Your presence in my life has given me the resilience to push through the challenging moments and the strength to finish what I started.

This thesis is a reflection of the collective effort and support of all of these individuals, and I am deeply grateful for their contributions.

TABLE OF CONTENTS

Chapter	Page
ABSTRACT	iv
DEDICATION	vi
ACKNOWLEDGEMENTS	vii
TABLE OF CONTENTS	ix
LIST OF TABLES	xiv
LIST OF FIGURES	xv
1 INTRODUCTION	1
1.1 GEM Detector Construction for DarkLight@ARIEL Experiment . . .	1
1.2 GEM Data Analysis for MUSE Experiment at PSI	3
2 GEM DETECTOR: PRINCIPLES AND FUNCTIONALITY . .	5
2.1 Introduction	5
2.2 Structure of a GEM Detector	6
2.2.1 GEM Foils	7
2.2.2 Readout Plane	10
2.3 Operational Principles	11
2.3.1 Drift, Transfer and Induction Regions	11
2.3.2 Gas Mixture	12
2.3.3 Detector Gain	13
2.4 Electronics and Data Acquisition System	13

Chapter	Page
3 DARKLIGHT@ARIEL EXPERIMENT	15
3.1 Motivation	15
3.2 Physics Background	19
3.3 Projected Scope of DarkLight@ARIEL	20
3.4 Overview of the DarkLight Experiment	22
3.5 Experimental Setup	22
3.5.1 The Electron Accelerator	23
3.5.2 Target	25
3.5.3 Spectrometers	26
3.5.4 GEM Detectors	27
3.5.5 Trigger Hodoscopes	28
3.5.6 DAQ, Trigger Electronics and Slow Control	29
4 CONSTRUCTION AND COMMISSIONING OF GEM DETEC-	
TORS	31
4.1 Introduction	31
4.2 Foil Stretching Techniques	31
4.2.1 Mechanical Stretching Technique	32
4.2.2 Thermal Stretching Technique	33
4.2.3 Drawbacks	34
4.2.4 Self-Stretching Technique	34
4.3 Design	35
4.3.1 GEM Foil	36
4.3.2 Gas Flow	36
4.3.3 High Voltage Supply	37
4.4 Construction	40

Chapter	Page
4.4.1	3D CAD Modeling 40
4.4.2	Preparation 44
4.4.3	Assembly 49
4.4.3.1	Assembly of Inner Stack 50
4.4.3.2	Foil Stretching 64
4.4.3.3	Closing of the Chamber 67
4.5	Electronics, DAQ System and COOKER Framework 71
4.5.1	APV25 72
4.5.2	MPD 73
4.6	Testing and commissioning 75
4.6.1	Gas Leak Testing 75
4.7	Results 77
5	MUSE EXPERIMENT 80
5.1	Motivation 80
5.2	Proton Charge Radius Measurements 83
5.2.1	Elastic Electron-Proton Scattering 83
5.2.2	Upcoming Experiments 85
5.3	Overview of the MUSE Experiment 86
5.4	Experimental Setup 87
5.4.1	PiM1 Beam Line 88
5.4.2	Beamline Detectors 93
5.4.2.1	Beam Hodoscope 93
5.4.2.2	GEM Detector 94
5.4.2.3	Veto Scintillator 97
5.4.2.4	Beam Monitor 98

Chapter	Page
5.4.3 Target	99
5.4.4 Scattered Particle Spectrometer	101
5.4.4.1 Straw Tube Trackers	101
5.4.4.2 Scattered Particle Scintillators	103
6 GEM DATA ANALYSIS FOR MUSE EXPERIMENT	105
6.1 Introduction	105
6.2 Analysis	106
6.3 GEM data pre-processing techniques	107
6.3.1 Common-mode Subtraction	108
6.3.2 Pedestal Subtraction	110
6.3.3 Background Corrected Data	112
6.4 Channel masking	114
6.5 Cross-talk Suppression	116
6.5.1 Identification	117
6.5.2 Suppression	119
6.6 Cluster Finder Algorithms	120
6.7 Detector Alignment Studies	123
6.8 Study of GEM Efficiencies	130
6.8.1 Three GEM vs. Four GEM Configuration	130
6.8.2 Three GEM vs. Four GEM Configuration in the Presence of BH Hits	135
6.9 Results	141
7 CONCLUSION AND DISCUSSION	144
7.1 GEM Detector Construction for DarkLight@ARIEL Experiment . . .	144
7.2 GEM Data Analysis for MUSE Experiment at PSI	146

Chapter	Page
REFERENCES	150
VITA	158

LIST OF TABLES

Table		Page
3.1	Specifications of the Dipole Spectrometers	26
4.1	Table of Technical Data of High Voltage Spring Loaded Pins.	38
5.1	MUSE Kinematics	87
5.2	Detector Requirements for MUSE [1]	104
6.1	Efficiency Values for Low and High Rate Runs for Each Case	141

LIST OF FIGURES

Figure	Page
2.1	Cross-section of a triple-GEM layer detector [2]. 6
2.2	Left: Holes in the GEM foil under optical microscope. Right: Cross section of a GEM hole under electron microscope [2]. 7
2.3	Schematic of a GEM layer showing hole diameters and pitch. 8
2.4	GEM foil production - Left: Double masking technique. Right: Single masking technique [3]. 9
2.5	GEM holes achieved from single mask technique. The first and third pictures show how holes are visible from top and bottom and the second picture shows the cross-section of a hole [4]. 9
2.6	Electric field lines through GEM holes when a voltage is applied across the copper layers [2]. 10
2.7	X-Y pattern readout system with strips and pads. 11
2.8	Electron avalanche through the electric field of triple-GEM detector [5]. 12
2.9	Diagram of GEM readout system. 14
3.1	Standard Model of particle physics. 15
3.2	Composition of the universe - Image courtesy: NASA/CXC/K.Divona. 16
3.3	The s-channel boson may serve as a mediator for the dark sector. 17
3.4	(a): Anomaly in ${}^8\text{Be}$ [6]. (b): Anomaly in ${}^4\text{He}$ [7]. 20
3.5	The projected reaches on a linear plot for three separate data taking runs: 13@31 (dark blue) - a 1000h run at 31 MeV optimized for $m_{A'}$ = 13 MeV; 17@31 (light blue) a 1000h run at 31 MeV optimized for $m_{A'}$ = 17 MeV; 17@45 (light red) a 1000h run at 45 MeV optimized for $m_{A'}$ = 17 MeV; 17@55 (dark red) a 1000h run at 55 MeV optimized for $m_{A'}$ = 17 MeV [8]. 21

Figure	Page
3.6 3D CAD rendering of the experimental setup relative to average person for scale [8].	23
3.7 CAD representation of the proposed experimental layout with top and side views, featuring the scattering chamber, a pair of magnetic spectrometers, and GEM detectors.	24
3.8 Floor plan of the ARIEL e-Linac. Phase one (31 MeV) will be conducted in position A, while phase two (50 MeV) will take place in position B.	24
3.9 Floor plan of the ARIEL e-Linac for the final phase of the DarkLight experiment, with a cryo-module to increase the energy from 31 MeV to 50 MeV, and a septum magnet and RF deflector for concurrent beam delivery to ARIEL and DarkLight.	25
3.10 The figure displays a schematic overview of the spectrometer optics with GEM detectors and trigger hodoscopes. The central momentum, p_0 , is depicted in red, while the colors blue and green correspond to $p_0-20\%$ and $p_0+20\%$, respectively.	27
3.11 The picture shows two fully-equipped GEM elements, including APV frontend electronics, back-planes, adapter boards, and low-voltage regulator board.	28
3.12 Scintillator paddles attached to SiPMs - Image courtesy: Kate Pachal.	29
4.1 Mechanical stretching of 50 x 60 cm ² GEM foils made for a SBS by UVA - Left: Stretched GEM foil using a mechanical system on four sides. Right: Top figure shows the close-up of the mechanical system and bottom figure shows the GEM foil after gluing on to the spacer frame.	32
4.2 Thermal stretching of 30 cm × 30 cm GEM foils made for a muon tomography station by Florida Tech - Left: IR array setup for thermal stretching on an optical bench. Right: GEM foil tensioned at $\sim 40^\circ\text{C}$ [9].	33
4.3 Schematic of self-stretch technique used to build the GEM detector for DarkLight@ARIEL experiment.	35
4.4 Top view of segmented GEM foil with 25 cm × 40 cm active area - credit: Bertrand Mehl, CERN.	36

Figure	Page
4.5 Two main inlets and outlets are shown (green) on corners of the main frame and 6 inlets and 6 outlets are shown (red) on shorter sides of inner frames - credit: Bertrand Mehl, CERN.	37
4.6 High voltage divider system - credit: Bertrand Mehl, CERN.	39
4.7 Ordering of the pins from (1) to (26) from left to right on drift foil attached on inner frame A.	39
4.8 GEM foil top layer (left) and bottom layer (right) - credit: Bertrand Mehl, CERN.	39
4.9 From left to right - Tanvi Patel, Jesmin Nazeer, Rui De Oliveira, Michael Kohl at CERN after assembly of the first detector.	40
4.10 Schematic of triple layer GEM assembly for DarkLight@ARIEL - Credit: Bertrand Mehl, CERN.	41
4.11 Drift foil, 3 GEM foils and readout board sandwiched between the inner frames from A to F.	42
4.12 Outer frame providing mechanical tension with screws through embedded nuts inside the inner frames for GEM foil stretching.	43
4.13 Final GEM chamber closed with top and bottom gas window covers.	43
4.14 Pre-stretched GEM foils being cleaned to remove dust particles from the surface using a tacky roller.	45
4.15 The performance of pre-stretched GEM foils at high voltages is being tested using the Megger MIT430/2 insulation tester.	45
4.16 Top side of top cover with holes for inlay nuts (Left) and inlay nuts were hammered into the top gas window foil (Right).	46
4.17 Top side of top cover with fixed inlay nuts (Left) and bottom side of top cover with embedded o-ring (Right).	47
4.18 Prepared adhesive side of inner frame A with embedded nuts for vertical screws (Left) and Inner frames B-E (Right).	48
4.19 Hammering of inlay nuts into the inner frame A (Left) and non-adhesive side of prepared frame A (Right).	48

Figure	Page
4.20 Soldering of wires to the HV connections on RO board (Left) Pre-stretched, prepared and cleaned RO board (Right).	49
4.21 Cleaning the Plexiglas base with a piece of anti-static tacky cloth.	50
4.22 Placing dowel pins for alignment and setting up inner frame A. . .	51
4.23 Extra holes on one side of inner frame A bar and on the drift foil for HV connections.	51
4.24 Test fitting drift layer on inner frame A bars and removing adhesive sticker from the inner frame A.	52
4.25 Tacky roller (left) and cleaning of the drift foil using tacky roller.	53
4.26 Placing the drift foil onto the frames while on green canvas and adjusting and pre-stretching the drift foil using green tape	54
4.27 Pressing down the drift foil onto the adhesive strips using the tacky cloth and cleaning the drift foil using tacky roller after final pre-stretching.	55
4.28 Fixing the spring loaded pins for HV connections and carefully soldering them to the drift foil.	56
4.29 Drift foil with all the spring loaded pins attached.	56
4.30 Placing inner frame B on the drift foil.	57
4.31 Testing the G1 foil and stretching it on the inner frames B.	58
4.32 Keep the foil connections for hv connections for G1T and G1B layers and cut-off other marked holes.	58
4.33 Testing connection between hv spring loaded pins is conducted after each layer of foil is stacked.	59
4.34 Placing the inner frames C on G1 foil and pre-stretching G2 GEM foil.	60
4.35 Keep the foil connections for hv connections for G2T and G2B layers and cut-off other marked holes.	60
4.36 Inserting T-nuts through inner frames C and B.	61
4.37 Placing inner frames D and pre-stretching of G3 GEM foil.	61

Figure	Page
4.38 Cleaning the active side of Readout board and placing it on the inner frames E.	62
4.39 Placing inner frames F and pre-stretching the readout board.	63
4.40 Tightening the screws through inner frames E - A and fixing the whole stack.	63
4.41 Flip the whole stack and test all the layers for electrical connections.	64
4.42 The GEM foil stack after cutting off excess foil.	65
4.43 The GEM foil stack after cutting off excess foil and after placing the outer frame.	65
4.44 Stretching of the foils by tightening the horizontal screws	66
4.45 The GEM foil stack before stretching.	66
4.46 The GEM foil stack after stretching.	67
4.47 The gas inlets/outlets through short bars of inner frames (Left), O-ring pieces are placed to ensure gas flows through active area (Right).	68
4.48 Cleaning the top cover and drift foil using tacky roller and placing the cover on GEM stack.	68
4.49 Cleaning the bottom cover and readout layer using tacky roller and placing the cover on RO layer.	69
4.50 Closing the chamber by inserting screws through bottom cover.	70
4.51 Placement of M6 screws through openings where horizontal screws sit (Left).	70
4.52 Fully closed GEM detector.	71
4.53 Readout system of GEM detector.	72
4.54 APV Frontend (INFN Geneva - Rev 4.11 Oct 2014) front and back.	73
4.55 APV Frontend card on GEM 4 slot backplane (Rev3).	73
4.56 MPD Rev3.0 (Left); MPD Rev4.0 (Right).	74
4.57 Block diagram for MPD Rev 4.0.	75

Figure	Page
4.58 The potential gas leak openings were sealed using epoxy.	77
4.59 The positioning of the GEM detectors at ULQ2@ELPH experiment during 2019 beam time.	78
4.60 The cluster distribution of GEM detectors for focused beam and de-focused beam.	79
5.1 Proton radius measurements over the years of 2010-2020 using electron scattering and spectroscopic measurements shown with CODATA compilations [10–17] - Image courtesy: Jan C. Bernauer.	83
5.2 MUSE Apparatus implemented by MUSE Geant4 simulation - Image courtesy: Steffen Strauch.	88
5.3 Main components of PiM1 beamline [1].	89
5.4 Measured RF time spectrum for negative charge beams with momenta of 117.5 MeV/c, 160 MeV/c, and 210 MeV/c, at a distance of ≈ 23.5 m from the production target [1].	91
5.5 Measured RF time spectrum for positive (top) and negative (bottom) charge beams with momenta of 115.29 MeV/c.	92
5.6 Beam hodospoe - Plance C.	93
5.7 10 cm x 10 cm triple-layer GEM detectors built by Hampton University.	95
5.8 GEM hit maps of the beam [18].	97
5.9 Schematic of beam veto detector (Left) and installed veto detector at PSI looking upstream (Right).	98
5.10 Beam monitor at PSI in production data configuration setup.	99
5.11 Schematic of scattering chamber (Left) and target ladder (Right).	101
5.12 CAD drawing of the four STT chambers mounted on a table. The straws are depicted in light gray color, while the HV/readout cards are in dark gray (Left) and installed STT chamber at PSI (Right) [1].	102
5.13 Scattered Particle Scintillator.	104

Figure	Page
6.1 ADC spectrum of US GEM plane before implementing noise subtraction routine for x-axis (left) and y-axis (right).	108
6.2 ADC spectrum of US GEM plane after subtracting common mode for x-axis (left) and y-axis (right).	109
6.3 ADC spectrum of US GEM plane after pedestal subtraction for x-axis (left) and y-axis (right).	112
6.4 ADC spectrum of US GEM plane after subtracting common-mode noise and pedestal for x-axis (left) and y-axis (right).	113
6.5 Distribution of hit counts for each strip along the X-axis of the US GEM detector.	115
6.6 Common-mode and pedestal subtracted ADC distribution of X-axis of US GEM (left) Vs. flagged hot channels in the same ADC distribution (right).	116
6.7 Example plot of correlation coefficient values of r_{xy} for 3rd APV card of MS GEM element. The values filled indicate the strength of correlation between ch_i and ch_j within the same APV card.	119
6.8 Histogram of cluster distribution map for US GEM element - using CENsus method (left) and K-Means clustering method (right).	123
6.9 The horizontal and vertical cross-hairs on a GEM plane is visually emphasized with a purple circular outline.	125
6.10 A visual representation illustrating the measurements conducted to obtain x, y, and z positions. The figure showcases the survey employed to calculate the precise coordinates of observed points in 3D space.	126
6.11 A picture illustrating the use of a handheld device for obtaining spatial coordinates of multiple points on a Kapton layer.	126
6.12 A figure illustrating a sequence of frames from left to right: local frame, telescope frame, and MUSE frame.	127
6.13 Geant4 illustration of the local frame and telescope frame in relation to the MUSE target. The illustration depicts the coordinate orientation, where the z-axis aligns with the beam direction, the y-axis points upwards, and the x-axis extends out of the plane.	128

Figure	Page
6.14 The histograms displaying track residuals of a 3 GEM setup before (blue) and after (red) alignment procedures along the X and Y axes for the US, 4TH, and MS GEMs highlighting the improved alignment accuracy achieved through the alignment procedures, validating the successful transformation of coordinates across the different frames of reference	129
6.15 Schematic representation of a hit passing through gem detector setup consisting of three planes and a track formed by two detectors projected onto the third plane. Residuals between the measured positions of the track and the expected positions are examined for precise track reconstruction.	131
6.16 Efficiency of US, 4TH and MS planes for 2 of 3 GEMs; Low rate run 100 kHz, 100k events.	132
6.17 Schematic representation of a hit passing through gem detector setup consisting of four planes and a track formed by three detectors projected onto the fourth plane. Residuals between the measured positions of the track and the expected positions are examined for precise track reconstruction.	134
6.18 Efficiency of US, 4TH, MS and DS planes for 3 of 4 GEMs; Low rate run 100 kHz, 100k events.	135
6.19 Schematic illustrating a hit passing through 3 GEM detector planes with the condition that the particle had passed through BH planes when in-time hits = 1.	136
6.20 Efficiency of US, 4TH and MS planes for 2 of 3 GEMs with BH; Low rate run 100 kHz, 100k events	136
6.21 Schematic illustrating a hit passing through 4 GEM detector planes with the condition that the particle had passed through BH planes when in-time hits = 1.	137
6.22 Efficiency of US, 4TH, MS and DS planes for 3-of-4 GEMs with BH; Low rate run 100 kHz, 100k events	137
6.23 Correlation between actual hit position and projected hit position of Beam Hodoscope plane 2; Low rate run 100 kHz, 100k events	138
6.24 Correlation between actual hit position and projected hit position of Beam Hodoscope plane 3; Low rate run 100 kHz, 100k events	138

Figure	Page
6.25 Efficiency of US, 4TH, MS and DS planes for 2 of 3 GEMs; High rate run 2.2 MHz, 100k events.	139
6.26 Efficiency of US, 4TH and MS planes for 2 of 3 GEMs with BH; High rate run 2.2 MHz, 100k events.	139
6.27 Efficiency of US, 4TH, MS and DS planes for 3 of 4 GEMs; High rate run 2.2 MHz, 100k events.	140
6.28 Efficiency of US, 4TH, MS and DS planes for 3 of 4 GEMs with BH; High rate run 2.2 MHz, 100k events.	140

CHAPTER 1

INTRODUCTION

1.1 GEM Detector Construction for DarkLight@ARIEL Experiment

The Standard Model explains subatomic particles and interactions, but not all mysteries. Dark matter constitutes 27% of the universe, yet remains invisible. A mediator, the dark photon or A' , could interact with ordinary and dark matter. DarkLight@ARIEL experiment investigates a hypothetical particle using an electron beam at ARIEL facility, TRIUMF, Canada to understand the fifth force and dark matter.

The X17 particle, a hypothetical mediator of the fifth force, has gained significant attention due to various unexplained phenomena observed in recent experiments. Anomalous results in the decay of excited ^8Be and ^4He atoms have hinted at the presence of a new particle with a mass of around $17 \text{ MeV}/c^2$. These experimental findings, coupled with the deviation in the muon's magnetic moment ($g_\mu - 2$) from the predicted value, have piqued the interest of physicists in the existence of a new force carrier. The DarkLight experiment aims to explore this possibility further by utilizing the ARIEL e-linac's high-energy electron beam to investigate the interaction between the proposed protophobic boson and ordinary matter. By colliding the electron beam with a tantalum target, DarkLight seeks to shed light on the nature of dark matter and potentially discover evidence of the fifth force.

The projected scope of DarkLight@ARIEL encompasses a comprehensive investigation of the proposed fifth force parameter space. The experiment's sensitivity is

evaluated by integrating the background over the expected signal width and calculating the coupling strength required for the signal to exceed a 2σ fluctuation of the background. With 1000 hours of beam time, DarkLight@ARIEL aims to explore the upper portion of the parameter space for the fifth force. The experiment's anticipated reach is depicted in a plot, demonstrating the achievable range for different beam energies and mediator masses. By focusing on the 17 MeV region, DarkLight has the potential to discover the proposed particle or place stringent limits on its interaction with normal matter, contributing to our understanding of the fundamental forces and the enigmatic realm of dark matter.

In Chapter 2, a comprehensive introduction to GEM detectors is presented. The chapter begins by delving into the historical background of GEM detectors, highlighting their development and evolution over time. It explores the advantages and unique features that make GEM detectors stand out among other particle tracking detectors. The working principles of GEM detectors are thoroughly explained, providing insights into how they operate and interact with particles. The chapter covers the fundamental concepts and mechanisms that drive the functionality of GEM detectors. Additionally, the characteristics of GEM detectors are discussed, addressing factors such as their spatial resolution, energy resolution, detection efficiency, and noise performance.

The Chapter 3 will discuss anomalies and other experimental observations related to the hypothetical X17 particle. It will then delve into the physics motivation behind the DarkLight experiment, highlighting its significance and the purpose of utilizing gem detectors as particle trackers.

Chapter 4 delves into the history of gem detector foil stretching techniques, highlighting their drawbacks and emphasizing the uniqueness and significance of the self-stretching technique. The chapter also covers the preparation for detector construction, including the methods employed and testing procedures. Furthermore, it

addresses the challenges encountered during the process and details the solutions implemented to overcome them. Lastly, the chapter presents the initial commissioning results of the constructed detectors.

1.2 GEM Data Analysis for MUSE Experiment at PSI

The proton, discovered by Ernest Rutherford in 1917, is a composite particle composed of three quarks bound by gluons. Its internal structure has led to investigations of properties like angular momentum and charge radius. The root-mean-square charge radius $R_p \equiv \sqrt{\langle r^2 \rangle}$, representing the spatial extent of the proton's charge distribution, has garnered attention due to discrepancies between measurements from muonic hydrogen and electron-based methods.

Hydrogen, with a single proton and an orbiting electron, is an ideal system for studying the proton's charge radius. Hofstadter's 1956 electron-proton scattering experiment provided the first measurement [19]. Two primary approaches were used until 2010: nuclear scattering and spectroscopy. Scattering experiments involved high-energy electrons interacting with hydrogen atoms, while spectroscopy used energy levels to calculate the radius. Both methods yielded consistent results [20].

A precise 2010 measurement of the proton charge radius using muonic hydrogen Lamb shift determined a value of 0.84184(67) fm, 4% smaller and 10 times more precise than the previous CODATA-2010 value. The significant discrepancy between electronic and muonic measurements, a 7σ difference, gave rise to the proton radius puzzle.

Presently, no existing data offers the required precision to unravel the mystery surrounding the proton's radius through $\mu - p$ scattering. The MUSE experiment aims to address this challenge by simultaneously measuring the elastic scattering cross-sections of $\mu^\pm p$ and $e^\pm p$. This simultaneous measurement enables a direct and highly precise comparison between $e - p$ and $\mu - p$ elastic scattering at sub-percent

levels, surpassing the previous limitations at lower values of Q^2 . Additionally, by examining cross-section differences between positively and negatively charged particles, the MUSE experiment will scrutinize the effects of two-photon exchange (TPE) at sub-percent levels with unprecedented accuracy.

Chapter 5 will discuss the origins of the proton radius puzzle, alternative experimental approaches, and the significance of the MUSE experiment. This chapter will also delve into the experimental methods employed, providing detailed insights into the detector setup and the overall approach adopted in the MUSE experiment.

Turning attention to Chapter 6, the focus will shift towards the importance of Gas Electron Multiplier (GEM) detectors within the MUSE setup. The chapter will delve into detailed aspects of GEM data analysis and explore the efficiency analysis associated with these detectors. By delving into the details of data analysis and efficiency studies, this chapter aims to provide a comprehensive understanding of the role of GEM detectors in the MUSE experiment.

In Chapter 7, the thesis will reach its conclusion by providing a comprehensive summary of the research efforts undertaken throughout the study. This final chapter will encompass an overview of the work conducted, presenting the achieved results and their significance, highlighting the contributions made and paving the way for future investigations and developments. Additionally, it will include a discussion on the future prospects that lie ahead, offering insights into potential avenues for further exploration and advancement in the field.

CHAPTER 2

GEM DETECTOR: PRINCIPLES AND FUNCTIONALITY

2.1 Introduction

Gas Electron Multiplier (GEM) detectors were first invented by Fabio Sauli in 1996 at CERN, the European Organization for Nuclear Research [21]. There are three basic types of gaseous ionization detectors characterized by the amount of voltage applied to the detector: ionization chambers, proportional counters, and Geiger-Muller tubes. GEM detectors belong to the category of proportional counters. These detectors generate electron avalanches at higher voltages, resulting in a current pulse that is proportional to the energy deposited by radiation. This characteristic allows for accurate measurement of the energy of incident particles in the detector.

Wire chambers and gas electron multiplier detectors are widely used proportional counters. In comparison to Multi-Wire Proportional Counters (MWPCs), GEM detectors have proven to be cost-effective in terms of manufacturing, maintenance, and repair. MWPCs have several disadvantages, including limitations in spatial resolution, energy deposition on the anode wires leading to efficiency loss over time, a decrease in gain at high beam rates, and the fragile of large area detectors.

Therefore, GEM detectors offer several key advantages. This include improved time and spatial resolution, radiation hardness, stability at high beam rates, granularity, and design flexibility. GEM detectors are also classified as Micro Pattern Gaseous Detectors (MPGDs) due to the sub-millimeter distance between the anode and cathode.

Overall, GEM detectors provide superior performance and overcome the limitations associated with MWPCs, making them a preferred choice for various applications requiring precise and reliable detection capabilities.

This chapter will discuss the details of a typical GEM detector, main characteristics of the design, working principles and usage of GEM detectors for particle tracking.

2.2 Structure of a GEM Detector

A triple layer GEM detector consists of a drift cathode, 3 GEM foils and a anode PCB readout plane sequentially arranged in a rigid frame as shown in Figure 2.1. This assembly is covered by top and bottom windows for gas tightness and only have openings for gas inlet and outlet for the purpose of gas distribution.

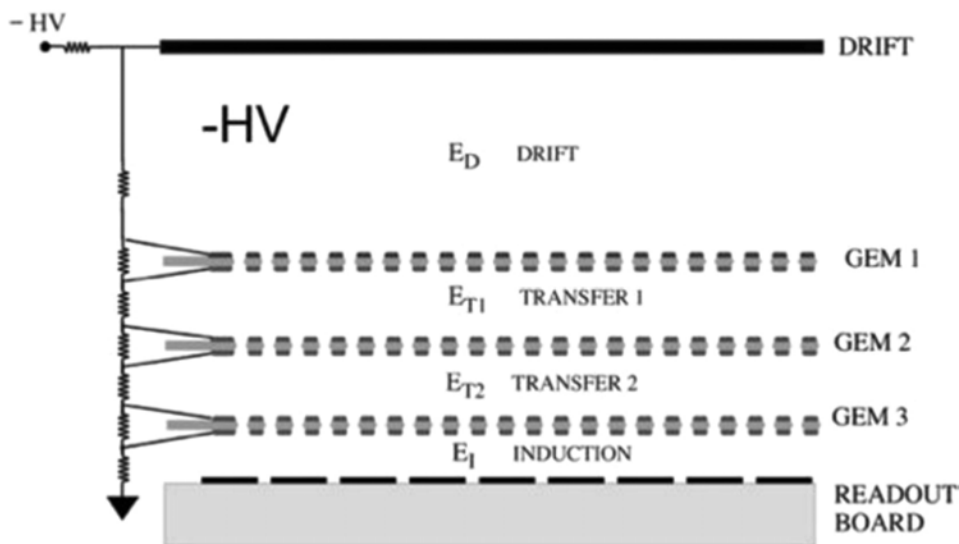


Figure 2.1. Cross-section of a triple-GEM layer detector [2].

Three separate regions can be defined as drift region, transfer region and induction region. The amplification process is independent from the readout structure ensuring the flexibility to use different readout patterns. The drift gap has a thickness of 3mm and there are 2mm gaps between each transfer region and induction region. A resistance scheme is set up using a single voltage source to distribute suitable voltages

to all electrodes. In this section, we will discuss about the principle components of a triple-layer GEM detector.

2.2.1 GEM Foils

GEM foil is the main component of a GEM detector. It is made out of a Kapton foil clad on copper on both sides. Kapton is an insulating dielectric medium and copper is a conducting medium. The thickness of the two copper layers are about $5\ \mu\text{m}$ each and Kapton thickness is about $50\ \mu\text{m}$. A condensed array of holes are etched into a GEM foil using a process called photolithography and acid etching. As shown in Figure 2.2 and Figure 2.3, the holes have an inner diameter of $50\ \mu\text{m}$, outer diameter of $70\ \mu\text{m}$ and a pitch of about $140\ \mu\text{m}$.

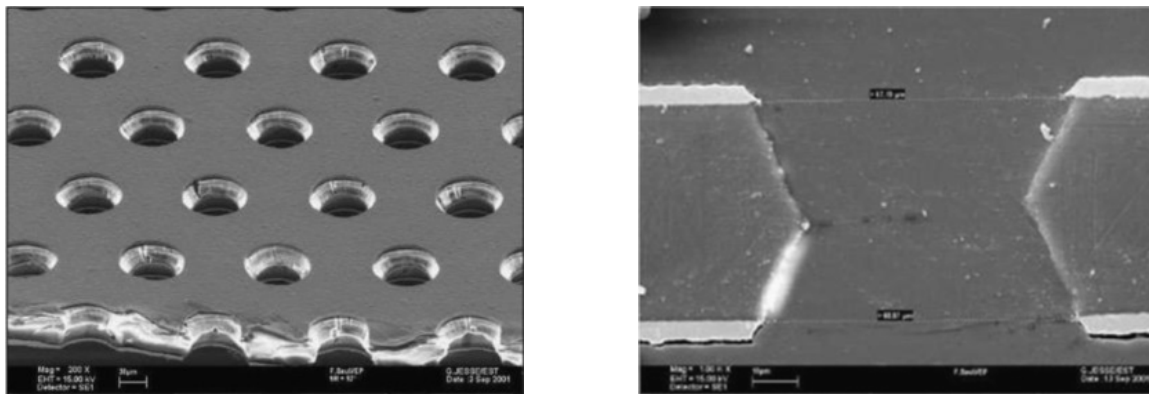


Figure 2.2. Left: Holes in the GEM foil under optical microscope. Right: Cross section of a GEM hole under electron microscope [2].

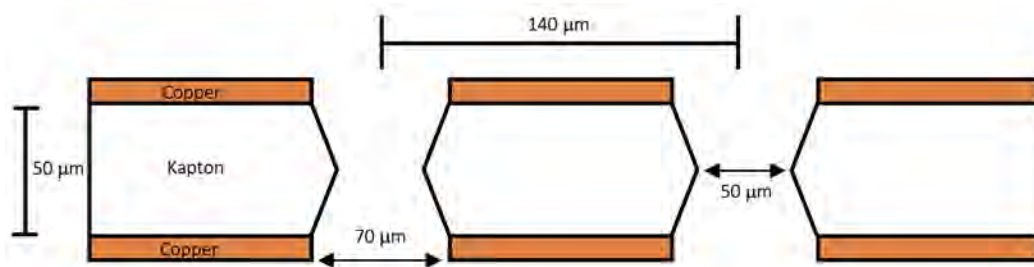


Figure 2.3. Schematic of a GEM layer showing hole diameters and pitch.

The etching process determines the shape of the GEM holes. Initial GEM foil production used a double masking technique. As shown in Figure 2.4, the process begins with a coating of photo-resist (a light-sensitive material) on both sides of the raw material, then first masking followed by exposure to UV light. After that etching of copper and Kapton is performed finishing with second round of masking, etching and cleaning. This introduces the double conical "hourglass" shape to the GEM holes (Figure 2.2). Major drawback of the double mask technique is that it limits GEM foil size to $40 \text{ cm} \times 40 \text{ cm}$. The standard double-mask technique for producing GEM foils was not proven to be ideal for large size GEM foils since it resulted in alignment problems between the two masks on either side of the foil during the photo-lithographic hole etching step. Later single mask etching technique was developed and currently is being used to fabricate GEM foils [4]. This technique involves the same steps as double masking but masking and etching is done only once, shown in Figure 2.4. This introduces a cylindrical shape to the GEM holes, shown in the Figure 2.5. The development of single mask technique allowed the production of large size GEM foils.

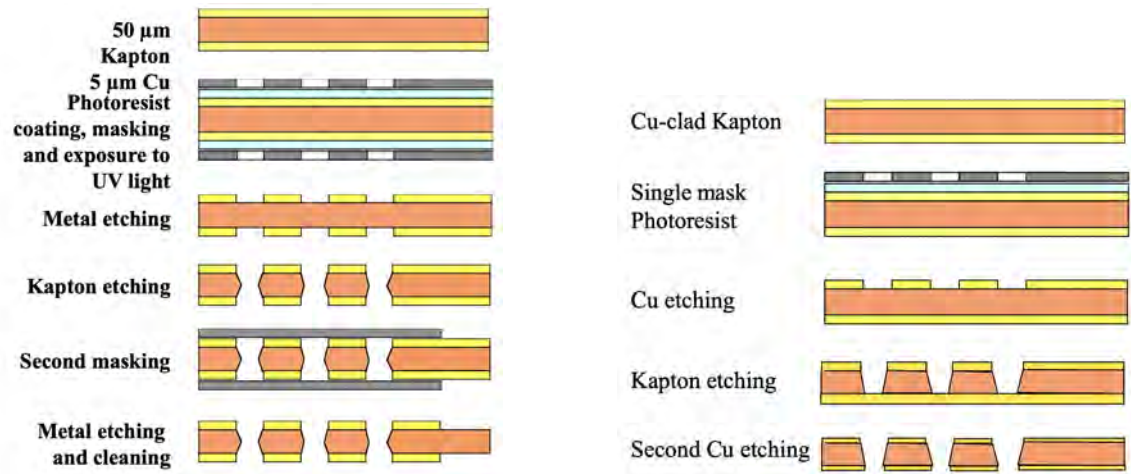


Figure 2.4. GEM foil production - Left: Double masking technique. Right: Single masking technique [3].

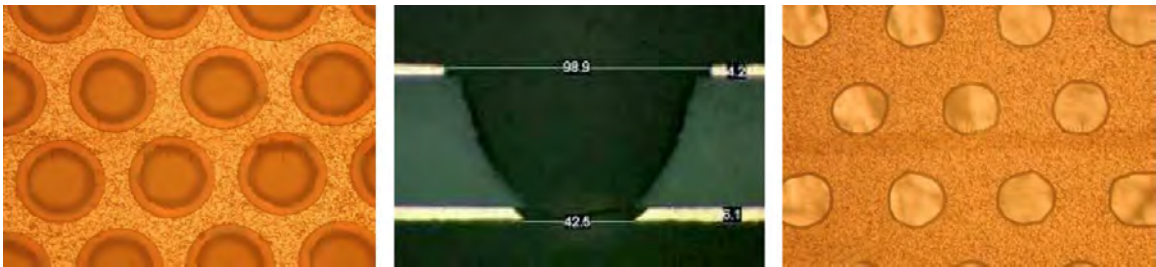


Figure 2.5. GEM holes achieved from single mask technique. The first and third pictures show how holes are visible from top and bottom and the second picture shows the cross-section of a hole [4].

When an electric potential difference of a few hundred volts is applied across the two copper layers of the GEM foil it will create a very strong electric field in the holes as shown in Figure 2.6.

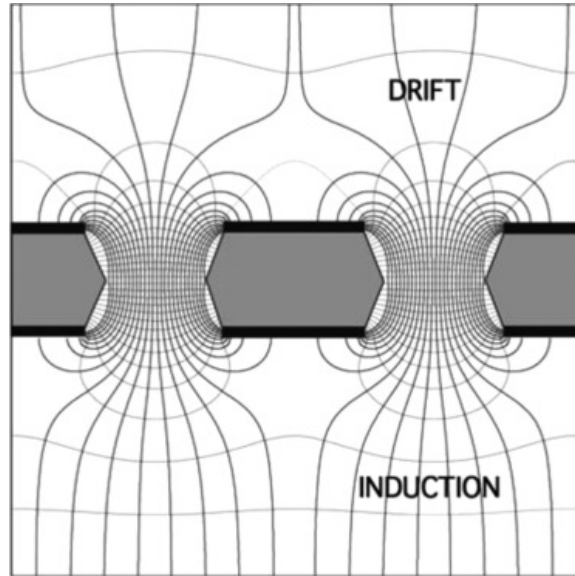


Figure 2.6. Electric field lines through GEM holes when a voltage is applied across the copper layers [2].

2.2.2 Readout Plane

For the GEM detectors used in MUSE experiment and for the newly built GEM detectors a same readout pattern is used. It is a 2D Cartesian stripe readout system set at ground level. The electrodes are made using a similar technology to the one used for GEMs. A layer of $50\ \mu\text{m}$ Kapton with engraved $5\ \mu\text{m}$ thick copper strips on each side is glued on to a rigid support board as shown in Figure 2.7. The pitch of the strips are $400\ \mu\text{m}$. Strip widths are optimized for each set so that the final signal sizes for given hits are the same on both axes. The signals that are collected on the strips are amplified and processed using the APV-25 chip before they are sent to be digitized and recorded using the Multi Purpose Digitizer (MPD) which will be further discussed in section 4.5.

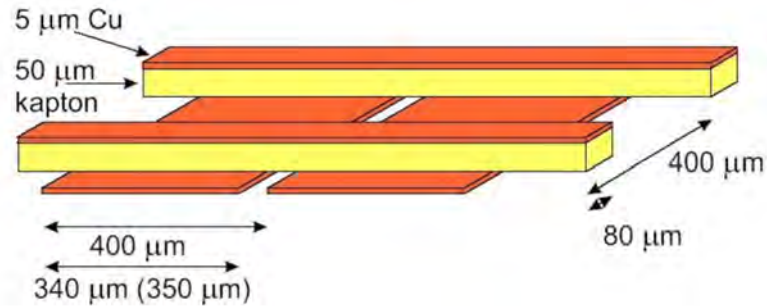


Figure 2.7. X-Y pattern readout system with strips and pads.

2.3 Operational Principles

2.3.1 Drift, Transfer and Induction Regions

In the drift region, ionization occurs when a charged particle enters into the electric field. As the charged particle interacts with the atoms of the supplied gas mixture it produces electrons which are then drifted through the electric field towards the holes. As shown in Figure 2.6, the electric field lines are quite dense inside the GEM holes. This high electric field further accelerates the electrons and collide with more atoms. In the transfer region, a chain reaction is set off as a result of this, which releases additional electrons that accelerate and collide with further atoms releasing more electrons. This process is called electron avalanche. Following amplification, in the induction region the electrons continue to drift towards the readout board. Signals are induced in the readout strips, which generate pulses that can be detected by electronics attached to the readout board. For a triple-GEM detector, a charged particle's behaviour is shown in Figure 2.8 through drift, transfer and induction regions.

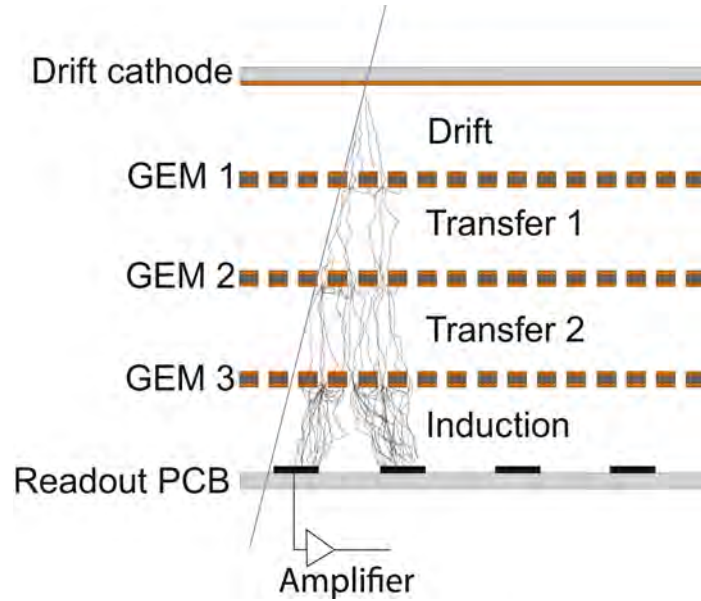


Figure 2.8. Electron avalanche through the electric field of triple-GEM detector [5].

2.3.2 Gas Mixture

It is important to choose an appropriate ionizing gas mixture for the detector. Generally Ar/CO₂ is used in the ratio of 70:30, 75:25 or in some cases 80:20. The ionizing agent is argon while CO₂ is used as quenching gas. When a charged particle gains enough energy and collides with argon atom in the medium it will knock of an electron from the outer most shell of argon atom and will produce a free electron and a positive ion. This is called primary ionization. These free electrons will gain energy and ionize more argon atoms and called secondary ionization process. This amplification of electrons is called gas amplification and continues as a chain reaction and electron avalanche takes place. Gas amplification is proportional to the voltage applied between cathode and anode. This shower of electrons create a signal large enough to be amplified by the electronics. It is necessary for the gas mixture to be well quenched in order to avoid secondary effects such as photon feedback. Excited argon atoms can decay under photon emission and these photons are absorbed by the quencher.

2.3.3 Detector Gain

The gain of the detector is defined as the ratio of the total number of electrons detected on the readout to the total number of primary ionizations produced by the incident particle. A typical triple-GEM detector will produce a gain of 10^4 . The gain of the detector depends on the applied voltage across the GEM foils, hole geometry, and the gas mixture. To maximize the gain factor, the recombination effect must be minimized. Recombination effect refers to the recombination of positive and negative ions, resulting in the creation of neutral atoms. This effect can be reduced by selecting a suitable voltage across the detector and using an appropriate gas mixture.

2.4 Electronics and Data Acquisition System

Depending on the experiment, different types of electronics can be used. In the context of the MUSE experiment, each GEM layer is readout with 4 APV25 frontend cards, 2 of each are connected to X and Y axes. As shown in Figure 2.9, the APV25 cards are powered with low voltage system of +5V and the signals are transferred through HDMI cables to the MPD module. The APV25 frontend cards can readout 128 channels. 250 channels are present in each coordinate axes and a total of 500 channels are read out from each GEM plane. Each APV sends 12 bit ADC data words combined with slow control data to the VME based MPD module. The conversion of analog waveforms to digital values is carried out by Multi Purpose Digitizers (MPDs). The processed signals and are then carried out to the DAQ system.

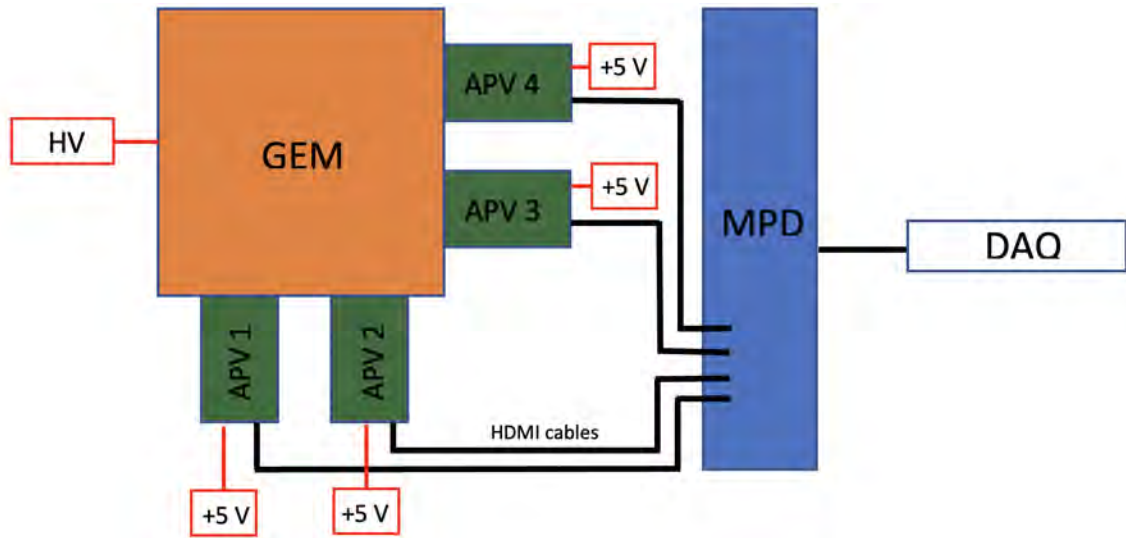


Figure 2.9. Diagram of GEM readout system.

For further details regarding the electronics, Data Acquisition (DAQ) system, and software used in the setup, please refer to Section 4.5. This section provides comprehensive information on the specific components and configurations of the electronics system, as well as software framework.

CHAPTER 3

DARKLIGHT@ARIEL EXPERIMENT

3.1 Motivation

The Standard Model (SM) of particle physics would delve into the fascinating and complex field of subatomic particles, and how they interact with each other under the influence of the four fundamental forces: the strong, electromagnetic, weak, and gravitational forces. Although the Standard Model (SM) of particle physics is a highly successful framework for understanding the behavior of subatomic particles, it is not without its limitations. Some of the most intriguing and perplexing mysteries in modern physics remain unexplained by the SM.

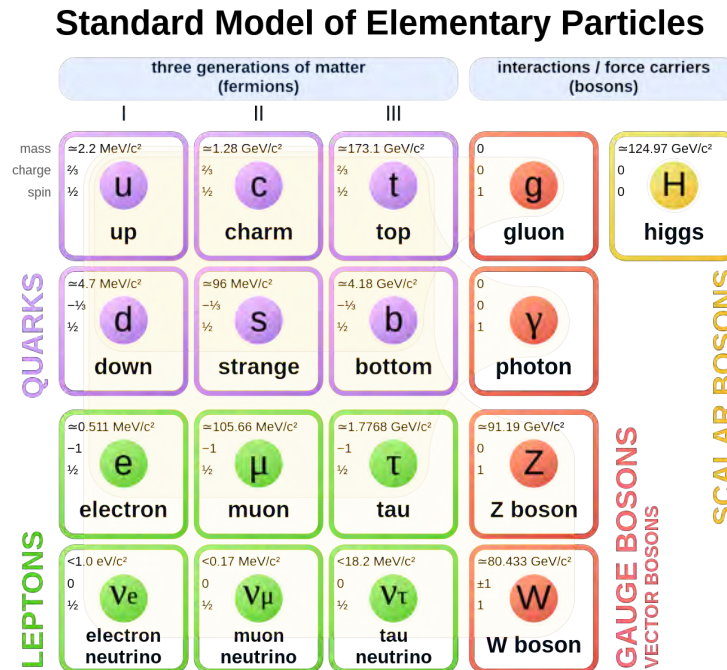


Figure 3.1. Standard Model of particle physics.

One of these mysteries is the existence of Dark Matter (DM), a type of matter that is not visible to telescopes or other instruments that detect electromagnetic radiation. Dark matter makes up $\approx 27\%$ of the total matter in the universe, but its nature and properties remain unknown. Researchers are actively searching for evidence of DM using a variety of experimental techniques, including particle colliders, astronomical observations, and underground detectors.

Depicted in Figure 3.2 the majority of the universe is shrouded in darkness, with normal matter - consisting of protons, neutrons, and electrons that make up everything from stars to planets and even ourselves - comprising a mere 5% of its total mass and energy. Recent estimates from 2017 suggest that dark matter, detected indirectly through its gravitational pull on surrounding matter, makes up 26% of the Universe, while dark energy, a mysterious force believed to be driving the Universe's accelerating expansion, accounts for a staggering 69%. Although telescopes are capable of detecting normal matter directly, only a small portion of it can be observed - about 85%, in the form of hot, intergalactic gas detected through Chandra observations of galaxy clusters. The precise composition of the Universe is still the subject of ongoing research and debate among scientists.

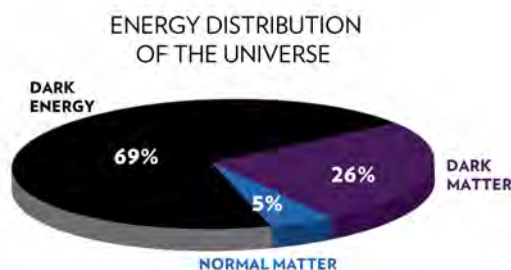


Figure 3.2. Composition of the universe - Image courtesy: NASA/CXC/K.Divona.

In the pursuit of understanding dark matter, an experimental approach is to investigate the existence of a mediator for a potential new interaction between our

observable world - which is explained through the four fundamental forces of gravity, electricity and magnetism, nuclear force, and weak force - and the domain of dark matter. This hypothesized fifth force is yet to be discovered. The dark photon, also known as A' , is a prime candidate for being the mediator of this interaction, as it is believed to couple with known particles through their electric charges. This mediator can decay in two ways: (a) visible decays - decay into detectable particles that are being actively searched for, or (b) invisible decays - decay into undetectable dark-sector particles, whose existence can only be inferred by observing significant missing energy and momentum in the final-state. These two decay modes are important for understanding the properties of the dark photon and the ways in which it interacts with regular and dark matter particles. Depending on the relative couplings and masses of particles in the Standard Model versus those in the dark sector, visible decays can dominate.

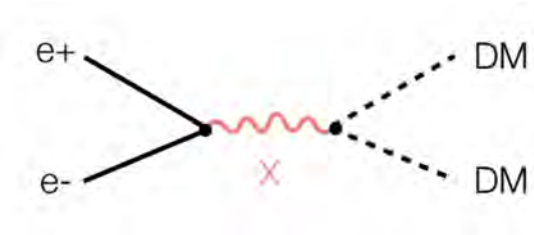


Figure 3.3. The s-channel boson may serve as a mediator for the dark sector.

X17 Particle

In recent research in particle physics, there has been a significant emphasis on a mediator that could potentially be a fifth force with a mass in the range 10 to 100 MeV. There have been several unexplained phenomena that suggest the possible existence of a new force carrier, which is referred to as X17. One such phenomenon is the anomalous magnetic moment of the muon ($g_{\mu}-2$), which is a discrepancy in

measurement of how strongly the muon interacts with magnetic fields [22]. The experimental results show a deviation of 4.2σ between the SM predicted value and observed value of magnetic moment of muon. The introduction of a dark photon with universal couplings offers a viable explanation for the observed discrepancy in the muon's magnetic moment.

Moreover, anomalies in the decay signatures of ^8Be and ^4He have also sparked interest in the possibility of X17 particle [6, 7]. These anomalies suggest that there may be a previously unknown particle with a mass of around $17 \text{ MeV}/c^2$, which could act as a mediator of a fifth fundamental force. Additionally, it is worth noting that the so-called "X17" anomaly originated from the Hungarian Be-8 experiment and was subsequently interpreted by Feng as a light boson with selective (protophobic) couplings [23, 24]. This interpretation of the anomaly provides an alternative perspective, indicating the potential existence of a light boson specially coupled to leptons.

The DarkLight experiment is a recent research initiative aimed at exploring the possibility of a fifth force carrier in the form of a protophobic boson. As discussed above, this hypothetical particle gained attention due to anomalies observed in recent experiments conducted by the Institute of Nuclear Research (ATOMKI) in Hungary [6, 7]. ATOMKI's experiments have produced data suggesting the existence of a new type of particle with a mass of $17 \text{ MeV}/c^2$, which could potentially be explained by the presence of a protophobic boson. The DarkLight experiment is designed to investigate this possibility further by using a high-intensity electron beam to search for interactions between the boson and ordinary matter. It will employ a 31 MeV electron beam, generated by the Advanced Rare Isotope Laboratory (ARIEL) e-linac at TRIUMF, to collide with a tantalum target to investigate the nature of dark matter.

3.2 Physics Background

The X17 particle is a hypothetical particle that was first proposed in 2016 by a team of Hungarian physicists led by Attila Krasznahorkay [6]. The team was studying the decay of excited ${}^8\text{Be}$ atoms, which were bombarded with protons in order to create a high-energy, unstable state. When they fired protons at a thin target of ${}^7\text{Li}$, the unstable excited ${}^8\text{Be}$ state decayed by emitting pairs of electrons and positrons. The team observed an unexpected excess of electron-positron pairs emitted at a specific angle. While the number of observed pairs should drop as the the angle separating the trajectory of the e^- and e^+ increases, the Hungarian group stated that they see a 'bump' at about 140° where there's an significant increase in such emissions corresponding to 17 MeV of invariant mass of the e^-e^+ pair. This was elucidated as the creation/decay of an intermediate particle "X17" with mass around 17 MeV.

Investigation of the ${}^8\text{Be}$ anomaly has been revisited by the same group using an enhanced and separate configuration. They have explored the e^+e^- pair correlations during a high-energy $\mathbf{J}^\pi = 0^- \rightarrow 0^+$ transition of ${}^4\text{He}$ to further support this result. The experiment was repeated with an improved setup in 2019 [7,25]. A sharp 'bump' was observed in the invariant mass distribution of e^+e^- of ${}^3\text{H}(p, e^+e^-){}^4\text{He}$ at about 115° , a feature similar to the anomaly observed in ${}^8\text{Be}$. Even though it appeared at a quiet different opening angle, it is still consistent with the same invariant mass around 17 MeV. They expect to conduct a repeat of the experiment with a focus on enhancing statistics and aim to enhance the energy resolution and implement a more precise cut on the symmetry energy, which will ultimately lead to an improved signal/background ratio.

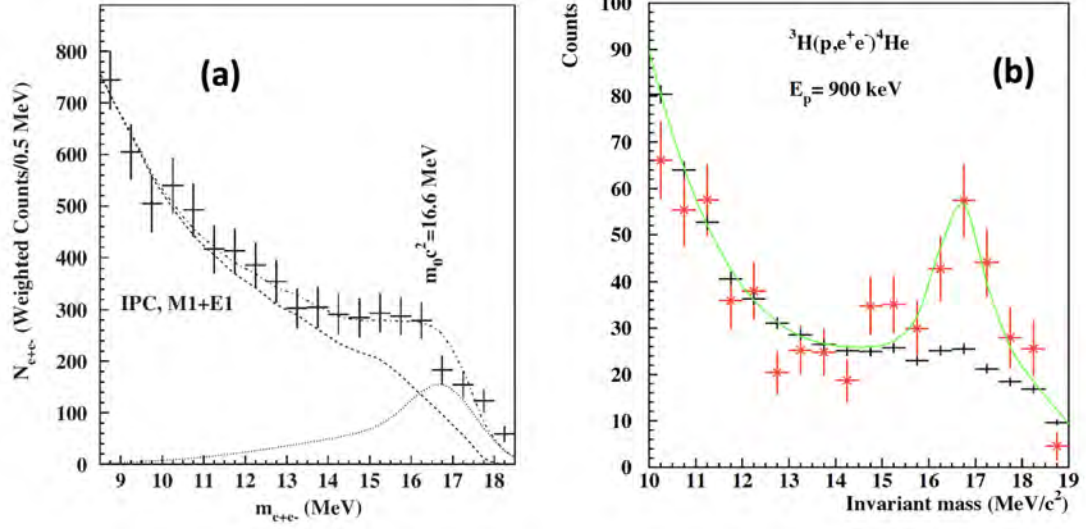


Figure 3.4. (a): Anomaly in ${}^8\text{Be}$ [6]. (b): Anomaly in ${}^4\text{He}$ [7].

This motivated our design of the DarkLight experiment to use the future 50 MeV electron beam from the e-linac driver at the Advanced Rare Isotope Laboratory (ARIEL) to investigate the nature of dark matter [8].

3.3 Projected Scope of DarkLight@ARIEL

To determine the experiment's reach, the background is integrated over the expected signal width ($\pm 1.7\sigma$), and the fifth force coupling (ϵ^2) is calculated such that the signal exceeds a 2σ fluctuation of the background. The shape of the background is predominantly governed by the overall acceptance, resulting in the irreducible background and random coincidences being proportional. Therefore, to evaluate the total background, it is feasible to scale up the irreducible background based on the projected rates.

The anticipated sensitivity and projected reach of the experiment is shown in Figure 3.5. The y-axis represents the relative strength of leptonic coupling in comparison to the fine structure constant α_{QED} , while the x-axis denotes the mediator's mass. It illustrates the attainable range for the four configurations, presuming a con-

sistent beam-time of 1000 hours for each. In Phase 1, a 31 MeV particle beam will be operated for a duration of 1000 hours, in addition to 300 hours designated for commissioning activities. Subsequently, Phase 2, which involves beam energies ranging from 45-55 MeV, is imperative to investigate the permissible 17-MeV region. The light gray areas have been excluded by other experiments sensitive to lepton coupling, while the dark gray area has only been excluded by the electron $g-2$ experiment.

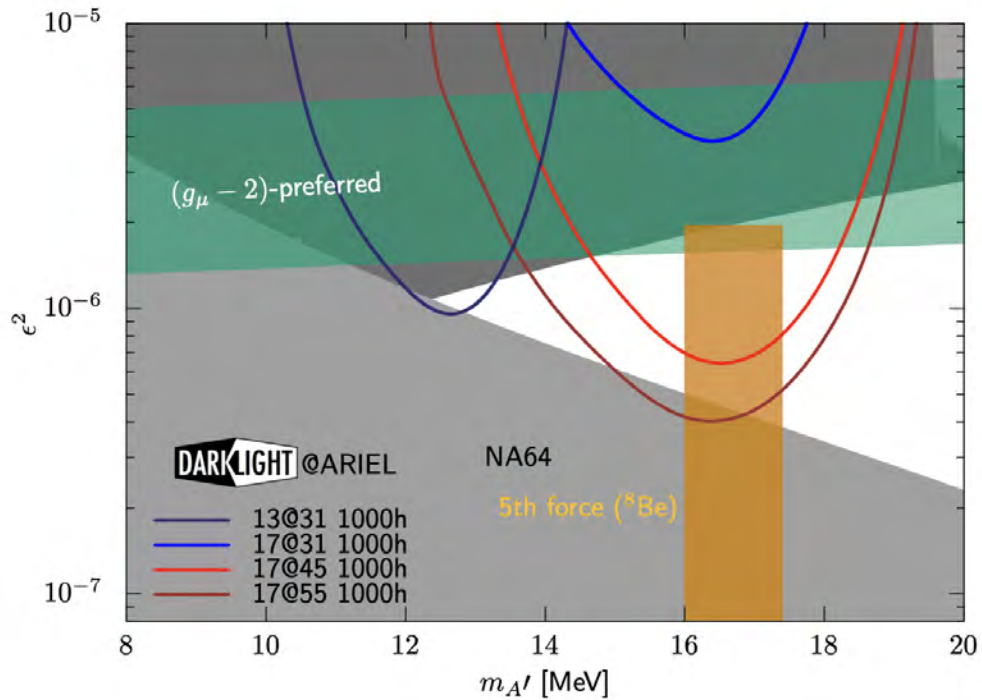


Figure 3.5. The projected reaches on a linear plot for three separate data taking runs: 13@31 (dark blue) - a 1000h run at 31 MeV optimized for $m_{A'} = 13$ MeV; 17@31 (light blue) a 1000h run at 31 MeV optimized for $m_{A'} = 17$ MeV; 17@45 (light red) a 1000h run at 45 MeV optimized for $m_{A'} = 17$ MeV; 17@55 (dark red) a 1000h run at 55 MeV optimized for $m_{A'} = 17$ MeV [8].

With 1000h beam time, the experiment is sensitive to the upper portion of the proposed fifth-force parameter space. DarkLight@ARIEL can reach the kinematic region of the proposed fifth force carrier. It is worth noting that, as DarkLight

focuses on the 17 MeV region, it might be possible to find the proposed particle or set strict limits on its interaction with normal matter.

3.4 Overview of the DarkLight Experiment

DarkLight@ARIEL experiment will be focused on a dedicated search for a dark force carrier with an invariant mass around $17 \text{ MeV}/c^2$. The objective of the DarkLight experiment involves the measurement of the scattering process of $e^- X \rightarrow e^- T a A'$, where A' decays into $e^- e^+$ pairs resulting in,

$$e^- X \rightarrow e^- T a (e^- e^+) \quad (3.4.1)$$

and by detecting the lepton pair in the final state using two dipole spectrometers and a thin foil Tantalum target to achieve sufficient luminosity. Utilizing the ARIEL e-linac provides an advantage by allowing for a lower beam energy which results in a reduced boost of produced bosons. As a result, small angles of forward-going decay leptons can be explored.

Currently, a generator for A' is under development, aimed at replicating the propagation of tracks through the spectrometer, as well as the detection and reconstruction of track parameters at the vertex based on detector measurements. By utilizing this track information, it becomes feasible to calculate the invariant mass of the coincidence tracks, thus enabling us to determine realistic mass resolution. This, in turn, will facilitate enhanced sensitivity by reducing the backgrounds.

3.5 Experimental Setup

The DarkLight experimental setup is shown in Figure 3.7, each spectrometer will feature uniform tracking detector systems, which are comprised of triple Gas Elec-

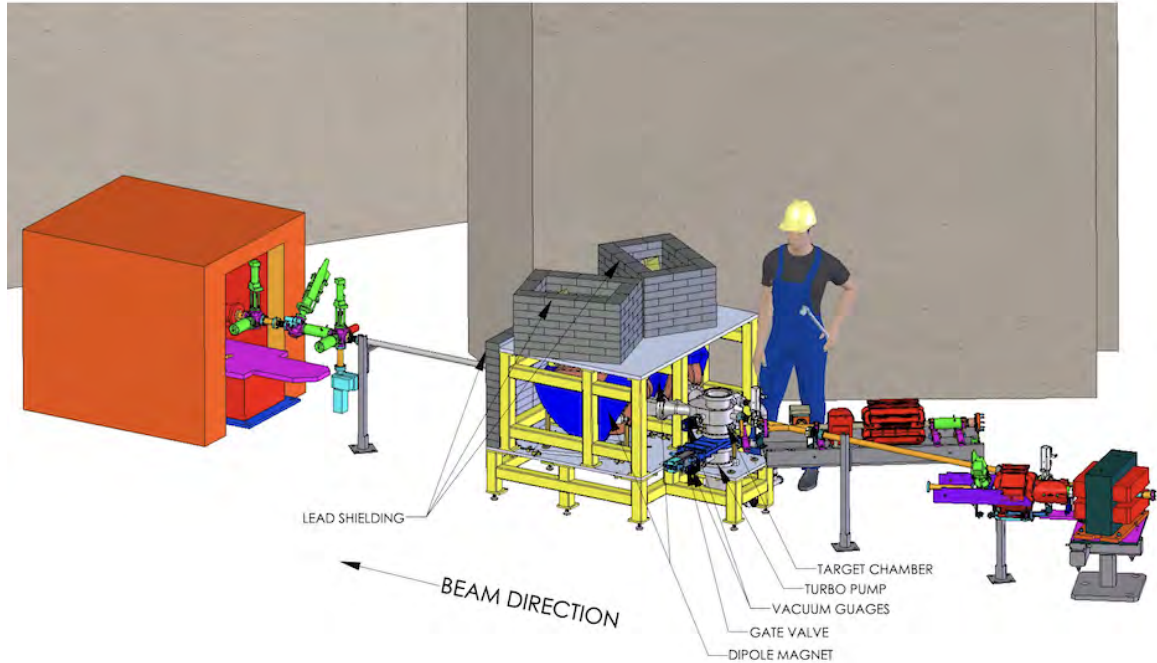


Figure 3.6. 3D CAD rendering of the experimental setup relative to average person for scale [8].

tron Multiplier (GEM) elements. These elements have already been developed and constructed by our group at Hampton University. The trigger hodoscope paddle segments are currently being manufactured at TRIUMF and have the ability to be timed independently. The trigger detector will be responsible for providing timing information. the TOF can be adjusted by altering the path length of the particle through the detector system, which can improve the precision of the momentum and energy measurements.

3.5.1 The Electron Accelerator

Currently, the beam energy at the ARIEL e-linac is 31 MeV, which is relatively low. However, it will be upgraded the beam energy to 50 MeV. As the electron

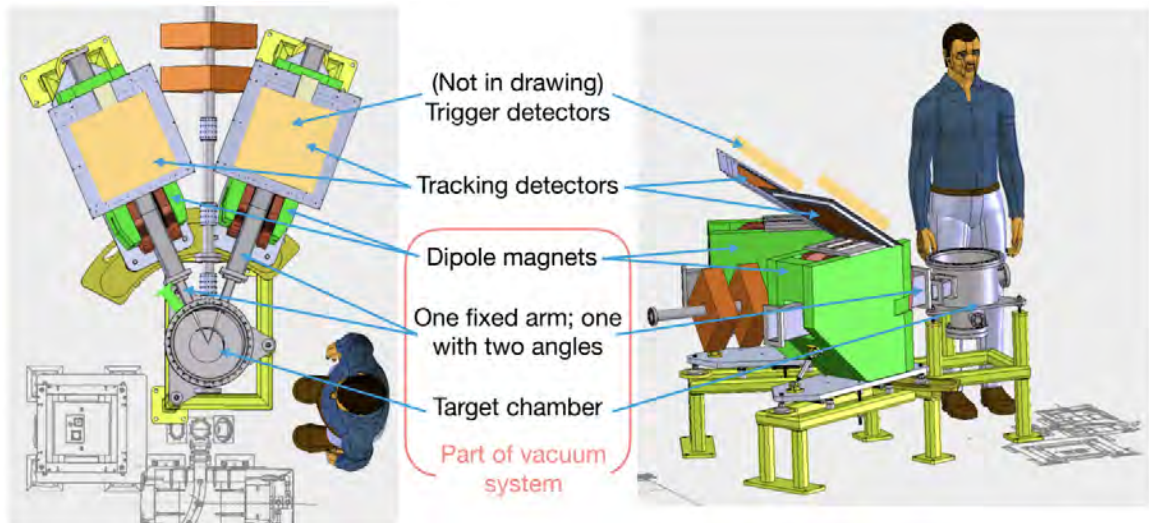


Figure 3.7. CAD representation of the proposed experimental layout with top and side views, featuring the scattering chamber, a pair of magnetic spectrometers, and GEM detectors.

accelerator evolves, the proposed DarkLight experiment can progress through three different stages.

- Stage 0 - The experiment would be located in front of the 10kW dump (Figure 3.8). The linac will be operated in a continuous wave mode, utilizing an electron beam energy of 31 MeV at a current capacity of up to $300 \mu\text{A}$.

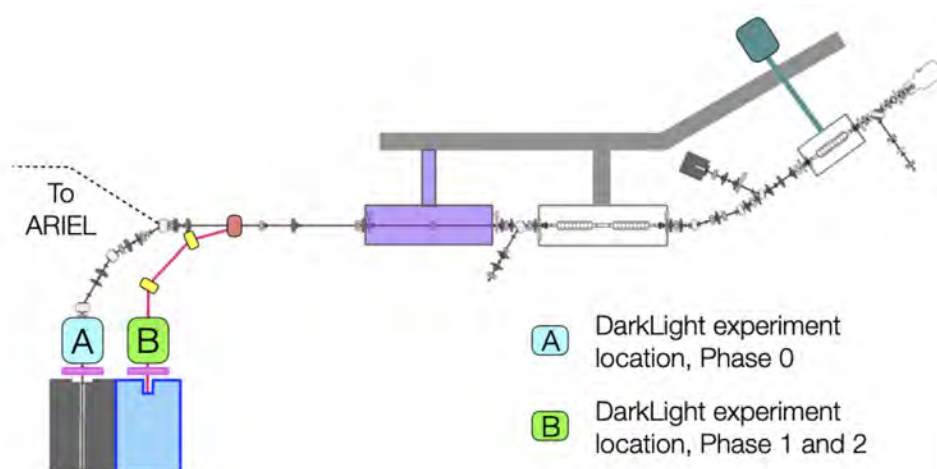


Figure 3.8. Floor plan of the ARIEL e-Linac. Phase one (31 MeV) will be conducted in position A, while phase two (50 MeV) will take place in position B.

- Stage 1 - A second cryo-module would be installed to increase the beam energy to 50 MeV, along with a dedicated dump and beamline (Figure 3.9). The experiment would relocate in front of the new dump, and a dipole magnet would deflect the beam through the target into the dump. The electron beam will undergo energy recirculation, wherein it will pass through the accelerating module for a second time and eventually reach an energy level of 50 MeV.
- Stage 2 - A septum magnet and RF deflector would be included to enable 50 MeV beam delivery to both ARIEL and DarkLight simultaneously (Figure 3.9).

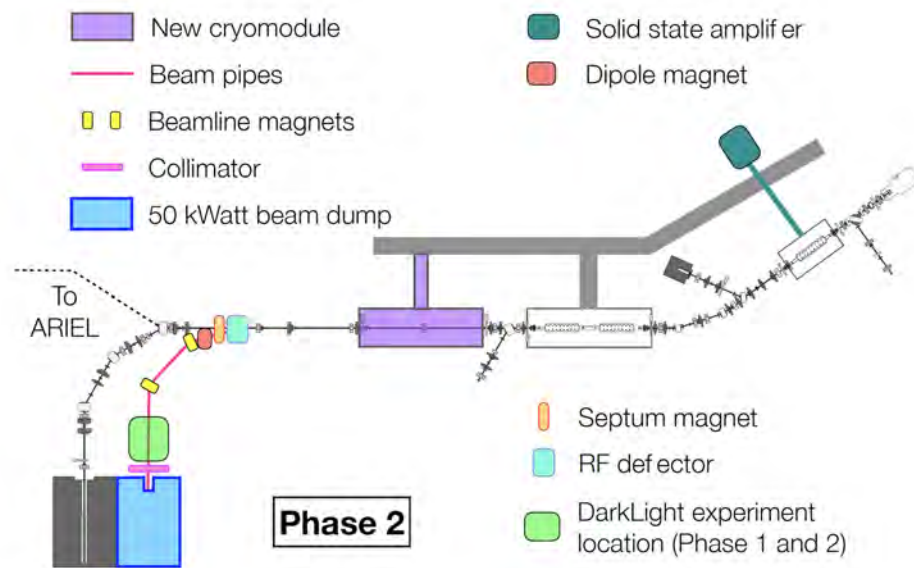


Figure 3.9. Floor plan of the ARIEL e-Linac for the final phase of the DarkLight experiment, with a cryo-module to increase the energy from 31 MeV to 50 MeV, and a septum magnet and RF deflector for concurrent beam delivery to ARIEL and DarkLight.

3.5.2 Target

As mentioned above, the experimental setup involves several beam energies ranging from 30 MeV to 50 MeV, with a current of $150 \mu\text{A}$ directed onto a $1 \mu\text{m}$ tantalum foil. The interaction between the beam and the foil generates an instantaneous luminosity of $L = 5.2 \text{ nb}^{-1} \text{ s}^{-1}$. Furthermore, the beam spread downstream of the target is approximately 0.5° .

As the 31 MeV electron beam passes through the tantalum target, it undergoes energy loss and experiences multiple scattering due to the target's 1 μm thickness. This energy loss leads to heating of the target, while multiple scattering increases the beam's emittance and causes the beam size to increase downstream towards the beam dump.

3.5.3 Spectrometers

The experimental setup involves the use of two dipole spectrometers, which are being built by MIT/Bates, to measure the final state e^+e^- pairs. The magnetic characteristics and pole shapes of the spectrometers have already been designed. The mechanical design of the supports and coils is currently being finalized. Although the two spectrometers have a common design, they will be operated at different currents in order to generate the required magnetic fields. These are standard iron-core magnets with basic, flat coils. The magnet and pole face design were specifically tailored for a spectrometer entrance situated 0.5m from the target and for trajectories that are appropriate for tracking with GEMs. The spectrometers will be designed with similar specifications, which are presented in Table 3.1.

Table 3.1

Specifications of the Dipole Spectrometers

Parameter	Value
In-plane acceptance	$\pm 2^\circ$
Out-of-plane acceptance	$\pm 5^\circ$
Momentum acceptance	$\pm 20\%$
Minimum central angle	16°
Maximum central momentum	28 MeV
Dipole field	0.32 T
Nominal bend radius	30 cm
Pole gap	4 cm

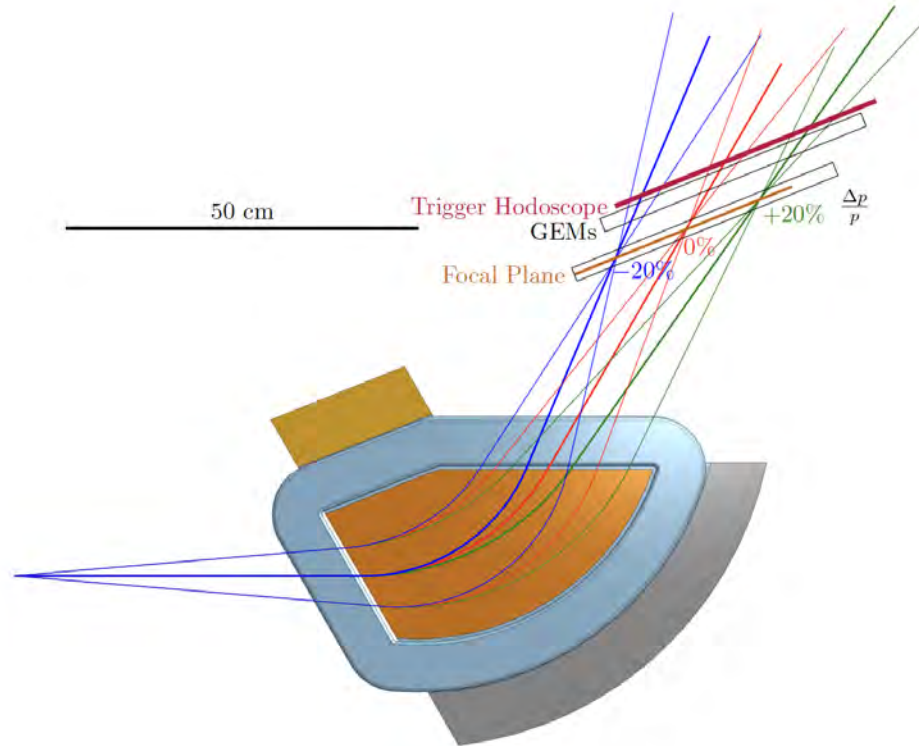


Figure 3.10. The figure displays a schematic overview of the spectrometer optics with GEM detectors and trigger hodoscopes. The central momentum, p_0 , is depicted in red, while the colors blue and green correspond to $p_0 - 20\%$ and $p_0 + 20\%$, respectively.

3.5.4 GEM Detectors

Each spectrometer will be equipped with a tracking detector system that is identical and consists of triple-GEM elements with an active area of $25 \times 40 \text{ cm}^2$. These detector modules have two-dimensional APV front-end readout cards with a pitch of $400 \mu\text{m}$ between strips. The APVs are read out into Multi-Purpose Digitizer front-end cards of the latest generation (APV4.1 and MPD4.0). These detector modules were constructed using a novel technique, which is explained thoroughly in the following chapter.

The fabrication of eight detectors utilizing this approach resulted in three being relocated to Research Center for Electron Photon Science (ELPH), at Tohoku University in Sendai, Japan for ULQ2 experiment, while the remaining detectors were

undergoing testing at the Low Energy Recirculator Facility (LERF) at Jefferson Lab. Two of the three ULQ2 elements were later sent to CERN for repairs and sent back to LERF in 2022. Out of these, four GEM chambers will be made available for Dark-Light at ARIEL. The detectors will be assessed using a Sr-90 source and validated through the use of cosmic rays prior to being transferred to the ARIEL accelerator site. Furthermore, the testing and commissioning of the detectors with ULQ2 beam was examined utilizing three GEM detectors were discussed in Chapter 4

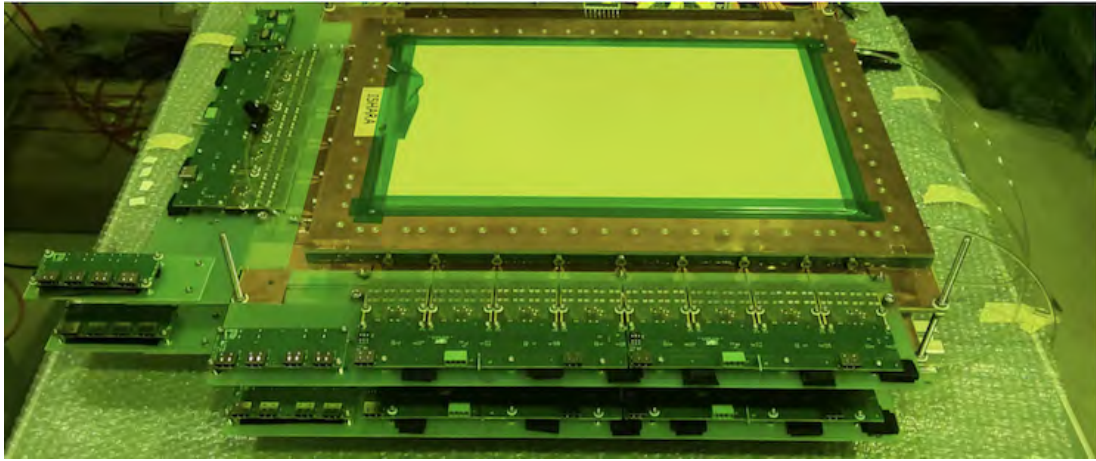


Figure 3.11. The picture shows two fully-equipped GEM elements, including APV frontend electronics, back-planes, adapter boards, and low-voltage regulator board.

3.5.5 Trigger Hodoscopes

The standard readout for GEM detectors necessitate a trigger signal, which is produced by the coincidence of two prompt trigger detectors in the spectrometers. The trigger detector will be fashioned using scintillator paddles, partitioned into 8 segments along the dispersive direction, with each segment being read out by 6 SiPMs (Hamamatsu S13360-3075PE measuring 3mm x 3mm). This enables independent timing of each segment. The scintillator paddles will be constructed using BC-404,

which is a typical plastic scintillator material, and will measure $150 \times 30 \times 2 \text{ mm}^3$ in size.

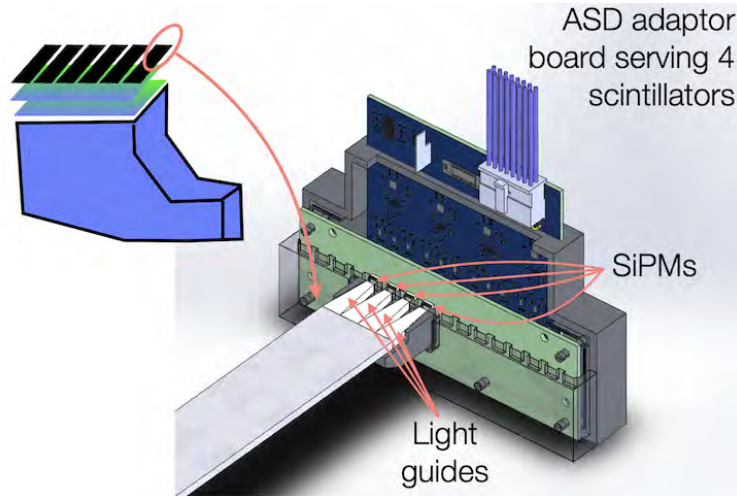


Figure 3.12. Scintillator paddles attached to SiPMs - Image courtesy: Kate Pachal.

3.5.6 DAQ, Trigger Electronics and Slow Control

The signals generated by the trigger hodoscope counters will undergo pre-amplification and summation from both ends. Following this, the output will be subject to discrimination and timing, utilizing both leading-edge and trailing-edge techniques. This process will be carried out by a TDC based on FPGA technology. Through the utilization of the FPGA firmware, it will be possible to generate triggers from e^+e^- coincidences within very narrow coincidence windows. The use of small coincidence time windows is necessary to identify coincidences at the level of individual bunches. This methodology aids in minimizing the recorded background.

To read out the GEMs, APV-25 and MPD4 readout boards from our group at Hampton University will be employed. Refer to Section 4.5 for further details on readout electronics and software framework. A VME crate will be allocated per spectrometer to house the MPD4, in addition to the FPGA trigger module. The

development of the necessary FPGA trigger firmware, basic DAQ software, and required slow controls will be undertaken by the TRIUMF DAQ group in conjunction with SBU.

CHAPTER 4

CONSTRUCTION AND COMMISSIONING OF GEM DETECTORS

4.1 Introduction

Over the past 25 years, the manufacturing process of GEMs have developed rapidly to allow for the production of many prototype detectors for small and large scale research and development programs. In particular, research done on GEM foil fabrication has allowed flexible geometry options to use for various experiments. Arbitrary shapes for GEM foils such as square, rectangular, annular and cylindrical are being used. For readout, hexagonal pads, X-Y pattern strips and pads, 2D stereo-angle (U-V) strip readout and in some cases a mix of both (X-Y and U-V) are being used. Considering that GEM foils are used in a variety of shapes and sizes, different techniques are used to construct the detectors.

In this chapter, the "NS2" technique, design, parts and assembly used for construction of a set of 40 cm \times 40 cm GEM detectors will be discussed in depth. Furthermore, testing and commissioning of these detectors will be performed and results will be evaluated.

4.2 Foil Stretching Techniques

The GEM foils are usually used in multi-layer structures and each foil is supplied with a voltage. Therefore, it is extremely important to maintain a gap between the foils to avoid electrostatic discharges and deformations. Due to this, "stretching" of the GEM foils is the most crucial process of assembly in to a detector.

To construct large-area GEM detectors, foil-stretching is usually achieved by two methods - mechanical and thermal.

4.2.1 Mechanical Stretching Technique

Traditionally, a rigid mechanical system is used to clamp the prepared GEM foils and stretch to a desired tension uniformly in four directions. Then the foils are glued to frames with spacers for large-area GEM detectors. The method shown in Figure 4.1 is used for the Back-Tracker GEM modules made for SBS (Super Big-Bite) apparatus at Jefferson lab. It uses a custom-made mechanical stretching system which can provide a uniform tension of 0.5 kg/cm on each side. The foil is positioned and aligned with the dowel pins and clamped in to the system on four sides, then the tension is applied while monitoring on a digital scale. When the foils are stretched, a spacer frame is glued on to the GEM foil. The frames have a grid of 300 μm wide spacers to maintain a uniform gap [26].



Figure 4.1. Mechanical stretching of 50 x 60 cm² GEM foils made for a SBS by UVA - Left: Stretched GEM foil using a mechanical system on four sides. Right: Top figure shows the close-up of the mechanical system and bottom figure shows the GEM foil after gluing on to the spacer frame.

4.2.2 Thermal Stretching Technique

Thermal stretching of GEM foils is traditionally accomplished by placing the foil in a large Plexiglas frame. This setup is placed inside a low temperature clean room oven. The coefficient of thermal expansions are $7.2 \times 10^{-5} \text{ }^\circ\text{C}^{-1}$ and $1.7 \times 10^{-5} \text{ }^\circ\text{C}^{-1}$ respectively for Plexiglas frame and Kapton foil. Because of the higher coefficient of thermal expansion of the Plexiglas frame, when a temperature is applied and increased the Plexiglas frame expands more than the kapton foil, resulting tension on the kapton foil [9]. Once the desired stretching has been achieved glue is applied to the FR4 frame and attached to the stretched GEM foil. Excess kapton foil is removed after the glue has cured.

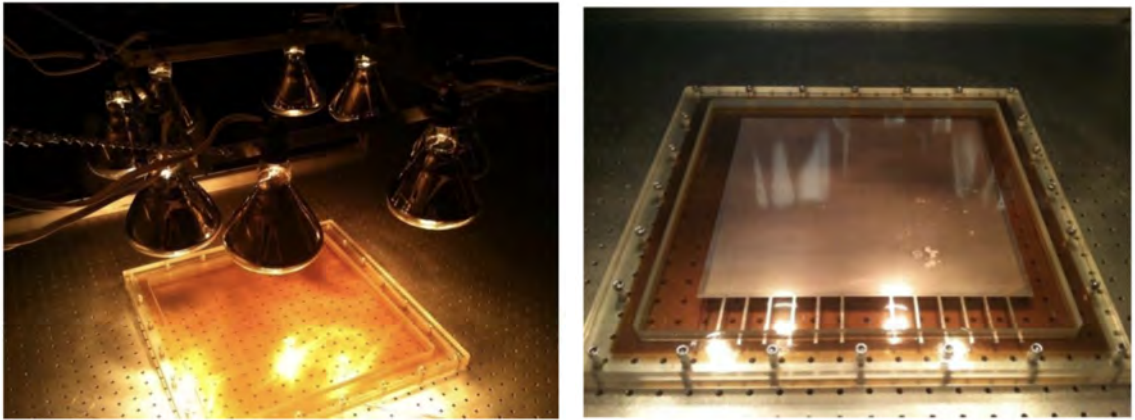


Figure 4.2. Thermal stretching of 30 cm \times 30 cm GEM foils made for a muon tomography station by Florida Tech - Left: IR array setup for thermal stretching on an optical bench. Right: GEM foil tensioned at $\sim 40^\circ\text{C}$ [9].

A group in Florida Institute of Technology tested thermal stretching technique using an IR array instead of a clean room oven as shown in Figure 4.2. This method can be used to stretch foils used for large-area GEM detectors at low cost by using IR array system instead of using a clean room oven.

4.2.3 Drawbacks

In these construction methods, the assembly is a very time-consuming process and it cannot be compromised by any errors during the procedure. Both of these methods involve gluing of the stretched foil to a rigid frame. Therefore, the GEM detector is integrated into a whole un-detachable chamber leaving no possibility of repairing the chamber by replacing any parts if needed. Usage of thin insulated spacers introduces more dead area to the active area of the detector.

To address these major drawbacks, a new technique was introduced to stretch the GEM foils which is called "Self-Stretching" or "NS2" (No Stretch - No Stress) Technique.

4.2.4 Self-Stretching Technique

The self-stretching technique was first introduced at CERN in 2011 using its first 10 x 10 cm² triple-GEM detector called "CMS Proto III". This method uses a double mechanical frame where, the drift layer and GEM foils are tightly sandwiched between the inner frames and then are being pulled by a mechanical system of the outer frame in the stretching process. After the GEM foils have been stretched out completely the readout board is mounted and the detector is covered with top frame allowing gas tightness inside the detector. The design will be discussed in the following section.

When compared with the standard assembly procedures that was discussed in 4.2, it is evident that the detector assembly is very fast, for example the 25 x 40 cm² detector was assembled in 2-3 hours. The detector does not require spacers in the active area to avoid electrostatic force between electrodes. Nor gluing neither soldering was used in the assemble process and that allows for the detector to be re-opened for any repairs, replacements or modifications. With prototype detectors at CERN, it was also observed that the detector response was very uniform across the surface of the GEM foils [27].

4.3 Design

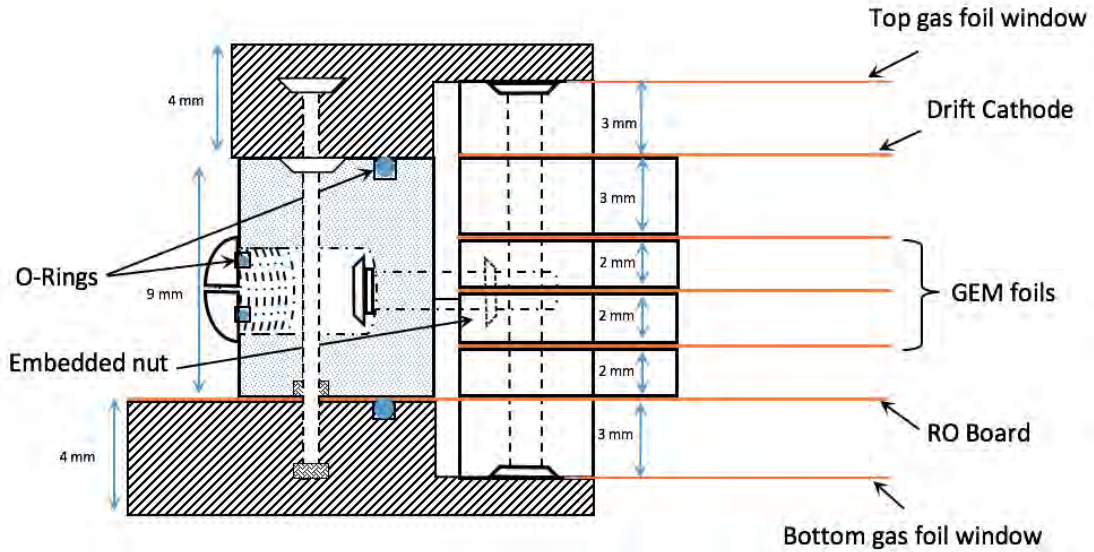


Figure 4.3. Schematic of self-stretch technique used to build the GEM detector for DarkLight@ARIEL experiment.

As shown in the figure 4.3, the GEM foils are mechanically fixed to the inner frames by vertical screws. These inner frames are located outside the active area and are embedded with nuts. The main frame is then attached by a series of horizontal screws which are fastened to nuts embedded in the inner frames. O-rings are placed carefully to provide gas tightness to the detector. Mechanical tension is provided by the main frame; the horizontal screws are used to pull the inner stack of frames to stretch the foils. The readout board is extended along 3 sides, 2 sides for receiving signals and one side for high voltage power supply. Finally the whole stack is covered with top and bottom covers with gas window foils made with $0.1\mu\text{m}$ Chromium on Kapton.

4.3.1 GEM Foil

The GEM detector has a "3-2-2-2 structure", where the gap between drift cathode-GEM foil(1)-GEM foil(2)-GEM foil(3)-readout anode are in units of mm. The GEM foil has a 25 cm \times 40 cm active area segmented into 10 high voltage sectors on top copper layer. Each segment is connected to a 1 M Ω protective resistor designed to prevent possible damage to GEM foils as a result of discharge.

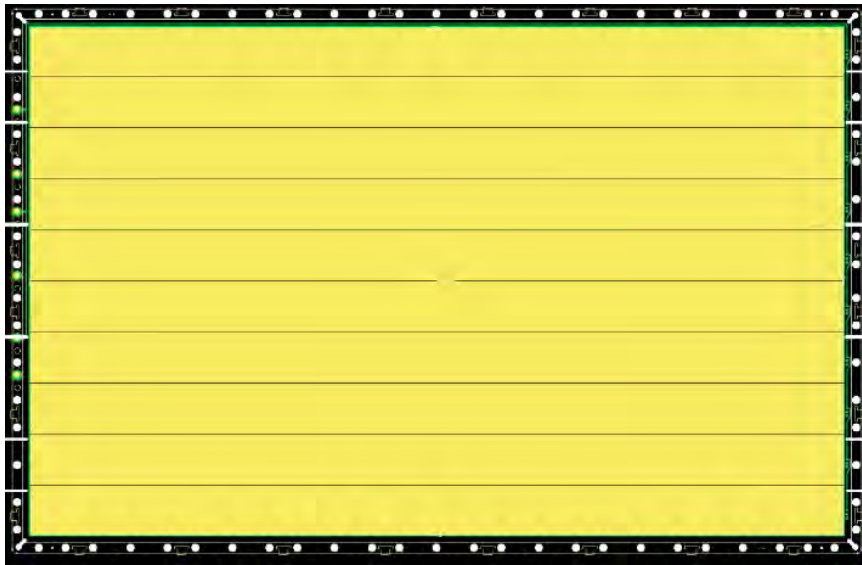


Figure 4.4. Top view of segmented GEM foil with 25 cm \times 40 cm active area - credit: Bertrand Mehl, CERN.

This design protects the GEM foils from possible damage if discharging occurs, and ensures that any shorted segments are isolated from the rest, thereby maximizing the efficiency of the detector during operation.

4.3.2 Gas Flow

The main frame has two gas inlets and outlets on short side for forced gas supply to the detectors. Each inner frame has 6 inlets and 6 outlets on short sides to provide gas flow uniformly between GEM foils.

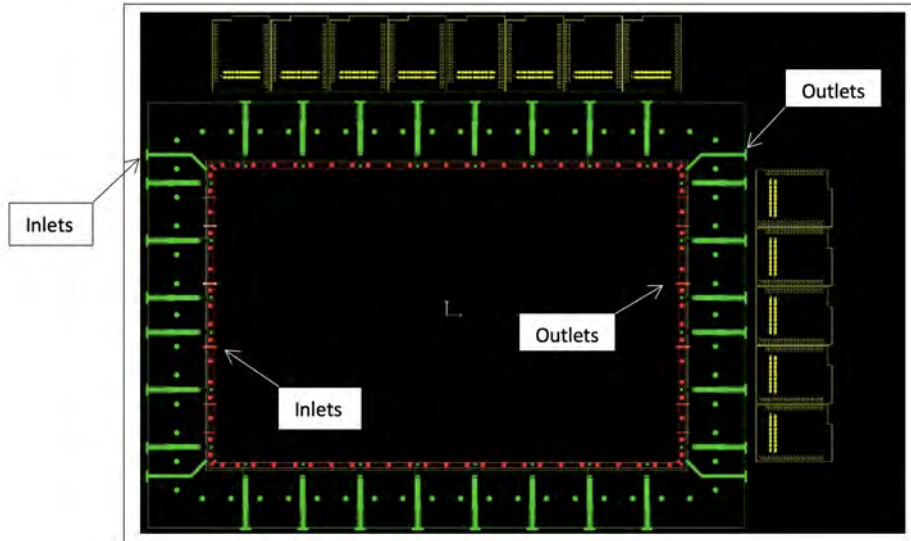


Figure 4.5. Two main inlets and outlets are shown (green) on corners of the main frame and 6 inlets and 6 outlets are shown (red) on shorter sides of inner frames - credit: Bertrand Mehl, CERN.

4.3.3 High Voltage Supply

The high voltage system consists of a series of 26 spring loaded pins in 4 sizes. These are called battery probes and are used to enable quick and easy detachment. Battery Probes are compact and built with spring-loaded contacts. Table 4.1 and 4.6 shows the usage of the pins to provide HV connections through D (Drift foil), G1 (GEM foil-1), G2 (GEM foil-2), G3 (GEM foil-3) and R (Readout board).

14 long pins (FK 603-15) are used between the readout layer and the drift foil layer in order to guide the voltages to all layers. For redundancy duplicate set of pins will supply the voltage to the same foil. The long pin that transmits the voltage from the readout to the drift layer is directly adjacent to the shorter pin that points to the final destination foil. As the GEM foils are stacked, the voltage of each foil can be measured by the long pin on the readout board. Each foil can be electrically tested throughout the stacking process.

Table 4.1

Table of Technical Data of High Voltage Spring Loaded Pins.

HV pin	Overall length (mm)	Electrical resistance($m\Omega$)	Current load(A)	Connection
FK 480	6.10	80	2.0	D-G1
FK 381	8.00	50	3.0	D-G2
FK 441	10.52	100	3.0	D-G3
FK 603-15	15.00	50	4.0	R-D

Pin Ordering

During the stacking up process, the drift foil is prepared by fixing these 26 HV pins onto the inner frame A, as shown in 4.7. Orienting the drift foil upside down, the pins are arranged from left to right as follows:

- 1) R-D
- 2) R-D
- 3)-6) D-G1T, R-D, R-D, D-G1T
- 7)-10) D-G1B, R-D, R-D, D-G1B
- 11)-14) D-G2T, R-D, R-D, D-G2T
- 15)-18) D-G2B, R-D, R-D, D-G2B
- 19)-22) D-G3T, R-D, R-D, D-G3T
- 23)-26) D-G3B, R-D, R-D, D-G3B

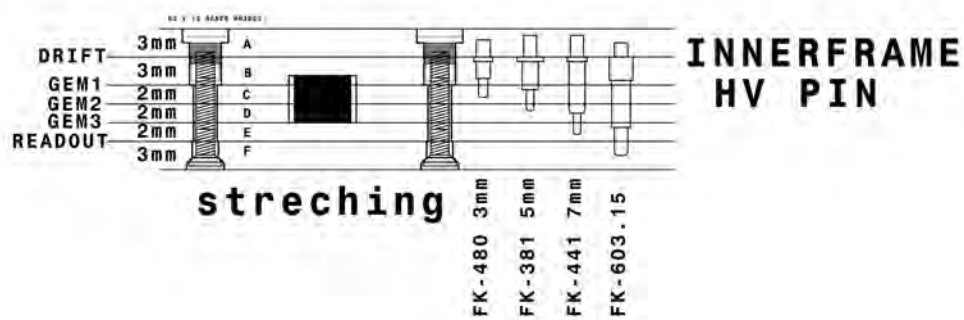


Figure 4.6. High voltage divider system - credit: Bertrand Mehl, CERN.

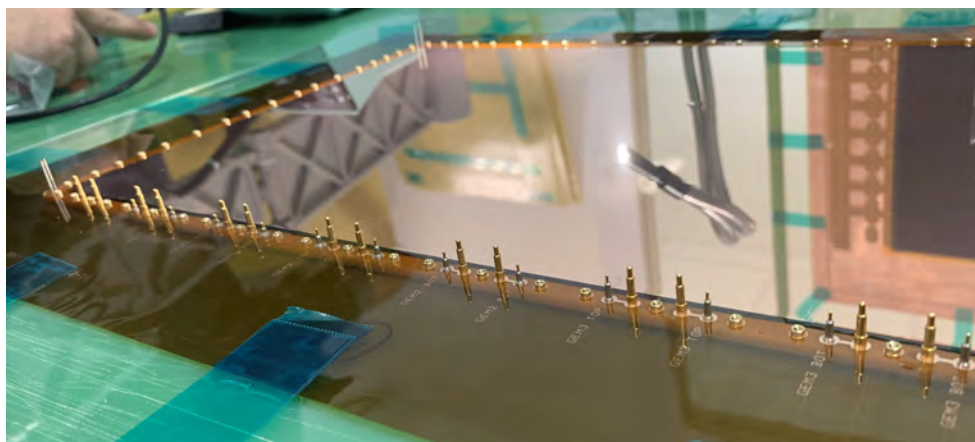


Figure 4.7. Ordering of the pins from (1) to (26) from left to right on drift foil attached on inner frame A.

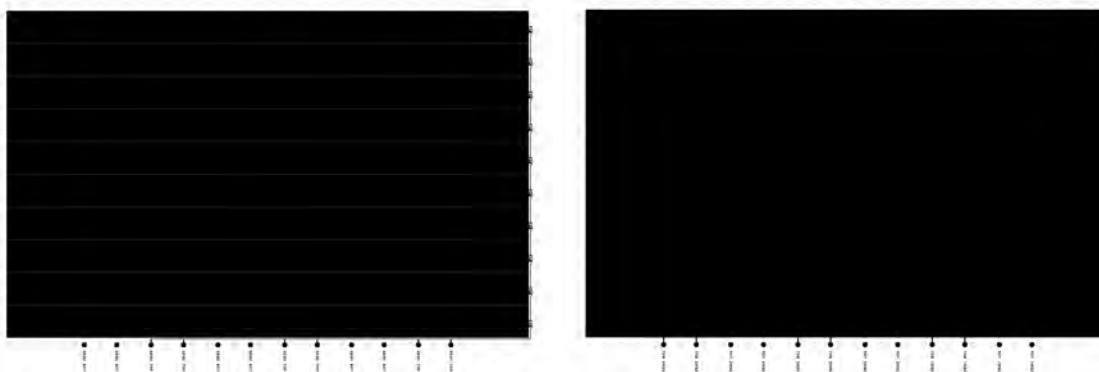


Figure 4.8. GEM foil top layer (left) and bottom layer (right) - credit: Bertrand Mehl, CERN.

As shown in figure 4.8, the GEM foil is equipped with connections to the HV system on the top and bottom layers.

4.4 Construction

Utilizing the self stretch technique, we built eight GEM detectors. First GEM detector was built at CERN in February, 2019 at Micro Pattern Technologies lab with the guidance of lab leader Rui De Oliveira. Detailed instructions were provided to assist in the preparation and assembly of the detector parts. Seven other detectors were constructed under clean room conditions at Jefferson Lab's Low Energy Recirculator Facility (LERF).



Figure 4.9. From left to right - Tanvi Patel, Jesmin Nazeer, Rui De Oliveira, Michael Kohl at CERN after assembly of the first detector.

4.4.1 3D CAD Modeling

All the components of the detector was visualized using a cloud based 3D CAD modeling software called Onshape. As each part was reproduced using 3D CAD and

assembled in the cloud-based workspace, we were able to see a visual representation of the detector as well as obtain precise measurements for simulations of the experiment.

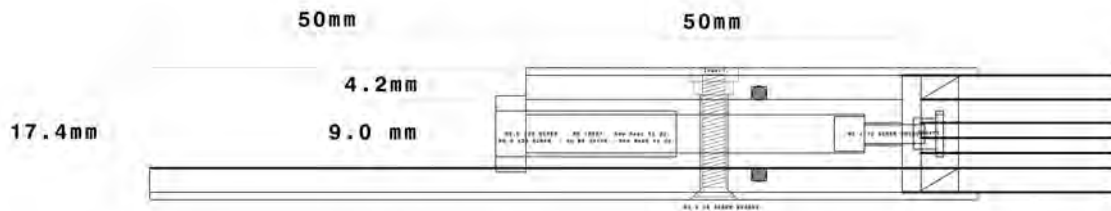


Figure 4.10. Schematic of triple layer GEM assembly for DarkLight@ARIEL - Credit: Bertrand Mehl, CERN.

As shown in Figure 4.10, the main parts of the detector are,

- Top cover with gas foil window - 4.2 mm
- Inner frame A - thickness 3 mm
- Drift foil
- Inner frame B - thickness 3 mm
- GEM foil
- Inner frame C - thickness 2 mm
- GEM foil
- Inner frame D - thickness 2 mm
- GEM foil
- Inner frame E - thickness 2 mm
- Readout board
- Inner frame F - thickness 3 mm
- Main frame/ Outer frame - 9 mm thickness
- Bottom cover with gas foil window - 4.2 mm

To provide a better understanding of the detector assembly process, the main steps are briefly discussed below with 3D illustrations from Onshape.

Assembly of Inner Stack

1. Stack up the drift foil, three GEM foils and readout board in the correct sequence on the inner frames. Clamp all the foils using vertical screws.

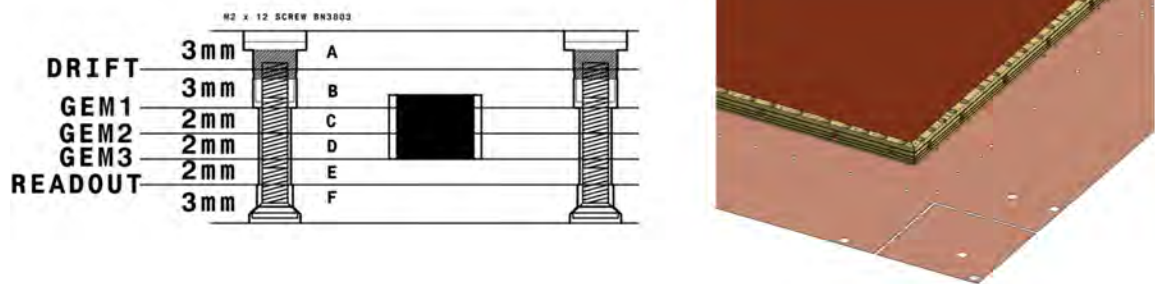


Figure 4.11. Drift foil, 3 GEM foils and readout board sandwiched between the inner frames from A to F.

Foil Stretching

2. Cut off excess foils around the inner frames. Then place the main frame around the stack of inner frames and secure it with horizontal screws through the embedded nuts inside the inner frames. Stretch the GEM foils.

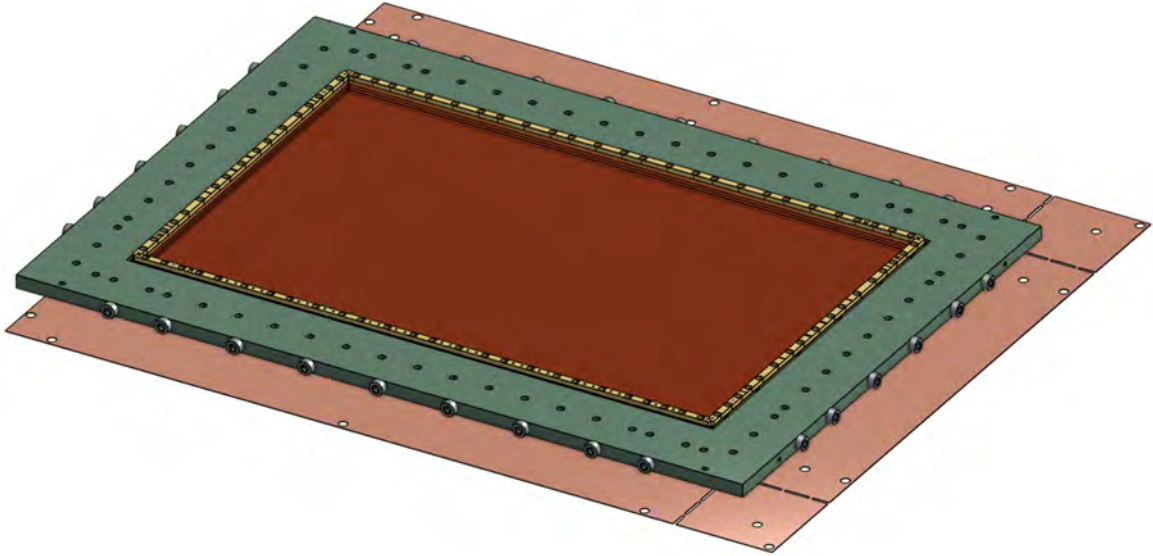


Figure 4.12. Outer frame providing mechanical tension with screws through embedded nuts inside the inner frames for GEM foil stretching.

Closing of the Chamber

3. After stretching of the foils, close the chamber with top and bottom gas window covers. As a final step, the horizontal openings in the main frame are sealed using M6 screws.

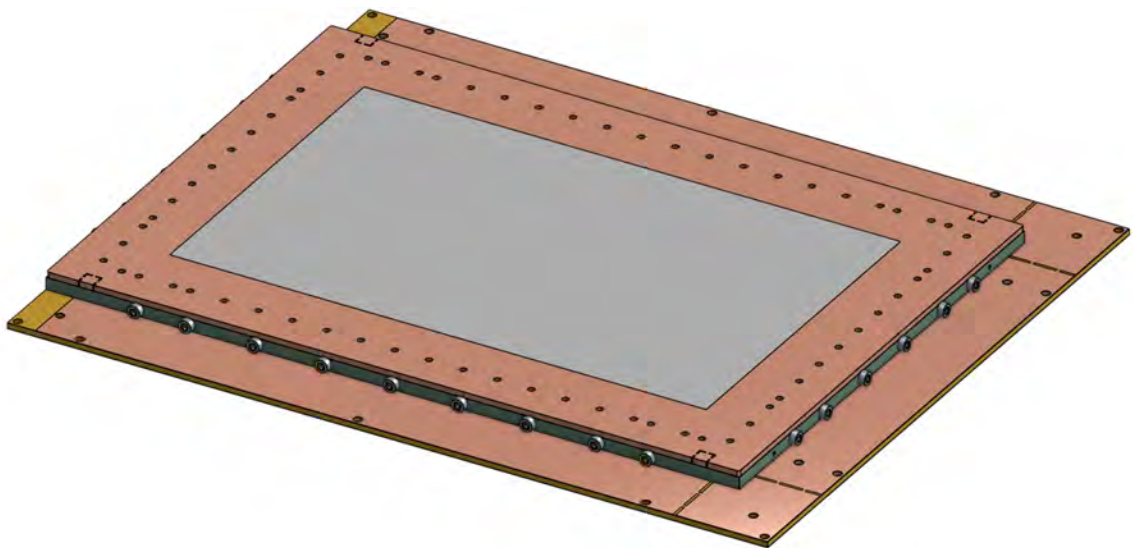


Figure 4.13. Final GEM chamber closed with top and bottom gas window covers.

4.4.2 Preparation

Clean-room

It is necessary to handle GEM foils under certain environmental conditions in order to prevent unwanted dust particles from adhering to their surface and to enhance their performance. All the preparation of foils and assembly was done inside a clean room in LERF at Jefferson lab. In order for the GEM foils to perform more effectively, the clean room humidity was monitored to be $< 35\%$. In order to prepare the clean room, the floor was vacuumed, mopped down, and then vacuumed again. The entrance to the clean room was equipped with sticky sheets to attract any dust particles that may be introduced as a result of people entering the room. It was required to wear clean room suits, bouffant hats, shoe covers, face masks and gloves to maintain low concentration of airborne particulates.

Preparation of GEM Foils

GEM foils are required to pre-stretch to avoid any deformations to its hole pattern during handling. Using green tape, the foils are pre stretched on an oversized rigid frame. A tacky roller was used to remove dust from both sides of the GEM foils after they had been pre-stretched. After the GEM foils were cleaned they were tested with 500V across the top and bottom layers to test the resistance of the GEM foils. In the final step, as shown in Figure 4.14 the pre-stretched, cleaned, and tested GEM foils are stored within a large storage closet to be used later on.

Each time a foil is handled, it was tested and confirmed that it retains its voltage when supplied with 500V immediately afterward and shows $> 100G\Omega$ as shown in Figure 4.15. It is recommended to repeat the above steps to ensure that there are no issues.

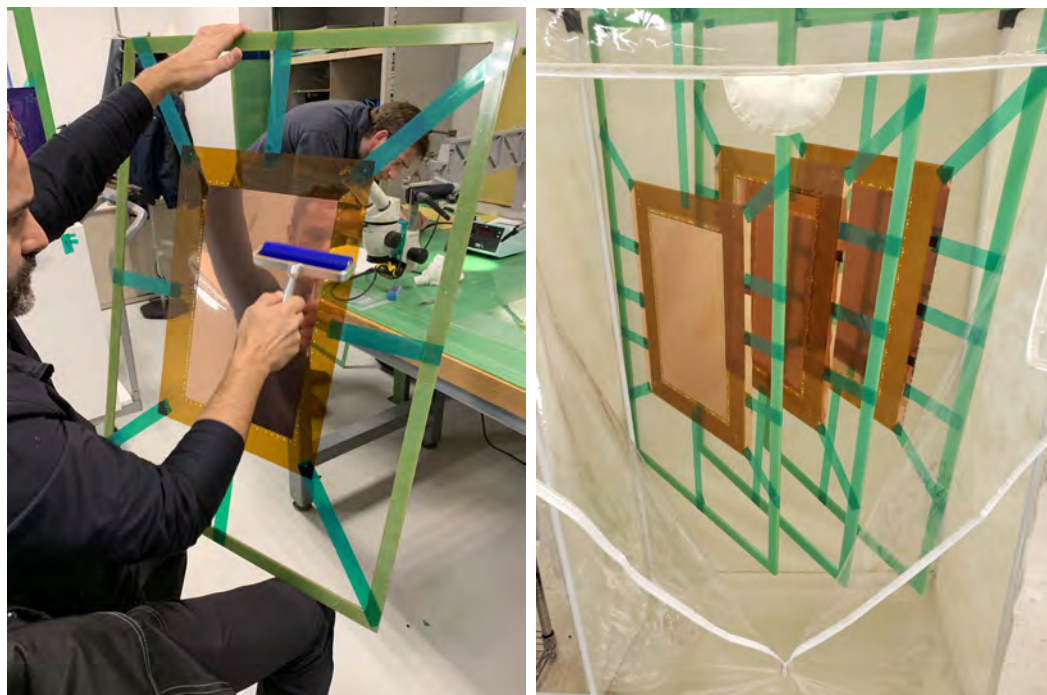


Figure 4.14. Pre-stretched GEM foils being cleaned to remove dust particles from the surface using a tacky roller.



Figure 4.15. The performance of pre-stretched GEM foils at high voltages is being tested using the Megger MIT430/2 insulation tester.

Preparation of Top Gas Window Cover

The top gas window cover was prepared by hammering the inlay nuts into the frame on top side as shown in Figure 4.16. Then o-ring was then installed on the bottom side of the housing as shown in Figure 4.17

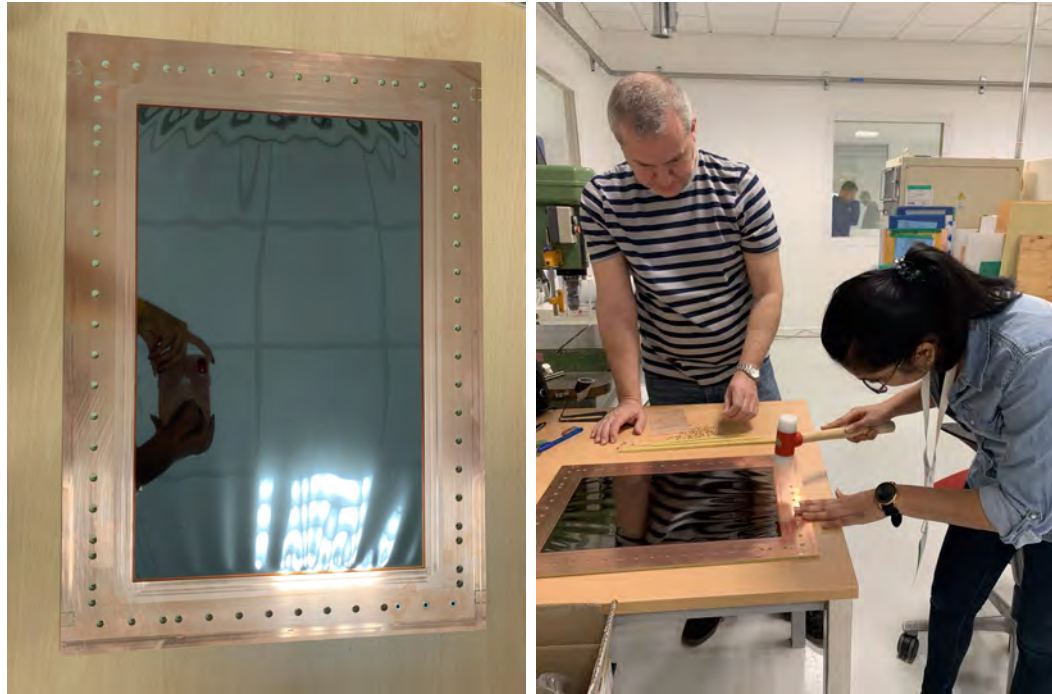


Figure 4.16. Top side of top cover with holes for inlay nuts (Left) and inlay nuts were hammered into the top gas window foil (Right).



Figure 4.17. Top side of top cover with fixed inlay nuts (Left) and bottom side of top cover with embedded o-ring (Right).

Preparation of Inner Frames

The inner frames are marked from A to F, with varying thicknesses as shown in Figure 4.11. The inner frames come in two sizes, one for the long side and one for the short side. The inner frame A features an adhesive side and holes for the inlay nuts that connect to the vertical screws as shown in Figure 4.18. Thus, inner frame A needs to be prepared by hammering in the screws using a rubber hammer in order to prevent damages to the frame edges as shown in Figure 4.19

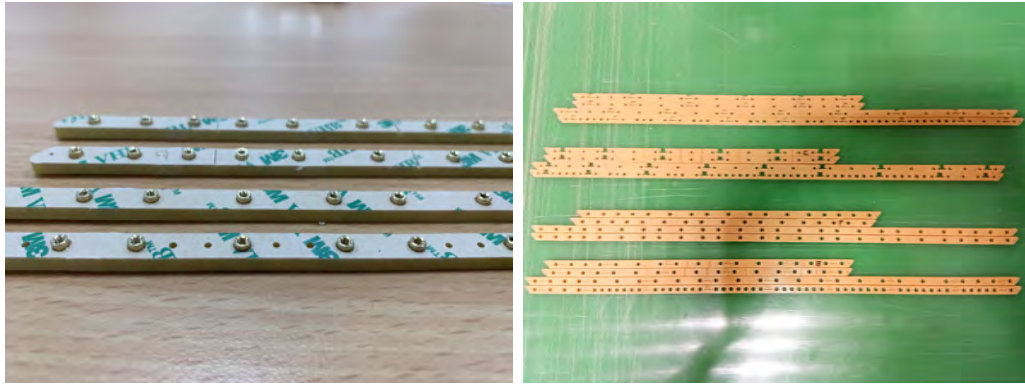


Figure 4.18. Prepared adhesive side of inner frame A with embedded nuts for vertical screws (Left) and Inner frames B-E (Right).



Figure 4.19. Hammering of inlay nuts into the inner frame A (Left) and non-adhesive side of prepared frame A (Right).

Preparation of Drift Foil

The drift foil is prepared by pre-stretching it using the oversized rigid green frame. After cleaning the drift foil using the tacky roller it is fixed onto the inner frame A which sits on a plexi-glass sheet. Then the HV pins are soldered from left to right as shown in figure 4.7. The HV pins will stick through the drift foil into the type-A frame holes. The procedure is explained further in detail in the section 4.4.3.

Preparation of Readout Board

Also, the readout board was pre-stretched using an oversized rigid frame and green adhesive tape in the same manner as GEM foils. The tacky roller was used to remove dust from the corners of the readout board after the corners had been cut off. Afterward, the wires were soldered to the high voltage connections on the readout board. To identify the ground connection, the most negative was marked with green tape.

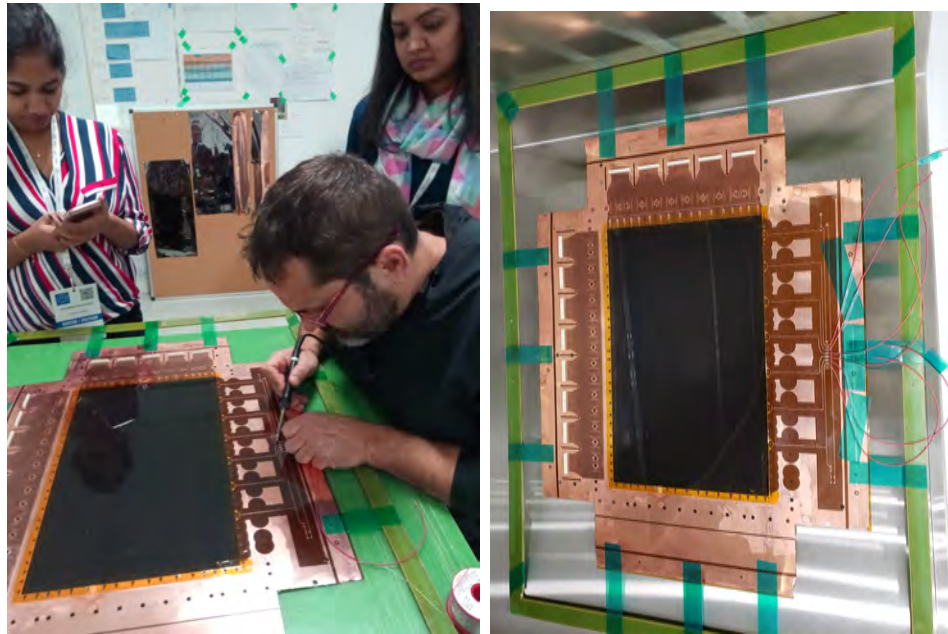


Figure 4.20. Soldering of wires to the HV connections on RO board (Left) Pre-stretched, prepared and cleaned RO board (Right).

4.4.3 Assembly

GEM detector is assembled in three main steps as discussed briefly in section 4.4.1.

4.4.3.1 Assembly of Inner Stack

It is necessary to assemble the inner stack by starting with the drift layer at the bottom, stacking up GEM foils, and finishing with the readout layer at the top. The stack is constructed on a Plexiglas base frame with holes for two dowel pins in each corner to facilitate stack alignment. Also there is an alignment dowel pin hole in each corner of the inner frames and foils which allow them to be precisely positioned on the Plexiglas.

The inner stack was assembled in the following manner.

1. Place the Plexiglas base on a work table and clean the surface with an anti-static cloth. The Plexiglas was fixed to the table using green tape for more secure placement. The sides are marked from 1-4 in order to ensure that the inner frame bars are positioned correctly.



Figure 4.21. Cleaning the Plexiglas base with a piece of anti-static tacky cloth.

2. Ensure that the eight steel alignment pins are inserted into the holes (2 in each corner).
3. Place four bars of inner frame A over the dowel pins and onto the Plexiglas base after wiping them with an anti-static cloth. Ensure that the adhesive side is facing up.

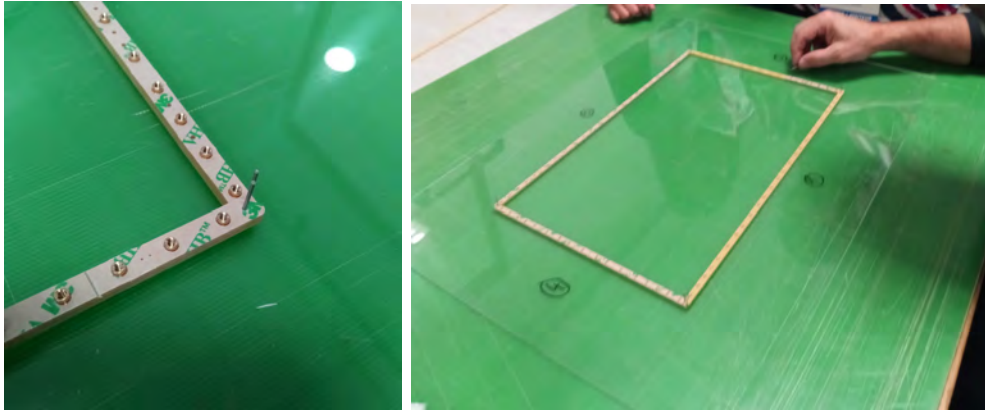


Figure 4.22. Placing dowel pins for alignment and setting up inner frame A.

4. In one of the long bars, there are extra holes designed for the sockets of the HV pins to be soldered to the drift layer. Additionally, the GEM foils have connections that run from the top and bottom layers of the foil for high voltage operation.



Figure 4.23. Extra holes on one side of inner frame A bar and on the drift foil for HV connections.

5. On the dowel pins, place the pre-stretched drift foil attached to the green canvas for test fit alignment and then remove it.
6. Remove the covering sticker from the adhesive layer using a scalpel if necessary. Remove any residues or crumbles that may remain.

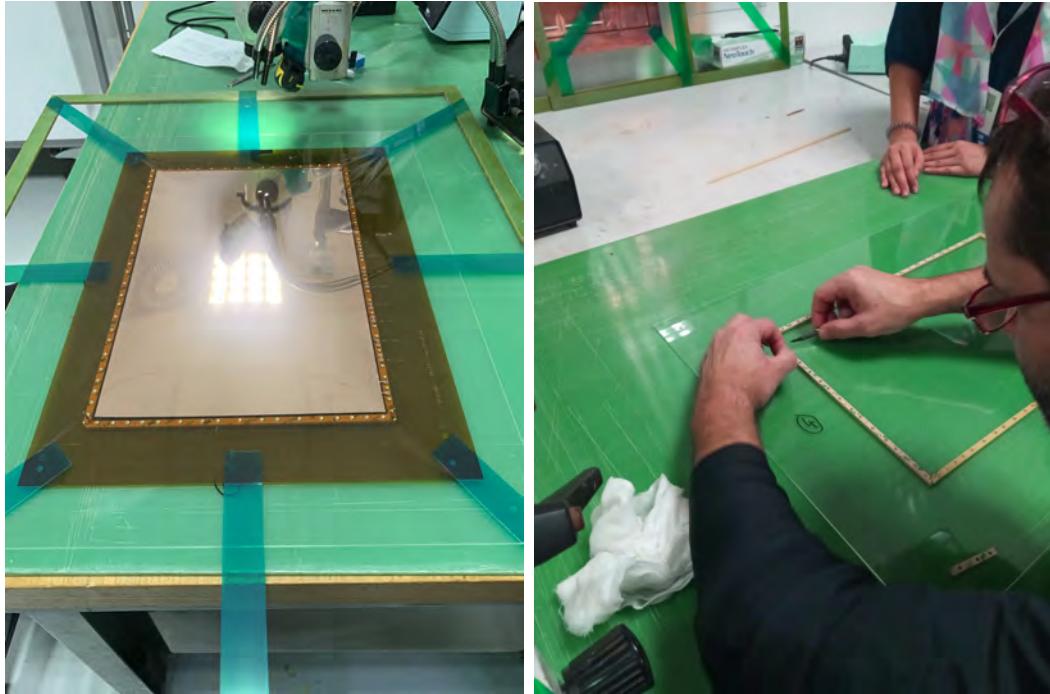


Figure 4.24. Test fitting drift layer on inner frame A bars and removing adhesive sticker from the inner frame A.

7. With tacky roller, clean both sides of the drift foil to remove any dust particles.



Figure 4.25. Tacky roller (left) and cleaning of the drift foil using tacky roller.

8. Overlay the canvas with the drift foil over the eight dowel pins making sure the conductive side is facing up. While the foil is still on the green canvas, cut off old tape and fix it with new tape to the Plexiglas and slightly pre-stretch it.



Figure 4.26. Placing the drift foil onto the frames while on green canvas and adjusting and pre-stretching the drift foil using green tape

9. Carefully press down the drift foil onto adhesive frame pieces using an anti-static, tacky cloth.
10. Fix the drift foil with tapes to the Plexiglas. Pre-stretching must be performed carefully once again as it is glued on to the inner frames. Using the tacky roller, clean the drift foil again.



Figure 4.27. Pressing down the drift foil onto the adhesive strips using the tacky cloth and cleaning the drift foil using tacky roller after final pre-stretching.

11. Place the HV pins on the drift layer, and the pins will adhere through the designated holes of inner frame A.
12. Solder the HV pins to the drift foil and finish off by removing and cleaning any residue with alcohol and tacky wipes.

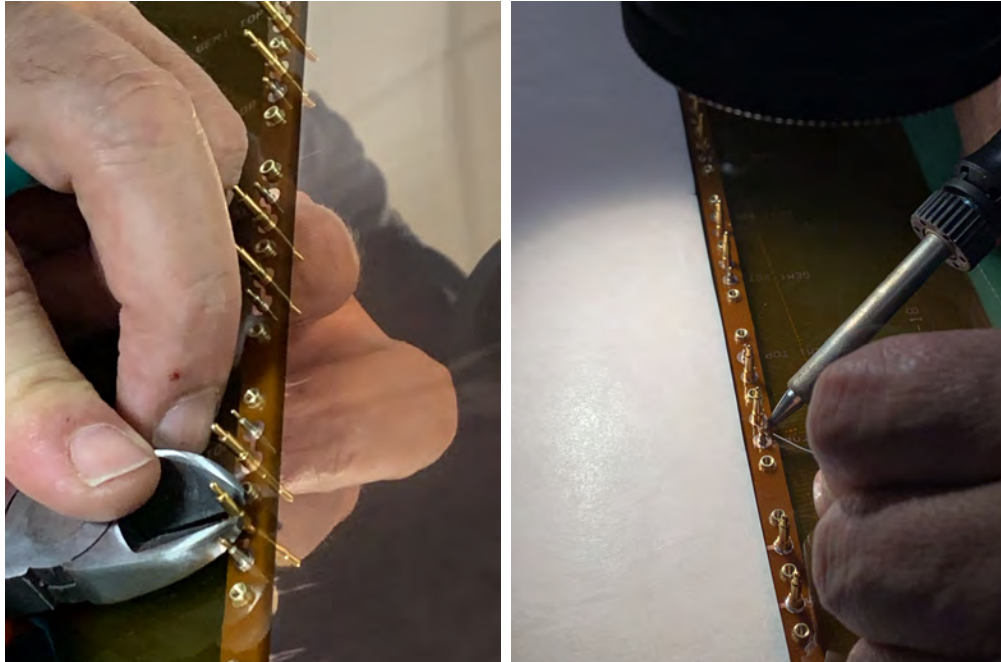


Figure 4.28. Fixing the spring loaded pins for HV connections and carefully soldering them to the drift foil.

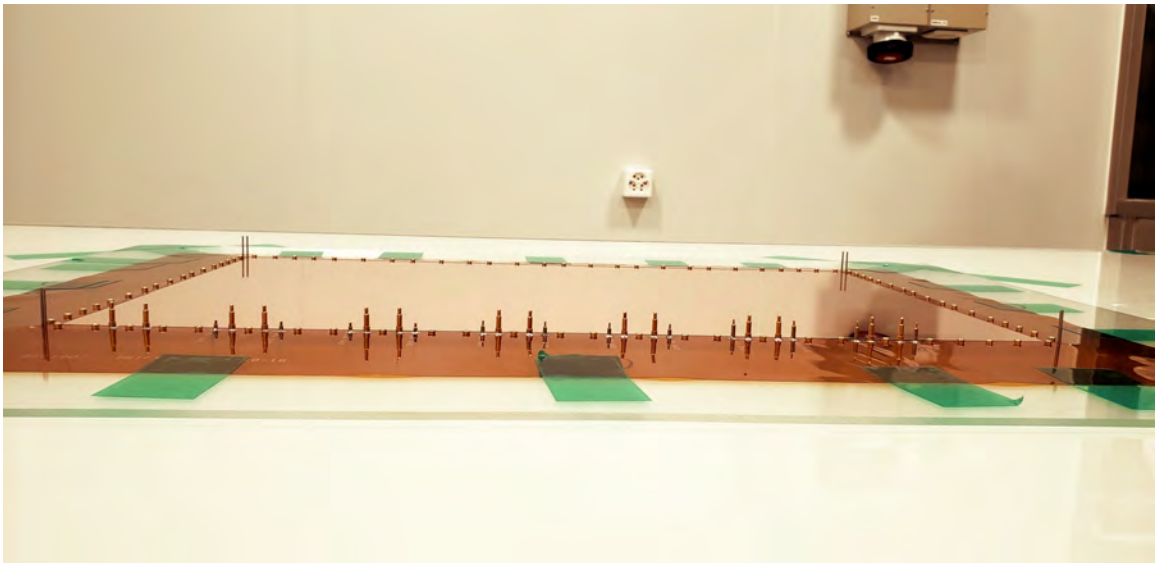


Figure 4.29. Drift foil with all the spring loaded pins attached.

Next, the GEM foils G1, G2 and G3 are stacked up alternating with inner frames B to E. And finally stack the Readout board and lastly inner frame F. Therefore, the

next set of steps were carried out inside the clean room to make sure there are no dust particles or humidity involved to create any discharge issues inside the chamber.

1. Slide the inner frame B bars carefully through HV pins and dowel pins.

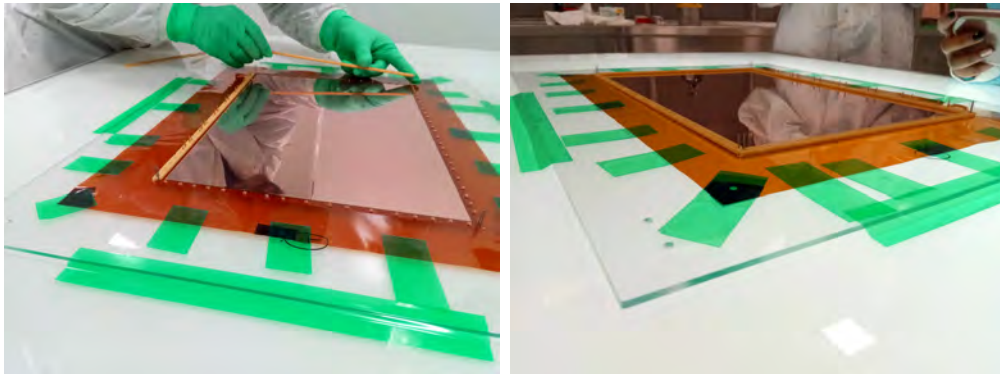


Figure 4.30. Placing inner frame B on the drift foil.

2. Take out the pre-stretched G1 foil and clean both sides using the tacky roller and test the foil with Megger MIT430/2 insulation tester to make sure the resistance is $> 100G\Omega$ when supplied with 500V.
3. The GEM foil is stacked upside down, so the top (G1T) will point up and the bottom (G1B) will point down. Clean the foil with tacky roller and flip the GEM foil, G1T facing down and pre-stretch the GEM foil in the same manner that the drift foil was pre-stretched while on the green canvas.
4. Pre-stretch the G1 foil with additional tape in order to eliminate wrinkles in the active region, if present. Then remove the green canvas.

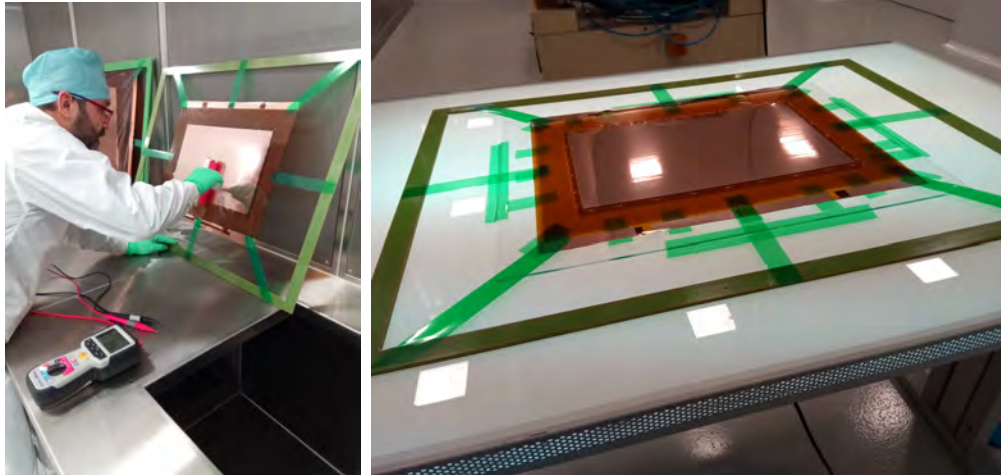


Figure 4.31. Testing the G1 foil and stretching it on the inner frames B.

5. It is important to note that 4 spring loaded pins will be covered by the GEM foil G1 and it will make high voltage connections to Top(G1T)) and Bottom(G1B) layers of G1 GEM foil.
6. As shown in Figure 4.23, the GEM foils have HV connections to top and bottom layers of the foil. It is necessary to cut off the remaining holes so that the spring loaded pins for the next two layers can stick through them.

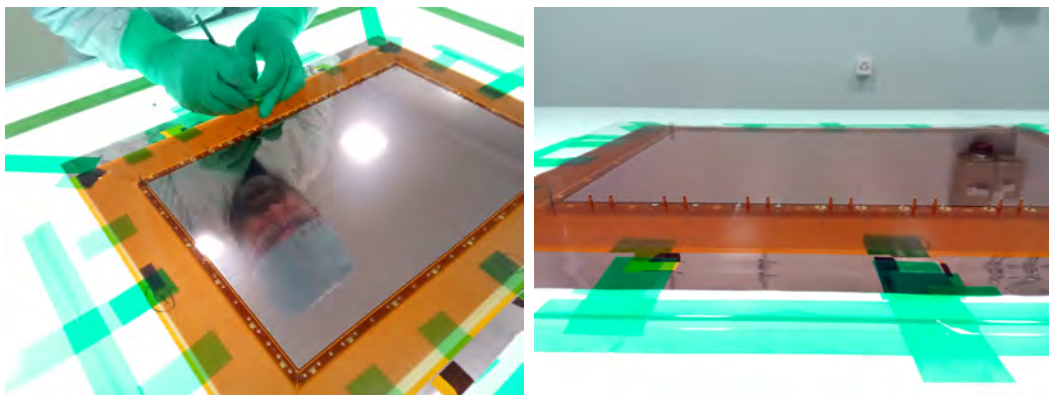


Figure 4.32. Keep the foil connections for hv connections for G1T and G1B layers and cut-off other marked holes.

7. Clean the G1 foil with tacky roller and test G1T and G1B layers by applying 550V and measuring resistance and current to ensure that the high voltage pins are properly positioned.

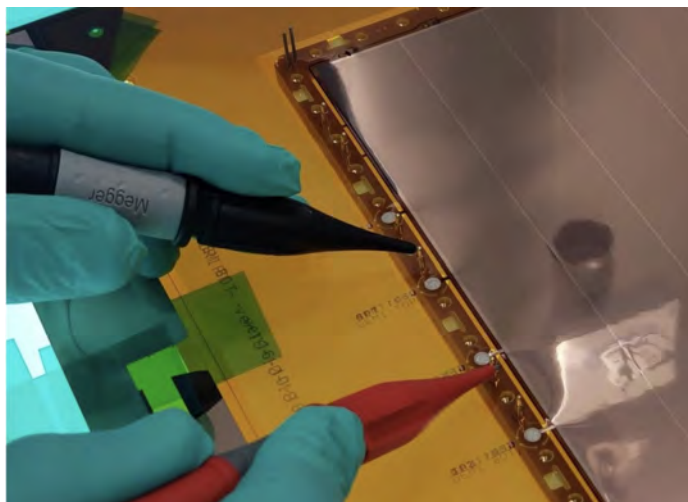


Figure 4.33. Testing connection between hv spring loaded pins is conducted after each layer of foil is stacked.

8. Place the inner frames C carefully through the HV pins and dowel pins onto the G1 foil.
9. Take out the pre-stretched G2 foil and clean both sides using the tacky roller and test the foil with Megger MIT430/2 insulation tester to make sure the resistance is $> 100G\Omega$ when supplied with 500V.
10. Clean G1 foil with tacky roller before placing the flipped G2 foil(G2T facing down). Then, pre-stretch G2 foil using tape and remove green canvas.

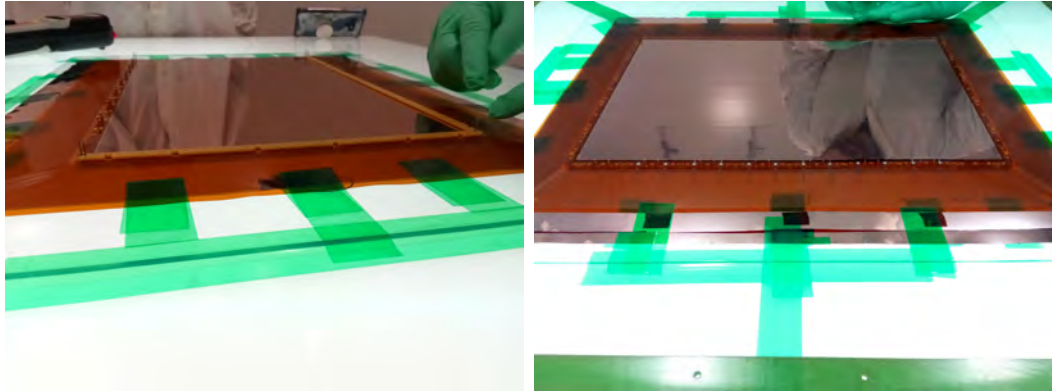


Figure 4.34. Placing the inner frames C on G1 foil and pre-stretching G2 GEM foil.

11. 4 spring loaded pins in the middle will be covered by the GEM foil G2 and it will make high voltage connections to Top(G2T)) and Bottom(G2B) layers of G2 GEM foil. The remaining hv foil connections are cut-off while keeping the connections only for G2 GEM foil.

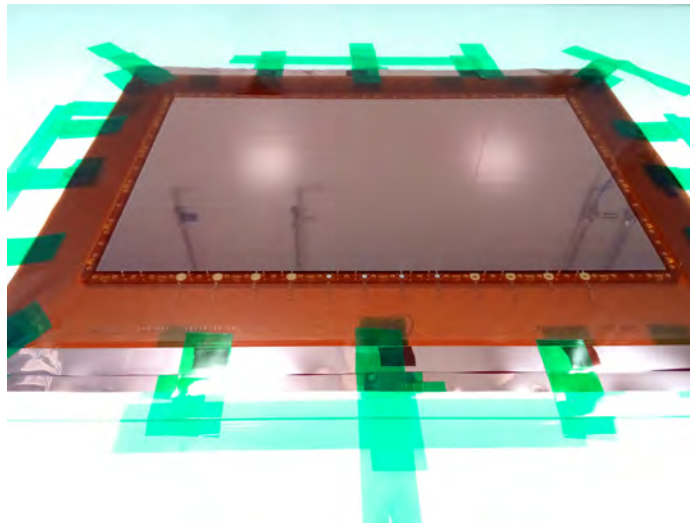


Figure 4.35. Keep the foil connections for hv connections for G2T and G2B layers and cut-off other marked holes.

12. Then clean the G2 foil with tacky roller and test G2T and G2B layers by applying 550V and measuring resistance and current to ensure that the high voltage pins are properly positioned.

13. Insert the T-nuts through inner frame C and B. These are designed to use for horizontal stretching when the stack is closed.

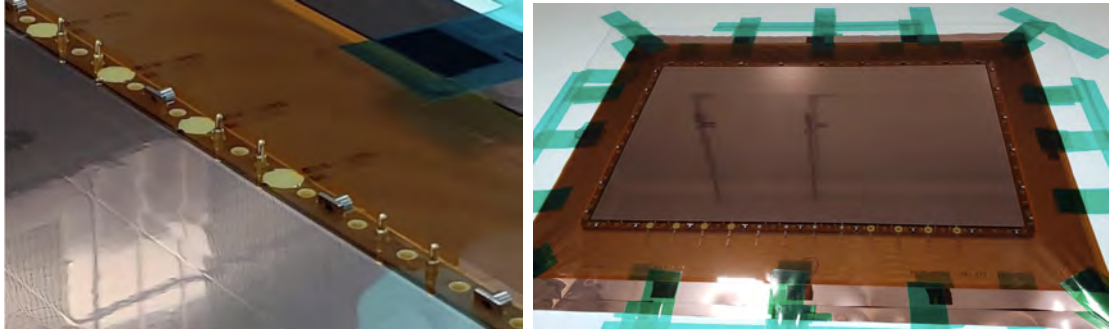


Figure 4.36. Inserting T-nuts through inner frames C and B.

14. Before placing the inner frame D bars, ensure that all the T-nuts have been inserted.
15. Then, steps from 9 to 12 are repeated for G3 foil and finally test the hv connections before placing the inner frames E.

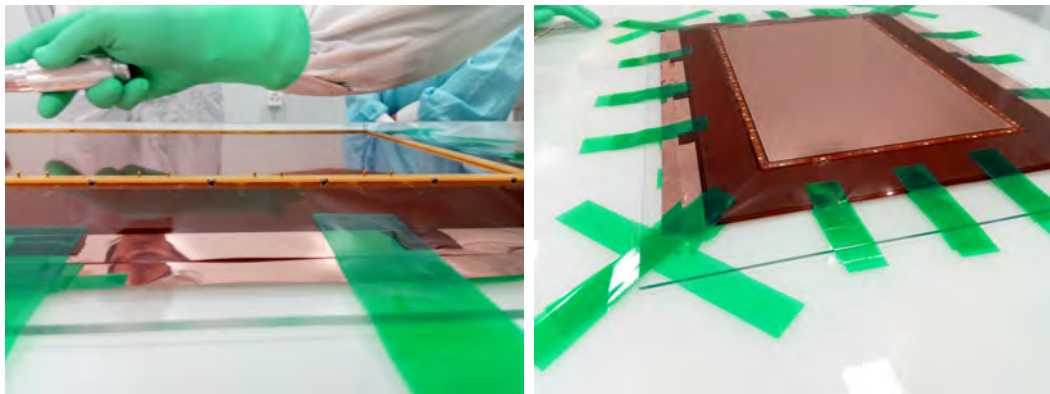


Figure 4.37. Placing inner frames D and pre-stretching of G3 GEM foil.

16. Clean the readout board using the tacky roller and test HV connections.

17. Carefully slide the inner frame E bars through dowel pins and hv pins on to the G3 GEM foil. A total of fourteen (14) spring-loaded hv pins will point to the Readout layer, which will be covered by the Readout layer.
18. Clean the G3B side of the G3 foil, as well as the active side of the Readout foil again, before flipping over and placing the Readout foil on the stack.

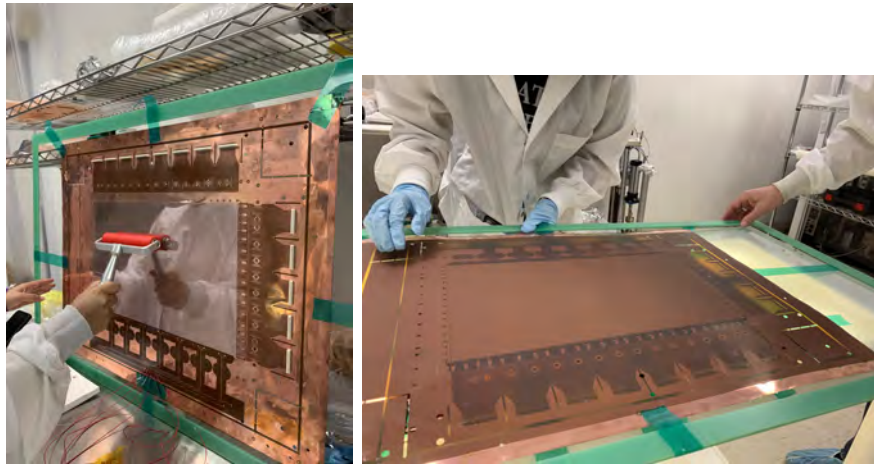


Figure 4.38. Cleaning the active side of Readout board and placing it on the inner frames E.

19. Pre-stretch the Readout foil with tape to ensure that the active area is de-wrinkled and also check the 14 HV pins are properly seated.

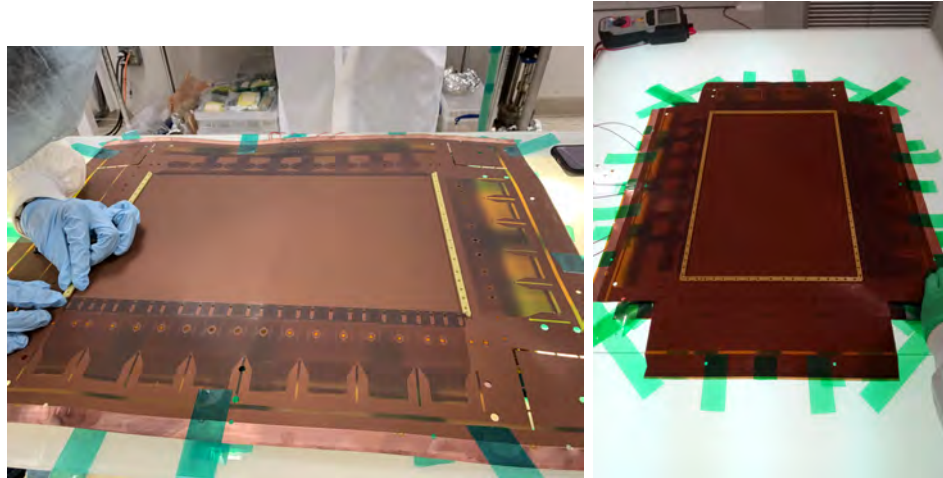


Figure 4.39. Placing inner frames F and pre-stretching the readout board.

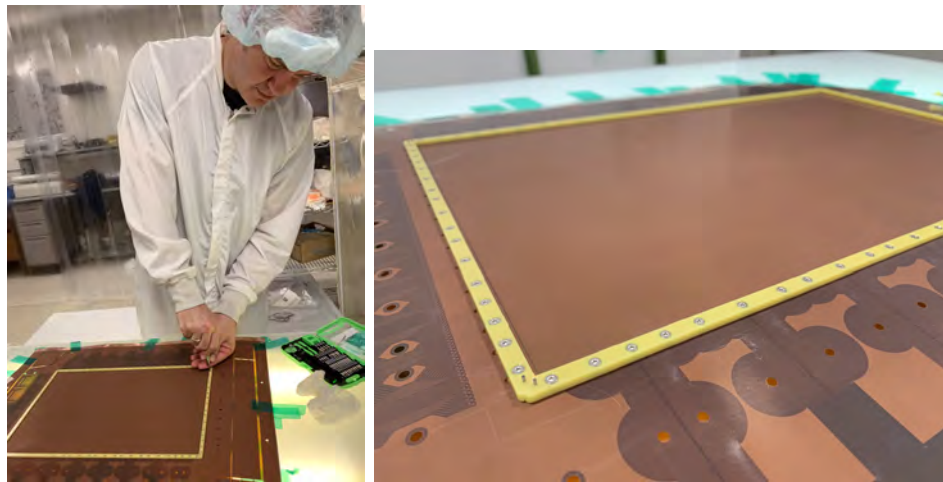


Figure 4.40. Tightening the screws through inner frames E - A and fixing the whole stack.

20. Ensure that the Drift, G1, G2, and G3 layers are electrically connected to the HV inputs on the Readout board. Conduct 550V tests on the GEM foils and measure current and resistance.

4.4.3.2 Foil Stretching

The next most important step is stretching of the foils. Upon completing the stacking of the layers from drift foil to readout board, we shall remove the pre-stretching tapes and dowel pins.

1. Ascertain that all foils have maintained their tension from pre-stretching and that the inner stack is not bulging or deforming.
2. Remove dowel pins and pre-stretching tapes and also remove the Plexiglass base from the stack.
3. Flip the whole stack right side up. Now the drift foil layer should be on top.
4. Perform electrical tests. Test the resistance from the readout plane using the externally connected wires.

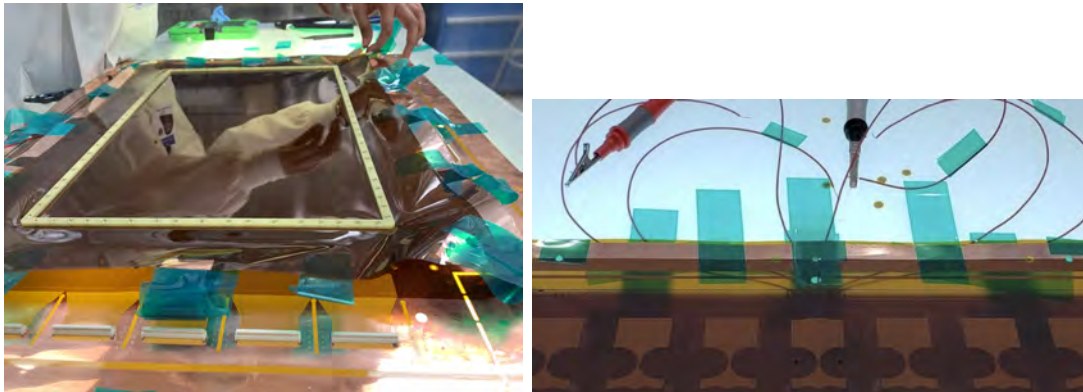


Figure 4.41. Flip the whole stack and test all the layers for electrical connections.

5. To prevent the readout board from being damaged or cut accidentally, secure a tape around its inner edge.
6. After confirming that the inner stack is mechanically and electrically sound, cut the foils on the outer sides of the inner frame bars, starting from excess drift layer and cutting off the G1, G2, G3 layers.



Figure 4.42. The GEM foil stack after cutting off excess foil.

7. The outer main frame should now be placed around the foil stack, and it should sit on the readout board.

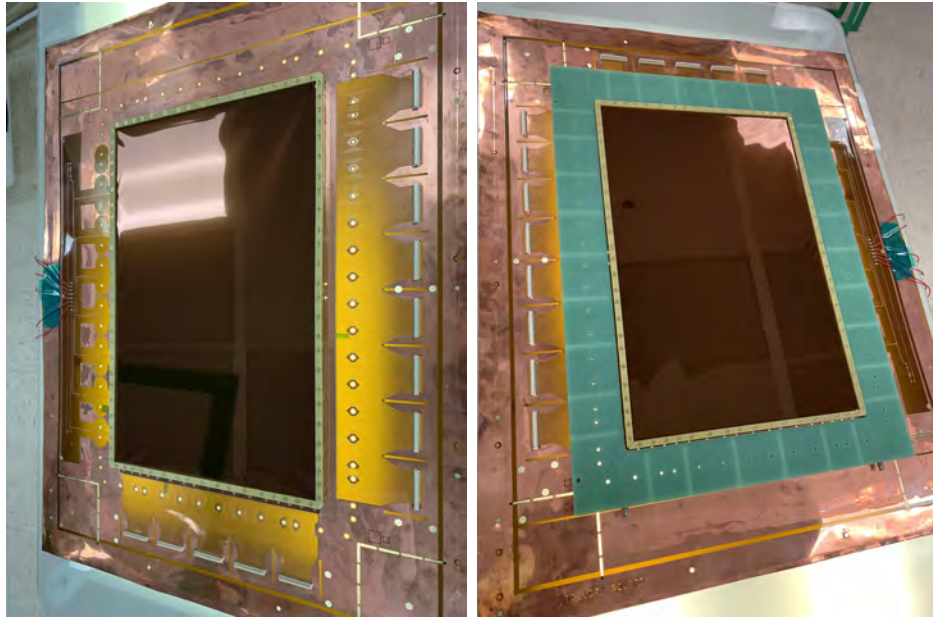


Figure 4.43. The GEM foil stack after cutting off excess foil and after placing the outer frame.

8. Attach the horizontal screws to the nuts by inserting them horizontally. It is now possible to tighten the screws gently in all four directions in order to stretch the foils.

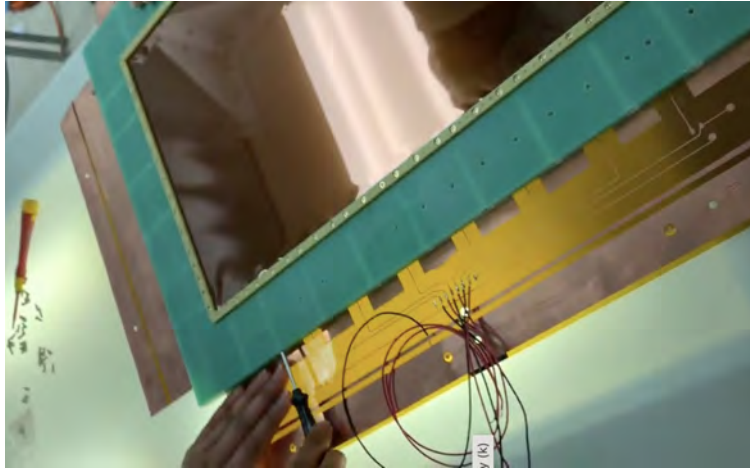


Figure 4.44. Stretching of the foils by tightening the horizontal screws

9. Two individuals must stretch simultaneously in opposite directions, ensuring that the gap between the inner and outer frames is the same.

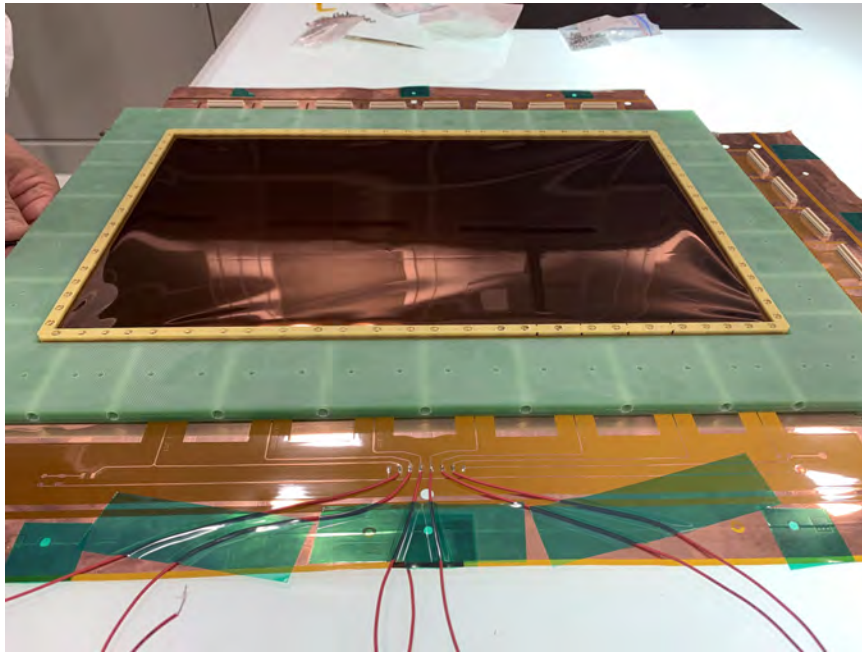


Figure 4.45. The GEM foil stack before stretching.

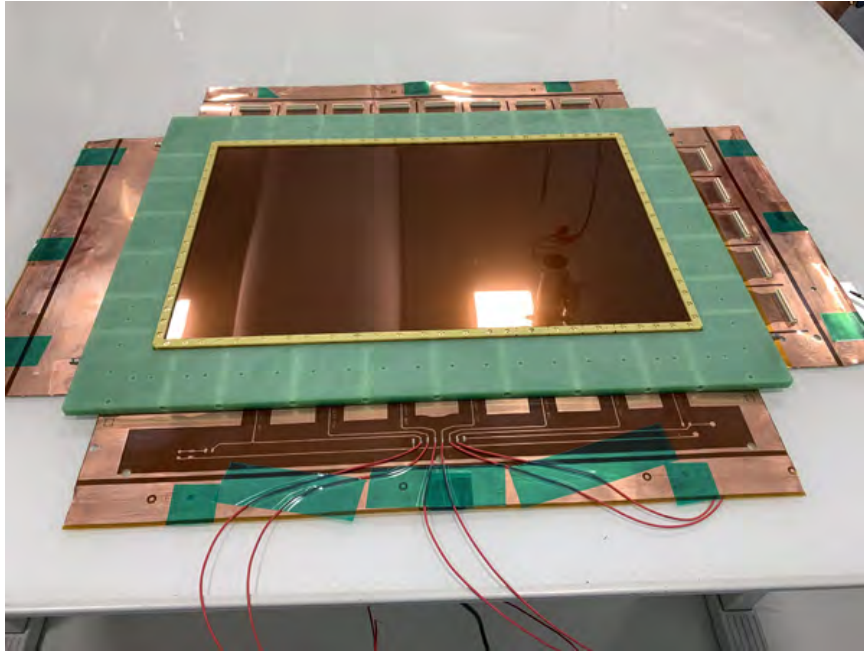


Figure 4.46. The GEM foil stack after stretching.

10. Finally perform electrical tests. Test the resistance from the readout plane using the externally connected wires.

4.4.3.3 Closing of the Chamber

For protection against the environmental factors such as dust and humidity, the detector must be sealed with top and bottom covers. The gas distribution system and the HV connections will be tested after the chamber has been sealed.

1. As the gas enters on one short end, it flows through the gas inlets on the inner frames, through the foil's active area, and exits on the other short end.
2. To ensure high gas flow efficiency, rubber o-ring pieces are used to obstruct the flow of gas on the long side of the detector and only allow it to flow through the active area.

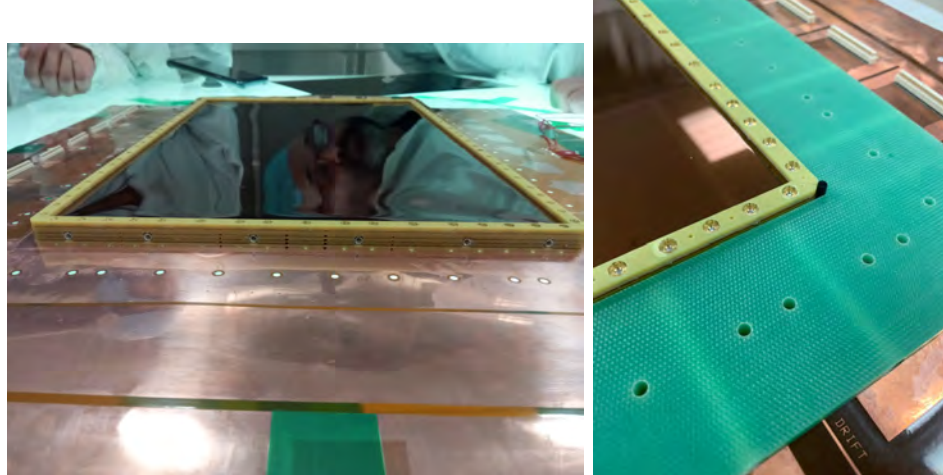


Figure 4.47. The gas inlets/outlets through short bars of inner frames (Left), O-ring pieces are placed to ensure gas flows through active area (Right).

3. The top cover with embedded nuts measures 37 cm × 47 cm and bottom cover measures 47 cm × 57 cm.
4. Using the tacky roller, clean the inner side of the gas foil window by placing the top cover upside down on the table.
5. Clean the drift foil using the tacky roller and place the prepared top cover to close it.

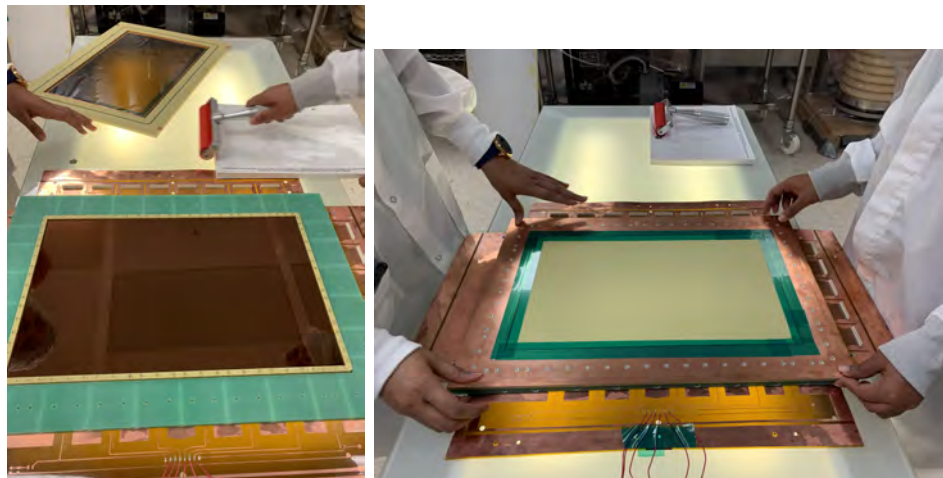


Figure 4.48. Cleaning the top cover and drift foil using tacky roller and placing the cover on GEM stack.

6. Then flip the whole detector. Now it should sit on top cover and the Readout layer should sit on the top. Clean the readout layer and inner side of the gas foil window of the bottom cover.
7. Place the bottom cover on top of the readout board.

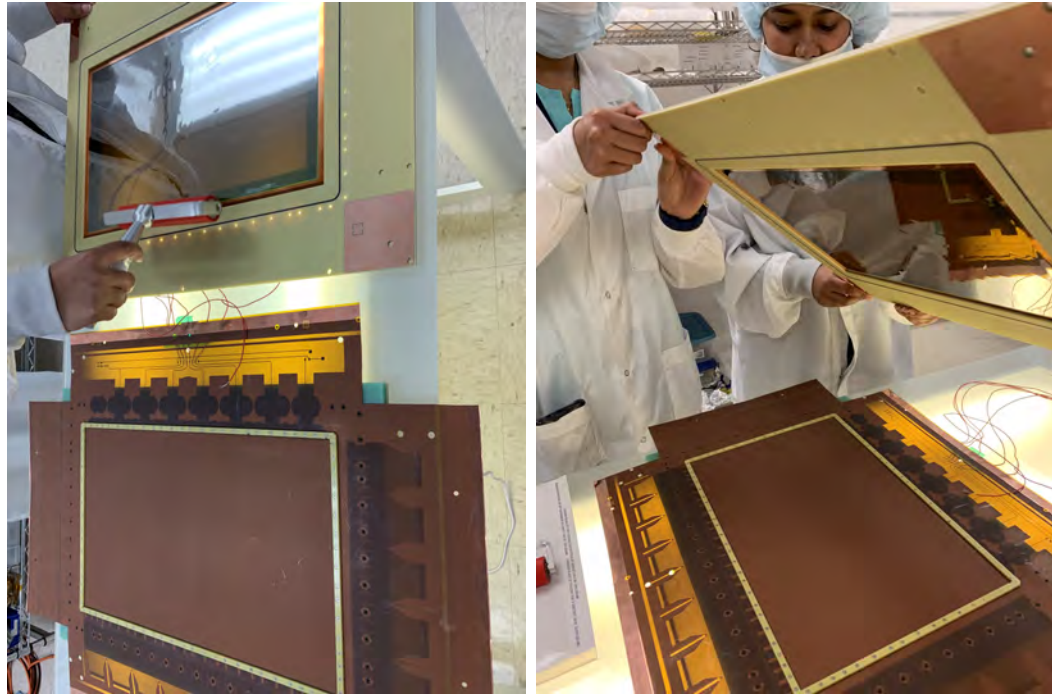


Figure 4.49. Cleaning the bottom cover and readout layer using tacky roller and placing the cover on RO layer.

8. Insert the screws from top and it will grip the embedded nuts in the other cover on the bottom.



Figure 4.50. Closing the chamber by inserting screws through bottom cover.

9. Finally, M6 screws are inserted to seal the openings where horizontal screws are located



Figure 4.51. Placement of M6 screws through openings where horizontal screws sit (Left).

10. Gas window foils are covered with the cutouts from the top and bottom covers until they are tested and commissioned.

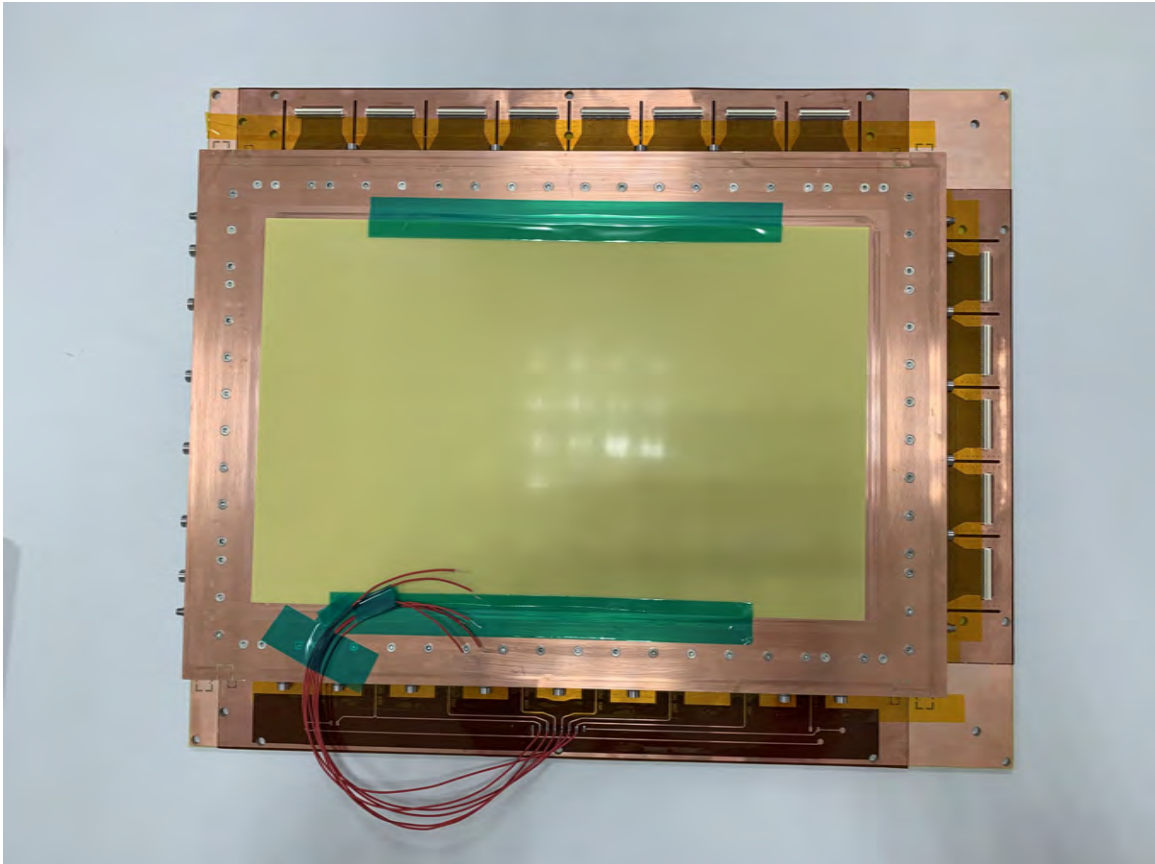


Figure 4.52. Fully closed GEM detector.

4.5 Electronics, DAQ System and COOKER Framework

GEM signals are read out using the APV25 frontend cards. A total of 128 ADC channels are read out by each device. The longer side of the detector is equipped with 8 APV25 cards, and shorter side is equipped with 5 APVs. Therefore, each GEM plane has a total of 1625 readout channels, of which 1000 channels are on Y axis and 625 channels are on X axis.

Each APV25 transmits 12 bit ADC data words and slow control data to the MPD board of the VME-based Multi-Purpose Digitizer (MPD). Then, the data is transferred to the DAQ system for further data processing.

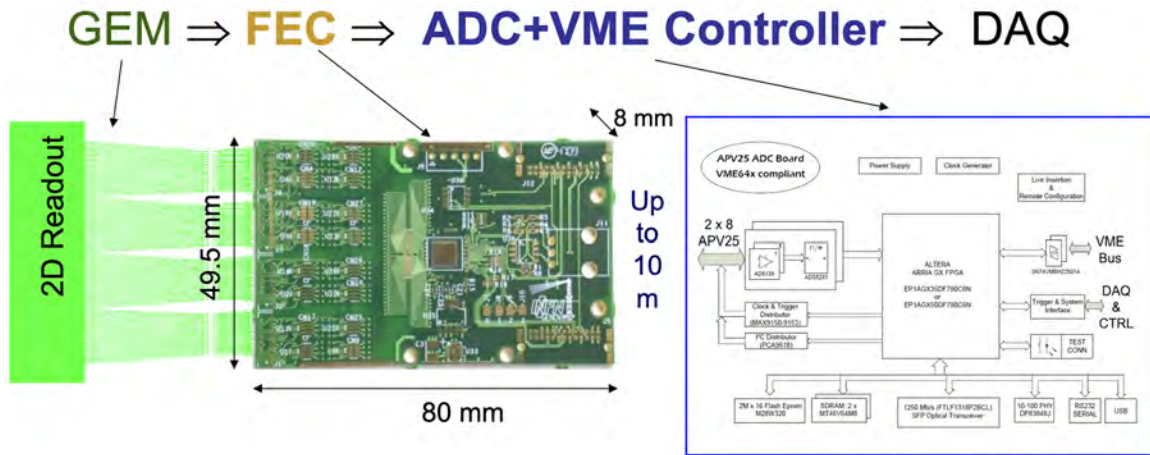


Figure 4.53. Readout system of GEM detector.

4.5.1 APV25

The Analog Pipeline Voltage (APV25) card is composed of 128 channels and has a low noise level and low power consumption. The frontend cards and VME controllers are developed by INFN Rome for JLab/SBS project by S. Frullani, E. Cisbani, P. Musico. APV25 frontend cards are primarily used due to its radiation hardness and relatively low cost per channel. There are 128 channels of pre-amplifiers and shapers on this chip that drive a 192 column analogue memory. As part of the analog data, there is a digital header, a digital address and an error bit, as well as an analog data stream consisting of 128 clock cycles, which corresponds to the signal size of 128 channels. An operating frequency of 40 MHz is used by the chip and it outputs a differential current signal in the range of $\pm 4mA$. The I2C standard is utilized for the configuration, bias settings, and error codes.

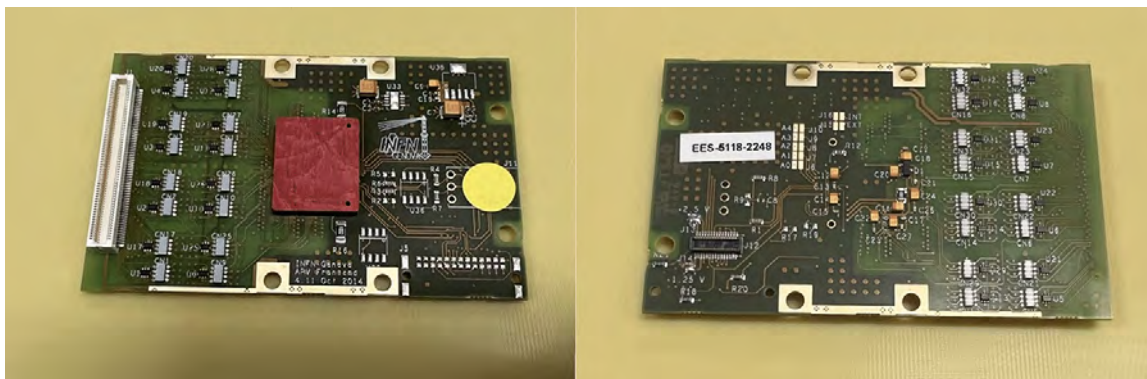


Figure 4.54. APV Frontend (INFN Geneva - Rev 4.11 Oct 2014) front and back.

APV25 cards are directly connected to the readout board and then gets connected to backplanes.

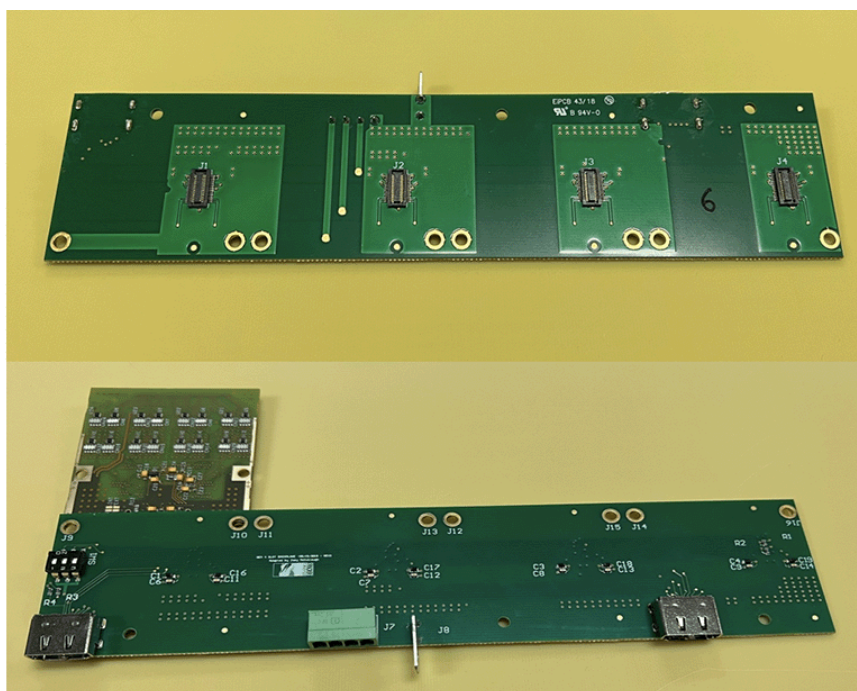


Figure 4.55. APV Frontend card on GEM 4 slot backplane (Rev3).

4.5.2 MPD

The Multi Purpose Digitizer (MPD) board developed also by INFN can be configured to handle up to 16 APV25 frontend cards. An MPD board is capable of

receiving analog data streams and converting them to digital signals. Furthermore, it is capable of transmitting control and configuration signals to the APV25 frontend cards. Figure 4.56 shows the difference between MPD versions 3.0 vs. 4.0



Figure 4.56. MPD Rev3.0 (Left); MPD Rev4.0 (Right).

In order to run MPD version 3.0, HDMI-B cables were required, which are expensive and difficult to obtain. With version 4.0, it avoids using these HDMI-B cables, instead uses HDMI-A cables. The main difference is the Field Programmable Gate Array (FPGA) that's used in as the core of the board. Some features of the MPD Rev 4.0 includes 12 bit ADC, I²C configurations for APV25 cards, APV25 triggering and improved signal to noise ratio in converted data. The modified MPD 4.0 firmware will also allow remote configuration to The board is designed to fit in a VME-64x VXS crate. To compensate for cable delays, the ADC clock phase can be adjusted. Figure 4.57 shows the block diagram for MPD Rev 4.0.

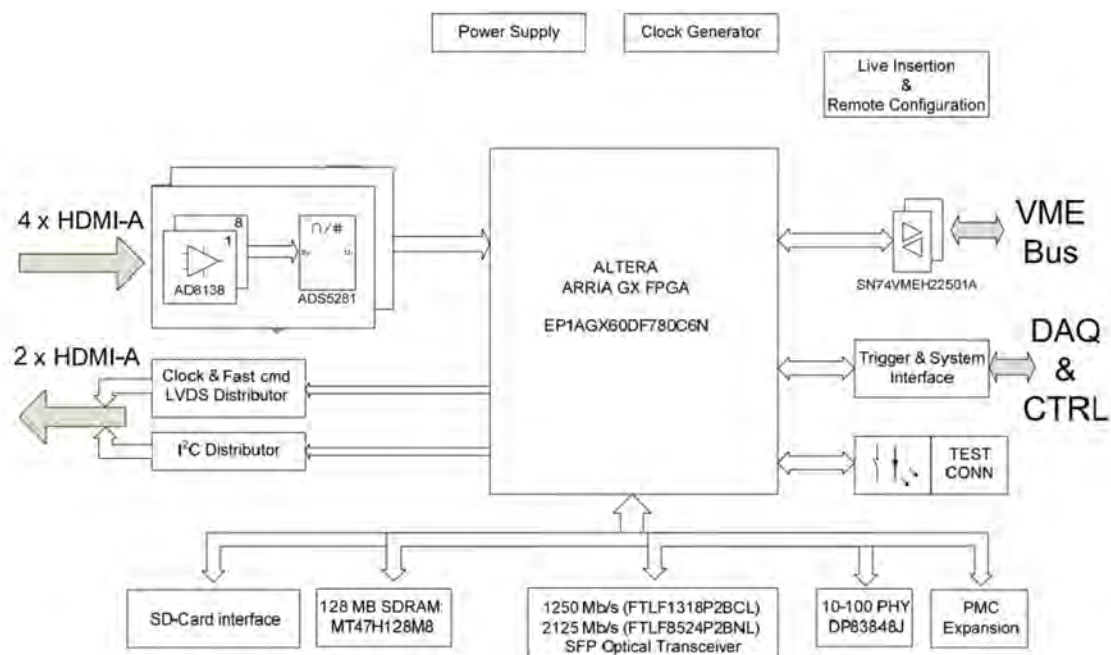


Figure 4.57. Block diagram for MPD Rev 4.0.

4.6 Testing and commissioning

4.6.1 Gas Leak Testing

Gas leak testing is a crucial procedure performed to assess the functionality of GEM detectors and ensure their reliable operation. These detectors typically operate in high voltage, the presence of gas leaks can result in altered electric fields, reduced gas gain, and increased background noise, all of which can significantly affect the detector's performance and data quality.

First, before conducting gas leak testing with hydrogen, it is common practice to flush nitrogen into GEM detectors to ensure a clean and controlled gas environment inside the detector before actual operation. This initial step serves multiple purposes in the testing process. Nitrogen, being an inert gas, helps to remove any residual contaminants or impurities that may be present in the detector chamber. Furthermore, it can also help to eliminate the presence of oxygen, which can be detrimental

to the detector's operation. Oxygen molecules have a higher electron attachment rate compared to other gases commonly used in GEM detectors, which can lead to electron recombination and reduced detector performance. By replacing oxygen with nitrogen, the detector can maintain a more stable and efficient operation.

To check the gas flow rate, the GEM detector was supplied with nitrogen gas, with the nitrogen supply from LERF directly connected to the flow meter. The outlet from the flow meter was then fed into the GEM detector, and the outlets from the GEM detector were connected to a bubbler. It took some time for the bubbles to appear in the bubbler due to pressure buildup. The bubble rate observed through the GEM detector was measured to be 68 bubbles per minute, while the direct gas supply had a bubble rate of 96 bubbles per minute. Based on these approximate numbers, it was assumed that there was a loss of approximately 30% in the gas supply through the GEM detector.

Then we started gas leak testing process, by introducing the hydrogen admixture (air/hydrogen 2.02%) into the detector. Hydrogen gas detector was employed to detect the presence of hydrogen gas outside the system. Through this testing, we discovered gas leaks in the detectors on the main frame, specifically near the bolt fixtures. It was observed that the main frame had suffered small openings around these areas, which were likely the source of the leaks. These openings were identified and sealed using epoxy.

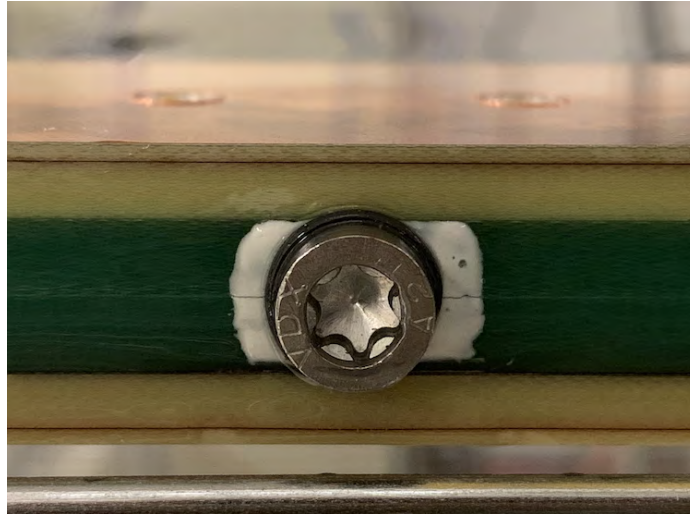


Figure 4.58. The potential gas leak openings were sealed using epoxy.

After sealing the GEM detectors with epoxy, no further gas leaks were detected. This indicates that the epoxy effectively closed any small openings or gaps in the detectors, ensuring a gas-tight seal.

4.7 Results

The GEM detectors underwent individual high voltage tests for the foils and were found to operate successfully with nitrogen (N₂) at a voltage of 4,300 V. In addition, the setup was prepared for electronics testing, including the APV, backplanes, patch panels, HDMI cables, MPD, and VME. Testing in histogramming mode with a 10Hz pulser showed satisfactory results, and the event mode with a standalone program was also functioning properly. The addressing, configuration, and mapping of the APVs were successfully implemented.

Three out of the eight GEM detectors were sent to Sendai, Japan for the Ultra Low Q^2 (ULQ2) experiment at Research Center for Electron Photon Science (ELPH), Tohoku University, Sendai, Japan. These three GEM elements, were utilized at ULQ2@ELPH and commissioning of the experiment began in the fall of 2019. The three GEM planes were specifically designed for position determination. The pri-

mary purpose of the commissioning was to characterize the spectrometer optics and facilitate accurate tracking during the experiment.

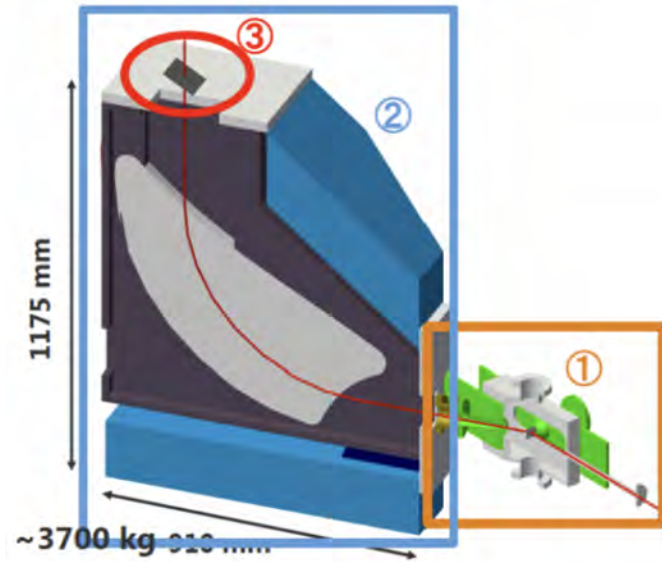


Figure 4.59. The positioning of the GEM detectors at ULQ2@ELPH experiment during 2019 beam time.

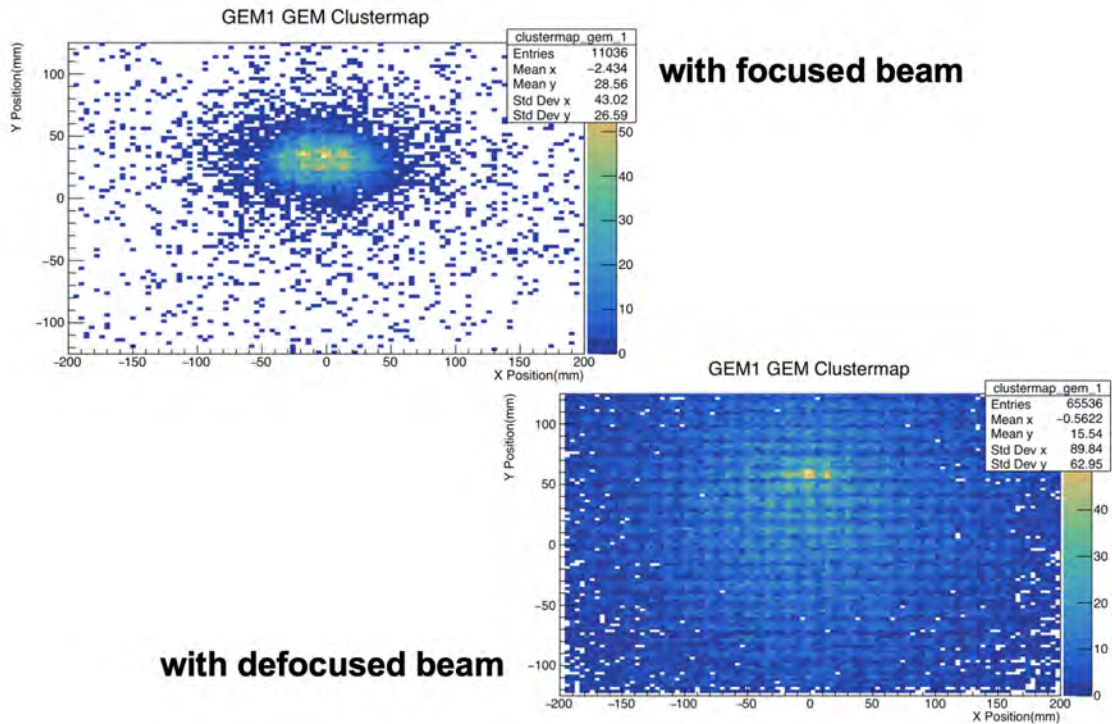


Figure 4.60. The cluster distribution of GEM detectors for focused beam and defocused beam.

It can be noticed in Figure 4.60, the cluster distribution exhibits a grid-like structure, which is likely a result of the encoding and decoding of ADC bits information. Despite the raw nature of the plots, the presence of a distinct beam spot can be clearly observed.

With the introduction of new firmware, MPD modules, and APVs, we anticipate obtaining data with an enhanced system in the near future. These updates hold the promise of improving the overall performance and capabilities of the system, leading to more accurate and reliable data acquisition. The detectors are currently being prepared to test with cosmic rays at LERF. Taking cosmic ray data will provide valuable insights into the performance of these detectors. Cosmic rays, being high-energy particles originating from outer space, can effectively probe the detector's response and characteristics. By analyzing cosmic ray data, we can study the detector's efficiency, resolution, noise levels, and other important parameters.

CHAPTER 5

MUSE EXPERIMENT

5.1 Motivation

The complex internal structure of the proton has led researchers to study some of its intrinsic properties, such as angular momentum and charge radius, using various experimental methods. The root-mean-square charge radius, denoted as R_E , is defined as $\sqrt{\langle r^2 \rangle}$ and represents the spatial extent of the proton's charge distribution. It has regained significant attention due to the discrepancy in experimental values between muonic hydrogen and measurements using electrons. Precise measurement of the proton's charge radius is important for understanding quantum electrodynamics (QED) calculations of energy levels of atoms, quantum chromodynamics (QCD) calculations in the non-perturbative region, and the Rydberg constant [28].

The hydrogen atom has been an excellent candidate for measuring the proton's charge radius because it consists of a single proton in its nucleus, orbited by one electron. Two established techniques are used for measuring the proton charge radius: the nuclear scattering method and the spectroscopy method.

In scattering experiments, high-energy electrons are directed at hydrogen atoms, and the proton charge radius can be determined by analyzing the resulting electron scattering. This method involves measuring the cross-section of elastic electron-proton scattering and extracting the proton's electric form factor, denoted as G_E^p . By observing the slope of G_E^p as the four-momentum transfer squared, Q^2 , approaches zero, it becomes possible to determine the proton's charge radius.

$$\langle r_p^2 \rangle \equiv -6 \frac{dG_E^p(Q^2)}{dQ^2} \Big|_{Q^2=0} \quad (5.1.1)$$

In the spectroscopic method, the transition frequency between two energy levels of a hydrogen atom is measured to calculate the proton's radius. One commonly used transition for this purpose is the hydrogen Lamb shift transition.

Prior to 2010, the results obtained from these two methods, spectroscopy and elastic electron-proton scattering experiments, were generally consistent with each other in determining the proton's radius (r_p). According to Committee on Data for Science and Technology (CODATA-2010), the values for r_p obtained from hydrogen spectroscopy and $e-p$ elastic scattering experiments were 0.8758(77) fm and 0.895(18) fm, respectively [29].

In the same year, the agreement between the two methods was further supported by the findings of a high-precision elastic electron-proton scattering experiment conducted at the Mainz Microtron (MAMI) [11]. This particular experiment involved collecting a significant amount of cross-section data points spanning a range of Q^2 values, specifically from 0.004 to 1 (GeV/c)². The analysis of this experiment yielded a proton charge radius value of 0.8791(79) fm. Subsequently, based on these results, the CODATA-2010 recommended and published a value of r_p as 0.8775(51) fm [29].

In 2010, an extremely precise calculation of the proton charge radius was conducted based on muonic hydrogen Lamb shift measurements. The reported value for the proton charge radius was 0.84184(67) fm [10]. This new measurement was 4% smaller and 10 times more precise than the previously released CODATA-2010 value. In 2013, another experiment yielded 0.84087(39) fm [13]. This discrepancy between electronic and muonic measurements was unexpected, given that the interactions of muonic and electronic particles with protons were expected to be the same according to the Standard Model. This 7σ discrepancy of charge radius measurements originated the proton radius puzzle.

A recent electron scattering experiment, namely the Proton charge radius (PRad) experiment at Jefferson Lab, has favored a smaller radius, $R_p = 0.831 \pm 0.007(stat) \pm$

0.012(*syst*) fm [12]. The technique employed in the PRad experiment involved the use of a calorimeter-based approach that did not rely on a magnetic spectrometer. The PRad experimental setup covered Q^2 range from 2×10^{-4} to 6×10^{-2} (GeV/c)² which is the lowest Q^2 value covered by a $e - p$ scattering experiment. However, this result disagrees with the Mainz data at the cross-section level [11]. The PRad experiment's smaller value for the proton charge radius is still subject to ongoing debate and scrutiny in the scientific community, and more experimental and theoretical work is needed to resolve the discrepancy with the Mainz data.

New hydrogen spectroscopic results have been published since 2010, including the 2S-4P transition frequency measurement in 2017 which reported a proton charge radius of $r_p = 0.8335(95)$ fm [14]. In addition, the 1S-3S transition frequency measurement published in 2018 determined the proton charge radius to be $r_p = 0.877(13)$ fm [15]. More recently, the 2S-2P Lamb shift measurement conducted in 2019 yielded a value of $r_p = 0.833(10)$ fm [16]. Notably, the 2017 and 2019 measurements are very similar and both agree with the muonic hydrogen measurements, while the 2018 measurement aligns with the CODATA-2010 value. According to CODATA-2018, the proton charge radius was published as (0.8414 ± 0.0019) fm, further supporting the smaller measurements obtained from muonic hydrogen experiments [17]. These measurements are summarized in Figure 5.1.

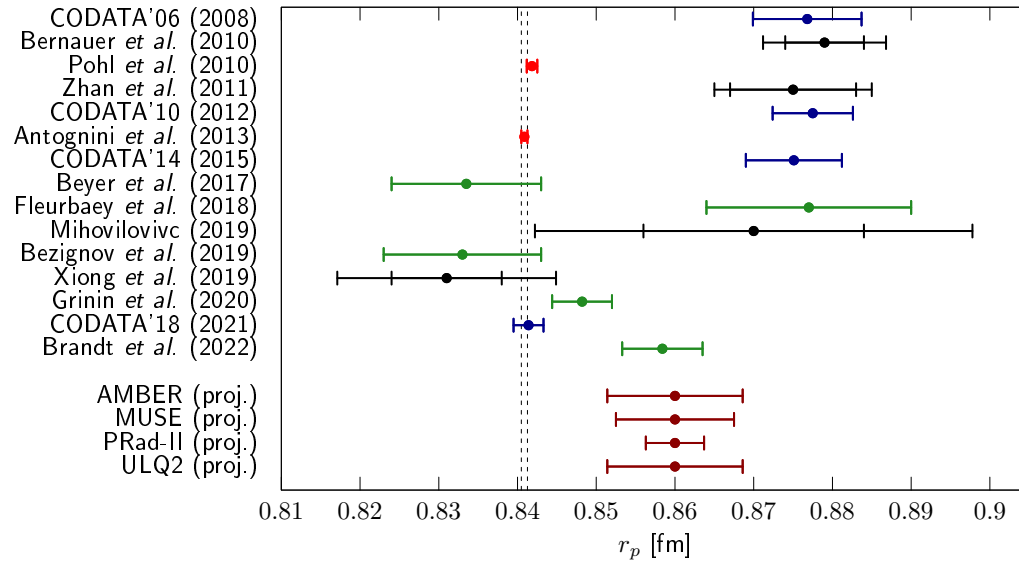


Figure 5.1. Proton radius measurements over the years of 2010-2020 using electron scattering and spectroscopic measurements shown with CODATA compilations [10–17] - Image courtesy: Jan C. Bernauer.

To address the proton radius puzzle, several experiments are currently ongoing or scheduled to begin in the near future. One of these experiments is the MUSE experiment at the Paul Scherrer Institute (PSI) in Switzerland. The MUSE experiment is specifically designed to achieve the first precise measurement of the proton radius through muon-proton scattering. It aims to compare the scattering of muons and electrons within the same experimental setup, providing valuable insights into the charge distribution of the proton [1, 30, 31].

5.2 Proton Charge Radius Measurements

5.2.1 Elastic Electron-Proton Scattering

Proton Charge Radius from Proton Electromagnetic Form Factors

To derive the proton radius from form factors, we can start with the electric form factor ($G_E(q^2)$) and the magnetic form factor ($G_M(q^2)$) of the proton, which

describe the spatial distribution of its charge and magnetic properties, respectively, as a function of the four-momentum transfer squared (q^2).

The Sachs form factors ($G_E(q^2)$ and $G_M(q^2)$) are related to the charge and magnetic distributions within the proton:

$$G_E(q^2) = F_1(q^2) - \frac{q^2}{4M^2}F_2(q^2) \quad (5.2.1)$$

$$G_M(q^2) = F_1(q^2) + F_2(q^2) \quad (5.2.2)$$

where $F_1(q^2)$ and $F_2(q^2)$ are the Dirac and Pauli form factors, respectively, and M is the mass of the proton.

In the non-relativistic limit, we can express the form factors as Fourier transforms of the proton charge density ($\rho(r)$) and magnetic current density ($j(r)$):

$$F_1(q^2) = \int \rho(r)e^{i\mathbf{q}\cdot\mathbf{r}}d^3r \quad (5.2.3)$$

$$F_2(q^2) = \frac{i}{2M} \int \mathbf{j}(r) \times \mathbf{q}e^{i\mathbf{q}\cdot\mathbf{r}}d^3r \quad (5.2.4)$$

To extract the proton radius, we focus on the electric form factor ($G_E(q^2)$) at low momentum transfers (q^2). In this region, the form factor is often expanded as a Taylor series:

$$G_E(q^2) = G_E(0) \left(1 - \frac{q^2}{6} \langle r_E^2 \rangle + \mathcal{O}(q^4) \right) \quad (5.2.5)$$

where $G_E(0)$ is the electric form factor at $q^2 = 0$, and $\langle r_E^2 \rangle$ is the mean square charge radius of the proton.

By comparing the above expression with the Sachs form factors relation, we find:

$$G_E(0) = F_1(0) - \frac{1}{4} \langle r_M^2 \rangle F_2(0) \quad (5.2.6)$$

where $\langle r_M^2 \rangle$ is the mean square magnetic radius of the proton.

Solving the above equation for $G_E(0)$ and substituting it back into the Taylor expansion, we obtain:

$$\langle r_E^2 \rangle = -6 \left(\frac{dG_E(q^2)}{dq^2} \right)_{q^2=0} \quad (5.2.7)$$

This equation allows us to extract the proton radius ($\langle r_E^2 \rangle$) from the slope of the electric form factor at $q^2 = 0$. Experimental measurements of the form factors at low momentum transfers are needed to determine the proton radius accurately.

It is worth noting that the derivation above assumes non-relativistic physics and a simple charge and current distribution model. In reality, the proton is a complex system governed by quantum chromodynamics (QCD), and more advanced theoretical and experimental techniques are used to extract the proton radius from form factor measurements.

5.2.2 Upcoming Experiments

A growing number of research efforts have begun to conduct higher precision measurements to understand the structure of proton. The COMPASS collaboration has proposed to investigate elastic scattering of muons at high energies using muon beam-line at CERN with COMPASS++/AMBER experiment. The proton electric form factor will be determined over a Q^2 range of 0.001 to 0.04 (GeV/c)². Protons' charge radius is expected to be determined with a precision of better than 0.01 fm. Another important upcoming project is the PRad-II experiment [32]. It is an upgraded version of PRad experiment to improve precision in extracting charge radius by reducing systematic and statistical uncertainties [12]. It is planned to use an electromagnetic calorimeter together with two planes of tracking detectors with several other important upgrades. Having reached the Q^2 range of 10⁻⁵ GeV², PRad-II will be the first

experiment to provide an accurate and robust estimation of proton charge radius using lepton scattering using three beam energies, 0.7, 1.4 and 2.1 GeV. Another experiment is proposed by the ULQ2 collaboration at Tohoku University, to conduct an electron scattering experiment and use the electron beam at energies from 20-60 MeV with a scattering angle of 30° to 50° , in Q^2 range of 0.0003 to 0.008 (GeV/c)². There will be PRES experiment at MAMI that measures ep elastic scattering in a Q^2 range of 0.001 to 0.04 (GeV/c)².

5.3 Overview of the MUSE Experiment

The muon is an elementary particle that is similar to electrons but 200 times more massive. As a result of its larger mass, its Bohr radius is 200 times smaller than that of electron. Muon spend more time inside the proton due to wave function overlap, making muonic hydrogen a few million times more sensitive to the size of the proton. The muonic hydrogen spectroscopic observations of proton charge radius also motivated the use of muon beams for scattering experiments. There are currently no data available that would allow the proton radius to be extracted with $\mu - p$ scattering with a precision sufficient to solve the proton radius puzzle.

The goal of the MUSE experiment is to simultaneously measure $\mu^\pm p$ and $e^\pm p$ elastic scattering cross-sections. With simultaneous measurements, $e - p$ and $\mu - p$ elastic scattering can be directly compared at the sub-percent level, allowing much higher level of precision than previously possible at lower Q^2 . Furthermore, by comparing cross sections of positively charged particles versus negatively charged particles, two-photon exchange (TPE) effects can be tested at the sub-percent level, more precisely than previously performed.

Table 5.1

MUSE Kinematics

Quantity	Coverage
Beam momenta	115, 153, 210 MeV/c
Scattering angle range	20° - 100°
Azimuthal coverage	30% of 2π typical
Q^2 range for electrons	0.0016 GeV ² - 0.0820 GeV ²
Q^2 range for muons	0.0016 GeV ² - 0.0799 GeV ²

In MUSE experiment, beam momentas of 115, 153, and 210 MeV/c are used to provide better e and μ fluxes at momenta at which the particles arrive separated in time at the MUSE target. At $Q^2 = 0.0016 - 0.082$ GeV², MUSE is the first experiment to extract and compare proton radius measurements with $e - p$ and $\mu - p$ scattering with reduced systematic uncertainties.

5.4 Experimental Setup

MUSE requires high precision vertices reconstruction and Time of Flight (TOF) determination in order to perform a momentum measurement. Therefore, it has several beam line detectors before the target in order to provide accurate information about the incoming beam. As shown in Figure 5.2 the secondary beam from PiM1 line hits the thin scintillator beam hodoscope which determines particle type using time measurements, then it passes through three triple-layer GEM chambers which can trace particle trajectories and passes through a hole in the annular veto scintillator to filter muons from pion decay. Then it enters the cryo-target vacuum chamber and strikes the target ladder and exits the vacuum chamber and goes through the beam monitor .

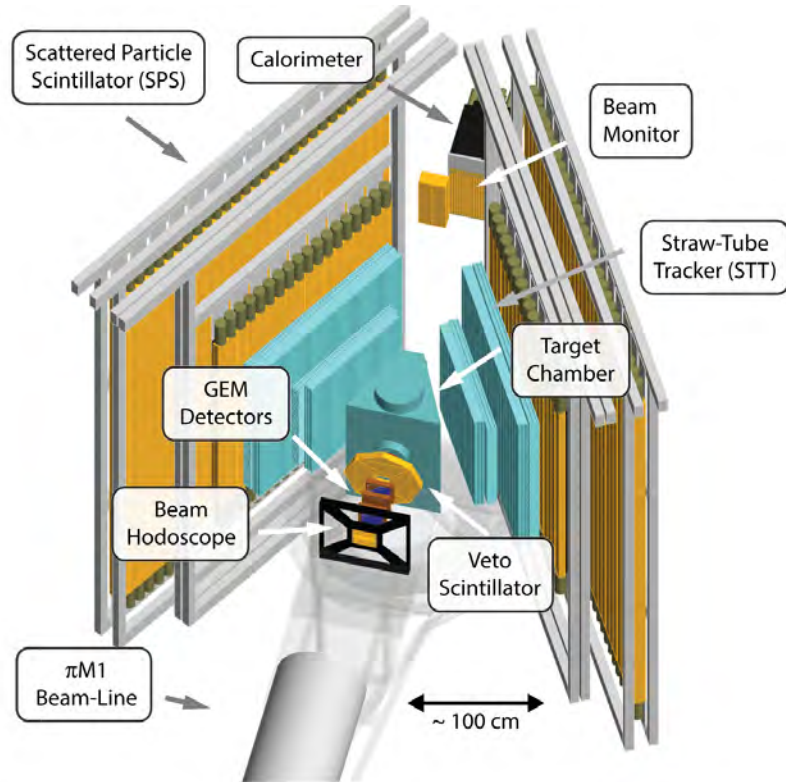


Figure 5.2. MUSE Apparatus implemented by MUSE Geant4 simulation - Image courtesy: Steffen Strauch.

5.4.1 PiM1 Beam Line

At PSI, MUSE utilizes a secondary beamline provided by the High-Intensity Proton Accelerator (HIPA). Previously, the PiM1 channel has been primarily used for high precision pion scattering experiments and to investigate π beam properties. Recently it has been studied the properties of muon and electron beams as well [33].

The PiM1 channel generates a combination of secondary beams consisting of electrons, muons, pions, and high-momentum protons, all of which are generated through the interaction of the primary proton beam with the M1 production target. A diagram of the beamline elements can be found in Figure 5.3. The production of these secondary beams occurs at a 22° angle with respect to the proton beam at target-M. The channel consists of focusing quadrupoles (red), two horizontal bending dipoles

(blue) with a 75° deflection angle, and two sets of jaws (green) for controlling beam flux. The beam line has a 65 msR solid angle nominal acceptance, resulting in a 2.9 momentum acceptance, and is approximately 23.5 m in length. In the beam line, electrons, muons, and pions are generated through multiple mechanisms.

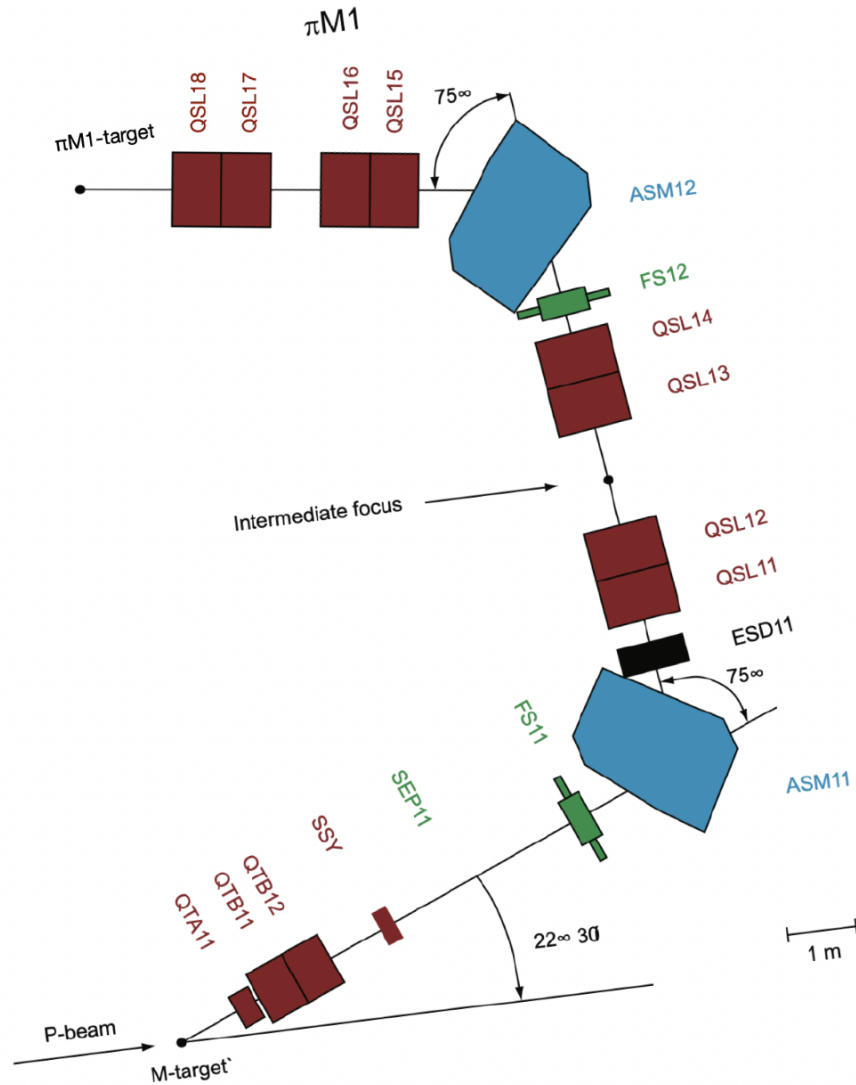


Figure 5.3. Main components of PiM1 beamline [1].

Pions are primarily generated through direct strong interactions within the target wheel through,

$$pC \rightarrow \pi X \quad (5.4.1)$$

where X refers to the final state of the reaction, which may include excited nucleon or nuclear states as well as states in which the carbon nucleus has been fragmented into smaller nuclei.

Electrons are produced through two distinct mechanisms involving pion decay. The first, which has the largest branching ratio (98.8%), occurs when neutral pions decay into intermediate states, which subsequently decay into electron-positron pairs in the target carbon.

$$\pi^0 \rightarrow \gamma\gamma \quad (5.4.2)$$

$$\gamma \rightarrow \gamma C \rightarrow e^+e^-X \quad (5.4.3)$$

The second source of electrons is from a process called the Dalitz decay, which has a branching ratio of 1.2%. In this process, neutral pions decay into electron-positron pairs and a photon.

$$\pi^0 \rightarrow e^+e^-\gamma \quad (5.4.4)$$

The muons are produced from charged pion decays. This decay process is not localized to a point source, as the charged pion can decay at any point along its trajectory. The decay is governed by the weak interaction, which leads to a longer half-life for charged pions.

$$\pi^\pm \rightarrow \mu^\pm + \nu_\mu(\bar{\nu}\mu) \quad (5.4.5)$$

or

$$\pi^\pm \rightarrow e^\pm + \nu_e(\bar{\nu}e) + \nu_\mu(\bar{\nu}\mu) \quad (5.4.6)$$

To achieve distinct separation between electrons, muons, and pions within a 20 ns Radio Frequency (RF) interval, the MUSE experiment employs beam momenta of

approximately 115, 153, and 210 MeV/c, with both positive and negative polarity. As shown in Figure 5.4, for the momenta 117.5 MeV/c and 160 MeV/c, the peaks from left to right correspond to e , π , μ and for 210 MeV/c, the peaks correspond to e , μ , π . By utilizing these specific beam momenta, the experiment is able to distinguish between the different particles based on their momentum and time-of-flight within the RF interval of 20 ns.

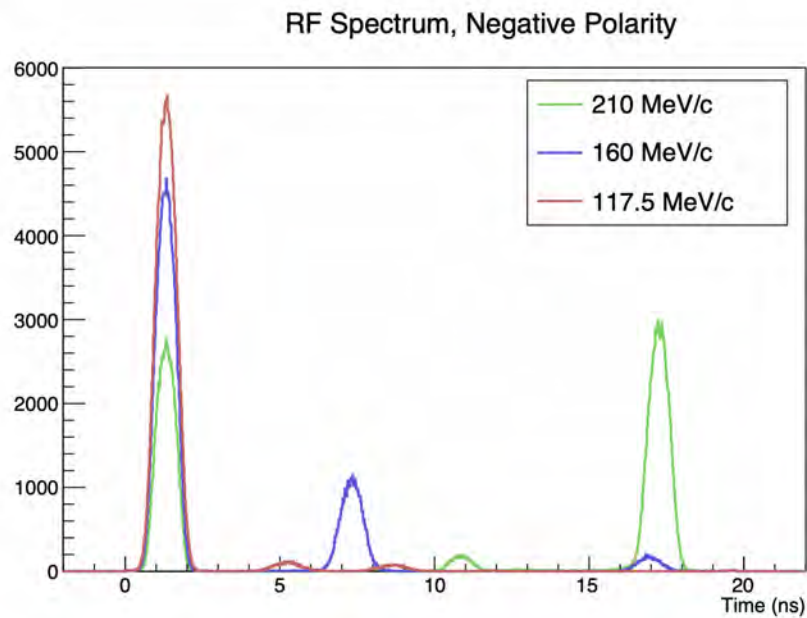


Figure 5.4. Measured RF time spectrum for negative charge beams with momenta of 117.5 MeV/c, 160 MeV/c, and 210 MeV/c, at a distance of ≈ 23.5 m from the production target [1].

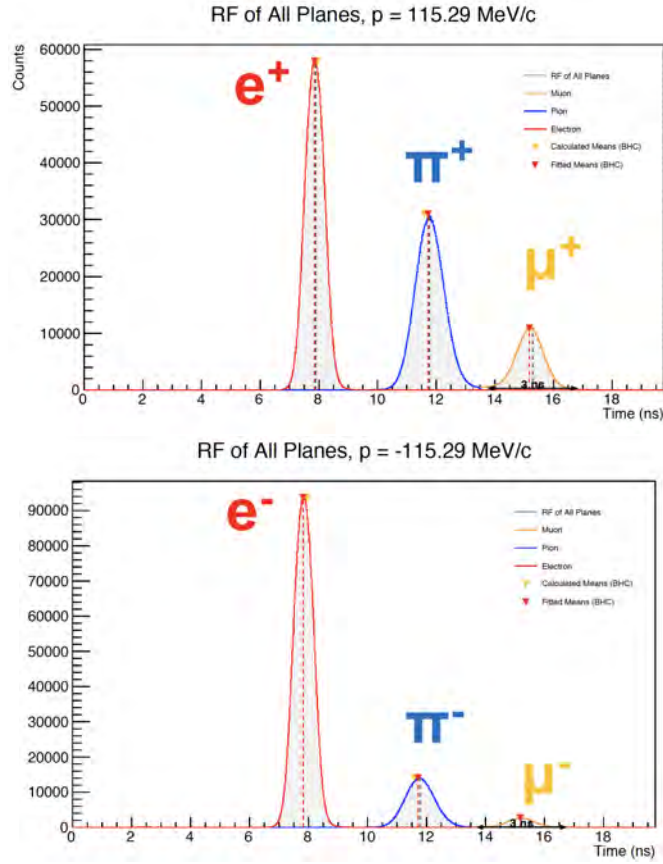


Figure 5.5. Measured RF time spectrum for positive (top) and negative (bottom) charge beams with momenta of 115.29 MeV/c.

The MUSE timing detectors are utilized for time-of-flight (TOF) measurements to identify mixed beam particles (e, μ, π) based on their distinct masses [34]. To accommodate the low beam flux of ≈ 3.3 MHz and cover a horizontal angular range of 20° to 100° , the experiment necessitates large angle detectors for scattered particles and tracking detectors to determine the scattering angle. The following discussion covers details about each detector used in the experiment.

5.4.2 Beamline Detectors

5.4.2.1 Beam Hodoscope

The beam hodoscope is located at the upstream end of the beamline, serving as the first detector. It can provide precise timing information as well as position information for beam particles. In addition, the beam hodoscope can also determine the total incident beam flux. The timing information from the beam hodoscope will be combined with the RF signal to accurately identify beam particles, enabling high precision event analysis. By measuring the time of flight from the beam hodoscope to the scattered particle scintillators, it is possible to distinguish between different reaction types, such as muon decay and muon scattering. Additionally, comparing the time of flight from the beam hodoscope to the beam monitor's RF time allows for accurate particle identification, background identification, and determination of the μ and π beam momenta.

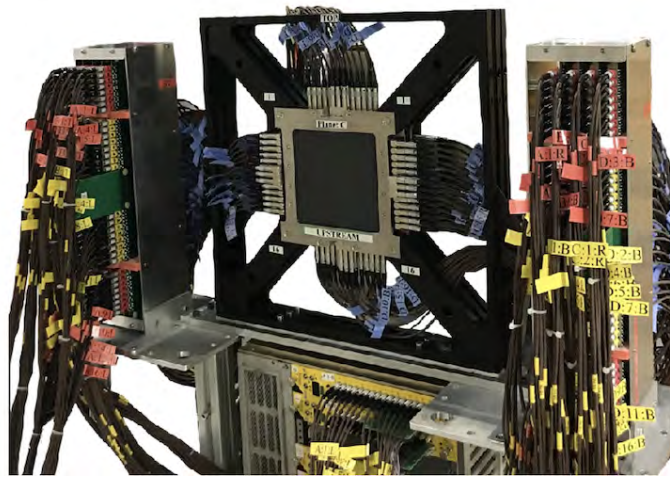


Figure 5.6. Beam hodoscope - Plane C.

The beam hodoscope (BH) is constructed with double-ended BC-404 scintillator paddles glued to Hamamatsu S13360-3075PE SiPMs which are mounted on custom printed circuit boards (PCBs). As shown in Figure 5.6 each plane consists of 16

paddles, with 6 central paddles measuring 10 cm in length, 4 mm in width, and 2 mm in thickness, and 5 outer paddles on each side measuring 10 cm in length, 8 mm in width, and 2 mm in thickness. As a result, each plane contains 32 readout channels. Light generated by the BC-404 plastic paddles is collected by SiPMs. To create an air gap that enables total internal reflection of scintillation light within the bar, aluminum foil is utilized to position each bar 6 μm apart. The bars alternate in orientation: the first plane is oriented in the y direction, the second plane in the x direction, the third plane in the y direction, and the fourth plane in the x direction. Additionally, each plane is offset by 0.5 mm from the previous plane to minimize the impact of geometric inefficiencies from particles that pass between bars without being detected. A total of 4 planes are built by Rutgers University and Tel Aviv University. It is configured to use all 4 planes at the highest beam momentum of 210 MeV/ c and the number of installed planes will be reduced to 3 at 153 MeV/ c and 2 at 115 MeV/ c due to the lower timing precision required at lower beam momenta.

5.4.2.2 GEM Detector

The Gas Electron Multiplier (GEM) is a high-resolution tracking detector that follows the BH detector. Tracking detectors with high spatial resolution are required in MUSE to precisely measure the particle trajectories as they enter the target, allowing for the accurate reconstruction of the scattering kinematics. A resolution of 50 – 100 μm can be achieved using GEM detectors. It has been shown that GEMs can endure harsh radiation conditions (rate capability upto 5 MHz beam flux), retain high resolution and efficiency for individual events, and exhibit negligible aging effects. Due to their low-mass design, GEM detectors effectively minimize multiple scattering. The main characteristics of the GEM detector can be seen in Table 5.2.

The GEM detector consists of 3 triple-layer GEM chambers. By measuring hit positions, a GEM detector can determine particle trajectories into the target and re-

construct scattering kinematics on an event-by-event basis. Figure 5.7 displays three 10 cm x 10 cm GEM planes equipped with electronic readouts. These detectors were designed, constructed, developed and effectively operated by the group from Hampton University at OLYMPUS experiment at DESY [35]. In OLYMPUS, the GEM components were labeled as upstream (US), middle (MI), and downstream (DS), and the same terminology will be applied for MUSE. An additional GEM element was added and it is labelled as Fourth (4TH). The utilization of three or four GEM elements for tracking purposes in MUSE has been a topic of debate. This matter will be comprehensively examined in Section 6.8.

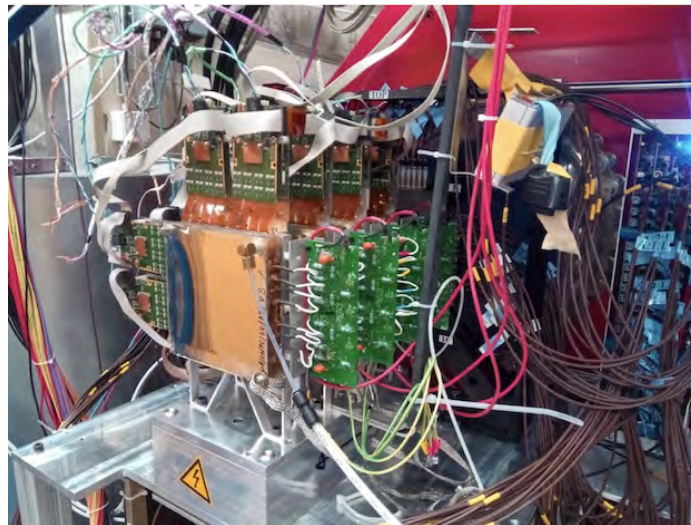


Figure 5.7. 10 cm x 10 cm triple-layer GEM detectors built by Hampton University.

The 3 GEM chambers are operated using a gas mixture of 70% argon and 30% carbon dioxide. Two-dimensional strip readouts with a pitch of $400\ \mu\text{m}$ are employed. The GEM detectors are equipped with FPGA-controlled frontend electronics that use the APV-25 chip, originally designed for CMS, for readout. The signals are subsequently digitized using the Multi-Purpose Digitizer (MPD). With each APV processing 128 readout channels, analog and digital information from 128 channels are conveyed through a single cable. Raw signals from all strips are sampled at a

frequency of either 20 or 40 MHz. Following latency adjustments, "snapshots" of the analog signal are captured and transmitted as frames to the VME-based controller. The MPD controller furnishes clock, trigger, and configuration commands to the APV via I2C interface, and captures the raw data by digitizing it into onboard ADCs. Further details on the data processing of GEM detectors will be provided in Section 4.5.

For the nominal PiM1 beam at the last GEM located just upstream of the target, the anticipated rate density is approximately $3.3 \text{ MHz}/5 \text{ cm}^2$, which equals $0.66 \text{ MHz}/\text{cm}^2$, with a probability of detecting a single track exceeding 90%. Due to the beam's focal point, the rate density for the upstream GEMs will be comparatively lower. During the summer 2018 beam time, two supplementary GEM planes were implemented at the IFP. These planes were not included in the MUSE production data configuration and exhibited sub-optimal performance. Their purpose was to evaluate beam distributions at the IFP. Upon close examination of the top two panels of the Figure 5.8, it is observable that the GEM distribution is broader for the upstream GEM compared to the middle GEM [18]. In PiM1, the beam focal point is situated after the GEM detectors at the scattering target. As a result, the beam's increased width in the upstream GEM is in line with expectations, as it subsequently converges at a later point.

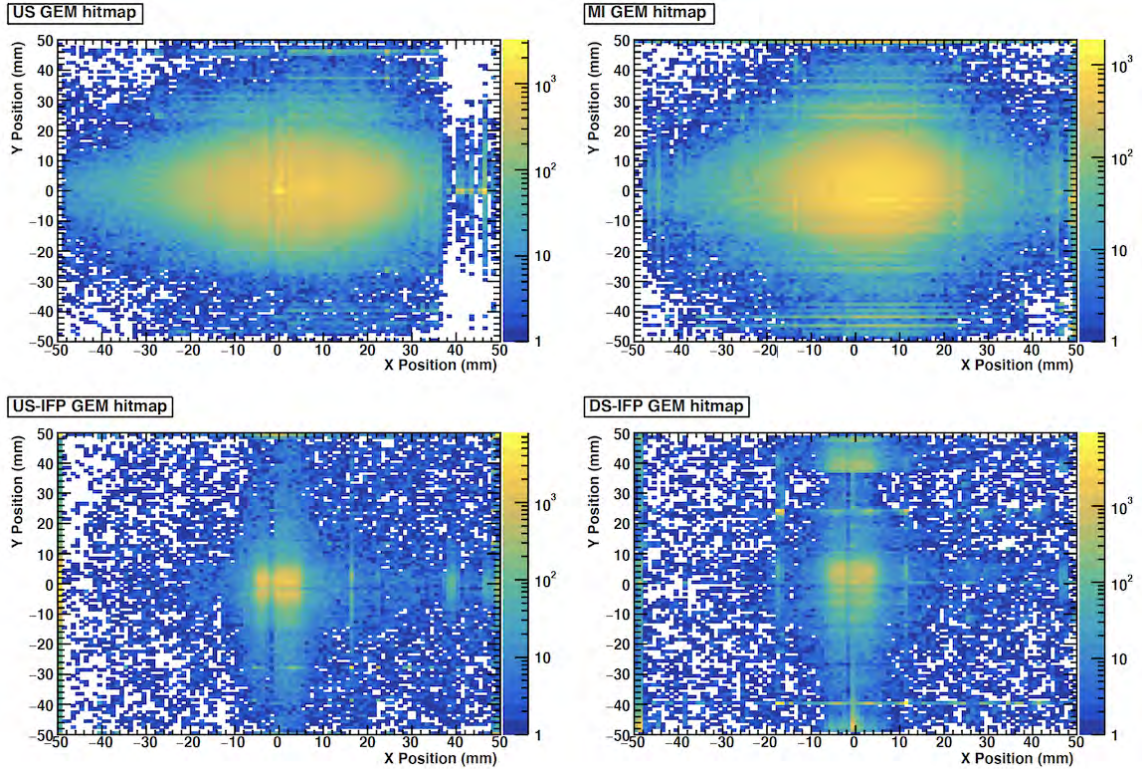


Figure 5.8. GEM hit maps of the beam [18].

5.4.2.3 Veto Scintillator

The primary purpose of the beam veto detector is to decrease the trigger rate by rejecting any scattering or decay events involving beam particles that occur upstream of the scattering chamber. Vetoing can be used to prevent certain events or particles from being included in data analysis in order to reduce background noise or increase the signal-to-noise ratio. A number of these decays such as $\pi^\pm \rightarrow \mu^\pm \nu_\mu$ or $\mu^\pm \rightarrow e^\pm \nu_\mu \nu_e$, occur at an angle that may be misconstrued as a track in the scattered particle detectors. To prevent these events from being recorded to the data storage system, the veto is strategically positioned to identify any decay events that occur upstream of the veto detector.

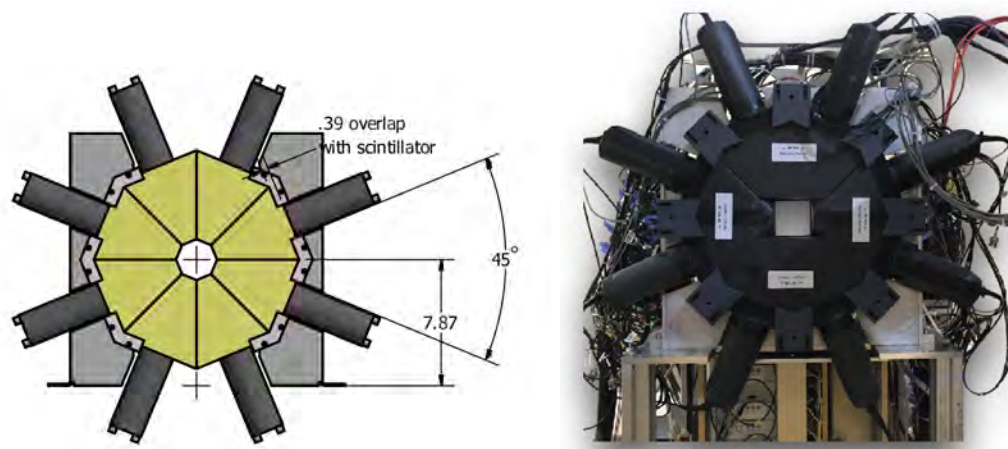


Figure 5.9. Schematic of beam veto detector (Left) and installed veto detector at PSI looking upstream (Right).

The veto detector was constructed by the group at South Carolina. As shown in Figure 5.9, it is designed in an approximately annular shape that encircles the beam and comprised of eight trapezoidal scintillators that are read out using Hamamatsu R13435 PMTs. The detector's inner radius measures 3 cm, which aligns with the thin entrance window of the target vacuum chamber.

5.4.2.4 Beam Monitor

The beam monitor is positioned downstream of the target and it ensures beam stability by monitoring the relative position and current of the beam. Additionally, it is used for taking time-of-flight data in conjunction with the BH detector and aids in the reduction of background noise. One such source of background is Møller or Bhabha scattering, which results in a high-energy electron or positron moving forward, along with a low-energy scattered particle that may trigger the detector system. The BM detects forward-moving particles, which can help in suppressing this background noise.



Figure 5.10. Beam monitor at PSI in production data configuration setup.

The BM detector is composed of two components: central hodoscope and an outer hodoscope to increase the beam's angular acceptance. The central hodoscope of the beam monitor is made up of two planes, each plane consisting of 16 paddles attached to SiPMs. Similar to the beam hodoscope, each paddle measures 300mm in length, 12mm in width, and 3mm in thickness, and is made of BC-404 material. The outer hodoscope consists of 4 large bars and constructed using EJ-204 scintillators that are 30 cm long, 6 cm wide, and 6 cm thick. The large scintillator bars were constructed by South Carolina while the thin scintillator paddles were fabricated by Rutgers and Tel Aviv University. The thick scintillators have a time resolution of approximately 35 ps, and the thin paddles have a time resolution close to 100 ps [34].

5.4.3 Target

The MUSE target system is comprised of multiple components, including a target ladder with various targets, a cryocooler and copper condenser assembly to liquefy the hydrogen gas, a vacuum chamber to house the target ladder and condenser, a lifting

system, a gas handling and vacuum system, and a slow control system to regulate hydrogen flow. The LH₂ scattering chamber was designed and built collaboratively by the University of Michigan and a private company called CREARE [36]. As shown in Figure 5.11, the target ladder is situated within a vacuum chamber, featuring large, thin exit windows to enable scattered particles to pass through and reach the scattered particle detectors. It has four targets, the LH₂-filled upper cell operates as the cryogenic target, maintained at 20 K and 1 bar pressure, while the lower cell, which is empty, serves as the dummy target. The carbon target is employed for detector alignment purposes.

Segments and their features of the target ladder for the MUSE experiment;

1. LH₂ target cell - for scattering.
2. Identical target cell without LH₂ - for background studies.
3. 1 mm thick segmented carbon and CH₂ target with a gap - for calibration, detector alignment and tracking studies.
4. Empty space - for TOF and dispersion measurements.

To achieve the required cooling, a cryocooler is used to cool both the copper condenser and the copper structure of the target ladder. Both the target ladder and the condenser are placed inside a vacuum chamber to ensure proper thermal insulation. The vacuum chamber is designed with two windows. The beam entrance and exit windows are made of Kapton with a thickness of 0.125 mm. The scattering windows are made of laminated Mylar and are 337 mm wide and 356 mm high. They cover a θ range of $[20^\circ, 100^\circ]$ on each side of the beamline and a ϕ range of $[-45^\circ, 45^\circ]$ from the target center at $\theta=60^\circ$, allowing for the passage of the beam and scattered particles. .

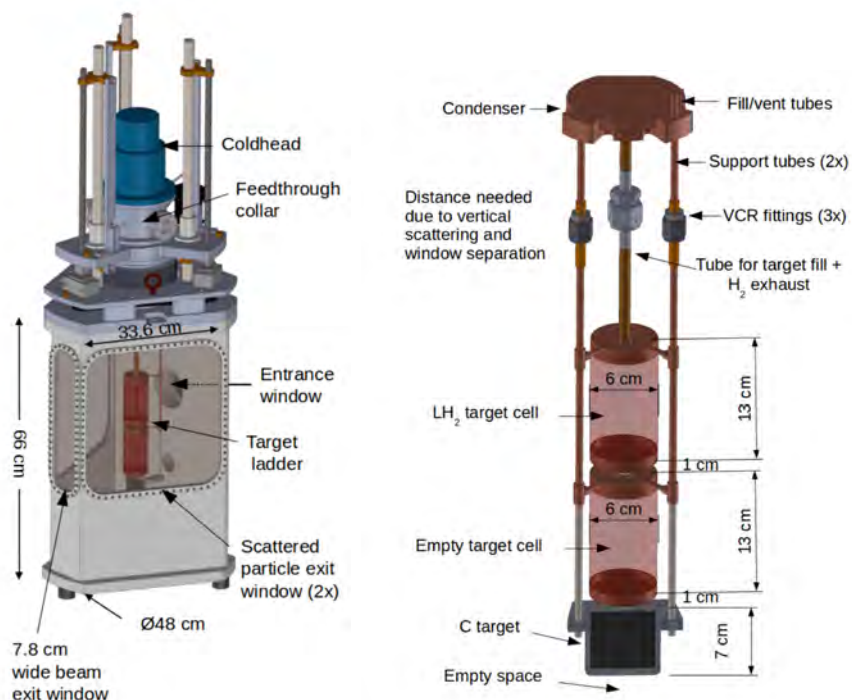


Figure 5.11. Schematic of scattering chamber (Left) and target ladder (Right).

5.4.4 Scattered Particle Spectrometer

5.4.4.1 Straw Tube Trackers

The Straw Tube Tracker is designed to provide accurate and efficient tracking of scattered particles originating from the target. The design is based on PANDA collaboration and developed by the group from Hebrew University [37]. The single-ended drift chambers that are sensitive to the position of particles and measure their trajectories with minimal induced multiple scattering. To ensure high tracking efficiency, MUSE requires the detectors to be symmetrically positioned on both sides of the beamline as shown in Figure 5.12. This is achieved by using 2 chambers, each with 5 vertical and 5 horizontal planes. To improve the resolution of the scattering angle, the vertical straw planes are positioned closer to the target. The STT has a resolution capable of tracking particles with a precision of $150 \mu\text{m}$. The STTs are centered at $\theta = 60^\circ$ and cover an angular range from 20° to 100° in θ and $\pm 45^\circ$ in ϕ .

This provides an angular coverage of approximately 30% of the typical 2π azimuthal range [1].

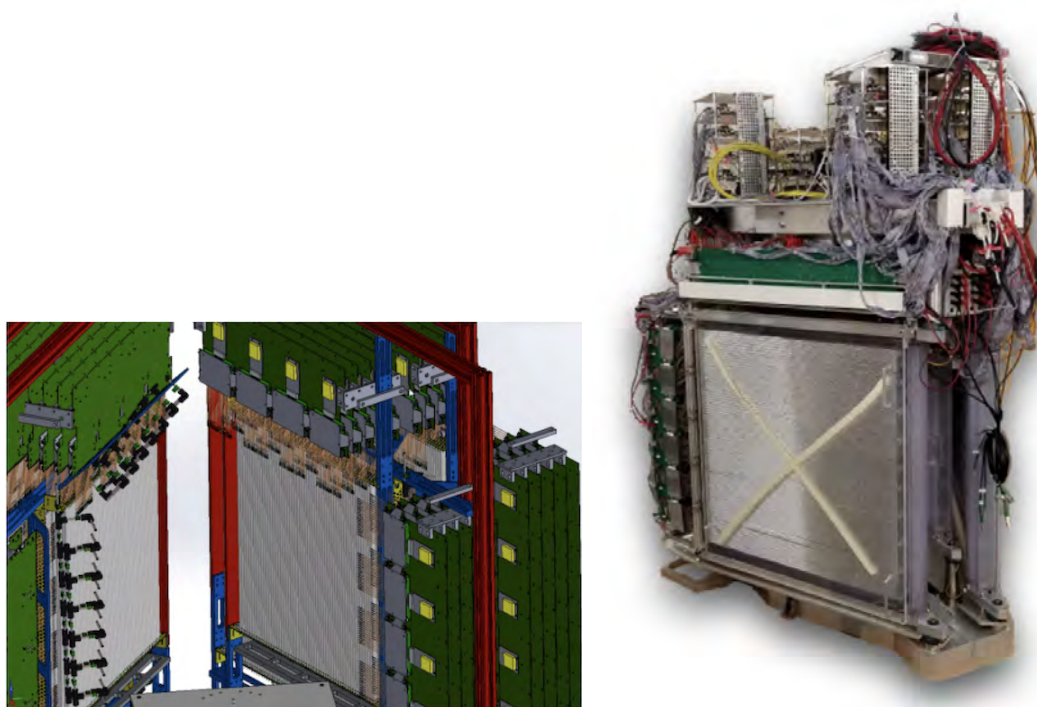


Figure 5.12. CAD drawing of the four STT chambers mounted on a table. The straws are depicted in light gray color, while the HV/readout cards are in dark gray (Left) and installed STT chamber at PSI (Right) [1].

In the front chambers, there are a total of 575 straws - 275 vertical straws with a length of 60 cm and 300 horizontal straws with a length of 55 cm. Meanwhile, the rear chambers contain a total of 850 straws - 400 vertical straws with a length of 90 cm and 450 horizontal straws with a length of 80 cm. The entire system has a total of 2850 straws. An independent gas supply system will be provided for each of the four chambers, and they will be operated using a gas mixture consisting of 90% Ar and 10% CO₂.

5.4.4.2 Scattered Particle Scintillators

The Scattered Particle Scintillators are located behind the STT on each side of the chamber. They play a crucial role in the event trigger and aid in particle separation by measuring time-of-flight (TOF). The detector is capable of time resolution at the level of 50-70 ps, which may vary depending on the type of particle and its momentum. On each side of the detector, there are two walls of scintillators. The front walls are made up of 18 short scintillator bars, each with dimensions of 6 cm \times 3 cm \times 120 cm while the rear wall, comprises 28 long scintillators, with dimensions of 6 cm \times 6 cm \times 220 cm. The front wall covers a horizontal angular range from 20° to 100° from the target, and azimuth angles from -45° to 45° from the target center at 60°. The back wall, on the other hand, has a larger angular acceptance to accommodate particles that scatter in the front wall material. To minimize noise hits, it is necessary to have a hit in both the front and back walls of the SPS for triggering purposes.

The Scattered-Particle Scintillators were constructed by the Experimental Nuclear Physics Group at University of South Carolina. Each counter in the Scattered-Particle Scintillators is composed of a plastic scintillator bar (Eljen EJ-204) with PMTs (Hamamatsu R13435) attached on both ends. The bar is then wrapped with aluminized mylar foil, followed by DuPont™Tedlar film that extends beyond each PMT to provide a light-tight casing for the entire counter. Pairs of scintillator bars are mounted on a backing structure, which for the front wall consists of a ROHACELL board sandwiched between two carbon-fiber sheets, while the rear wall has aluminum sheets. These units are then mounted in a frame at PSI as shown in Figure 5.13



Figure 5.13. Scattered Particle Scintillator.

A comprehensive summary of all the detector requirements for the MUSE experiment can be found in Table 5.2. This table provides a consolidated overview of the specific requirements and specifications for each detector used in the experiment.

Table 5.2

Detector Requirements for MUSE [1]

Detector	Resolution	Efficiency	Rate Capability	Readout Speed
Beam hodoscope	100 ps / plane	99%	3.3 MHz / plane	–
GEM Detector	100 μm / element	98%	3.3 MHz / plane	2 kHz
Beam Veto	1 ns / plane	99%	1 MHz / plane	–
STT	150 μm	99.8%	0.5 MHz	–
SPS	≈ 60 ps / plane	99%	0.5 MHz / paddle	–

CHAPTER 6

GEM DATA ANALYSIS FOR MUSE EXPERIMENT

6.1 Introduction

The presence of background hits in the data can significantly impact the accuracy and precision of the analysis. Thus, it is essential to develop robust algorithms and techniques that can effectively identify and filter out these background hits from the data.

Accurate identification of cluster positions, efficient reconstruction and good resolution of the primary track are crucial requirements for the successful analysis of the GEM detectors. Having an efficient method to extract the actual cluster positions of GEM detectors from false cluster positions is the primary prerequisite. This is a crucial step as it provides the foundation for all subsequent analysis. Secondly, the primary track must be accurately identified from a multitude of false tracks that arise due to the presence of background hits. This is a significant challenge and requires advanced algorithms and techniques to distinguish between real and fake tracks. Finally, it is essential that the reconstructed primary track has good resolution, in order to extract precise information about detector efficiency. A high-resolution track ensures that the measured quantities are free from systematic errors and are consistent with the theoretical predictions. A higher efficiency means that the detector can accurately detect more particles, resulting in better statistics and higher precision measurements.

In this chapter, we will explore various approaches to address this challenge, including the use of different algorithms, statistical methods, and data analysis techniques to extract efficiencies of GEM detector planes in high and low beam rate environments of the MUSE experimental setup.

Additionally, we need to determine whether three or four GEMs would be more suitable for the experimental setup. To compare the efficiency of three versus four GEM elements, we can conduct a systematic study that involves varying the number of GEMs in the setup and measuring their efficiency in both high and low beam rates. We can then compare the results and determine which configuration provides the highest efficiency and redundancy.

6.2 Analysis

The analysis of GEM-related data typically involves four main steps. The first step is the decoding of the raw data, which involves converting the digital signals from the detector electronics into a format that can be easily analyzed. This step typically includes data cleaning and calibration, which corrects for detector imperfections and noise. The second step is GEM hit reconstruction, which involves identifying the locations of the charged particles that pass through the GEM detectors. This step is essential as it provides the input for the subsequent track reconstruction. The third step is track reconstruction, which involves reconstructing the paths of the charged particles that passed through the GEM detectors. This step typically involves sophisticated algorithms that combine information from multiple detectors to reconstruct the most likely path of the particle. The final step is interaction vertex reconstruction, which involves determining the point at which the charged particles interacted with the target material. This information is critical for understanding the underlying physics process being studied. Overall, the accuracy and precision of each step directly impact the quality of the final results, making each step crucial for obtaining meaningful scientific insights.

In this chapter, our focus will primarily be on the first three steps of the GEM-related data analysis process, namely decoding the raw data, GEM hit reconstruction and track reconstruction to evaluate efficiencies of each GEM plane. The remaining

step - interaction vertex reconstruction - will be carried out using the physics data collected during the Summer and Fall of 2023. The final step require a large amount of data to achieve high accuracy and precision. This will allow us to ensure that the latter stages of the analysis benefit from a more comprehensive data-set, enabling a more accurate and precise reconstruction of particle tracks and interaction vertices.

As of beam time of 2022, there are four GEMs used in MUSE experiment and located just upstream of the target. Since each APV chip processes 128 channels, a 10×10 cm² GEM chamber consists of 2×250 channels that are read out using four APV chips. The GEM analysis code extracts digitized pulses produced by the APV-25 cards from the raw strip data obtained from the detector. The code identifies clusters of strips to determine the location of hit candidates and then fits tracks to these clusters to determine the most probable path of the incoming particle. The spatial information for the track is obtained from the strip numbers and digitized pulse heights of the hit clusters in x and y axes.

6.3 GEM data pre-processing techniques

In this context we refer to the 4 GEM planes as "US", "4TH", "MS" and "DS", with reference to their position in the beam line, starting from upstream and progressing downstream ("US"-Up-Stream, "MS"-Middle-Stream, "DS"-Down-Stream and "4TH"-4th GEM element which was added later). Each GEM plane is equipped with 4 APVs, with two cards mounted horizontally (X) and two vertically (Y). The APVs provide ADC information for each channel, which reflects the magnitude of charge collected in the channel. This ADC information is crucial for reconstructing the position and energy of the detected particles. An example of the ADC spectra for a single GEM plane prior to the implementation of noise subtraction procedures on the data is presented in Figure 6.1, which demonstrates the distribution of the collected charge for each channel for one GEM plane.

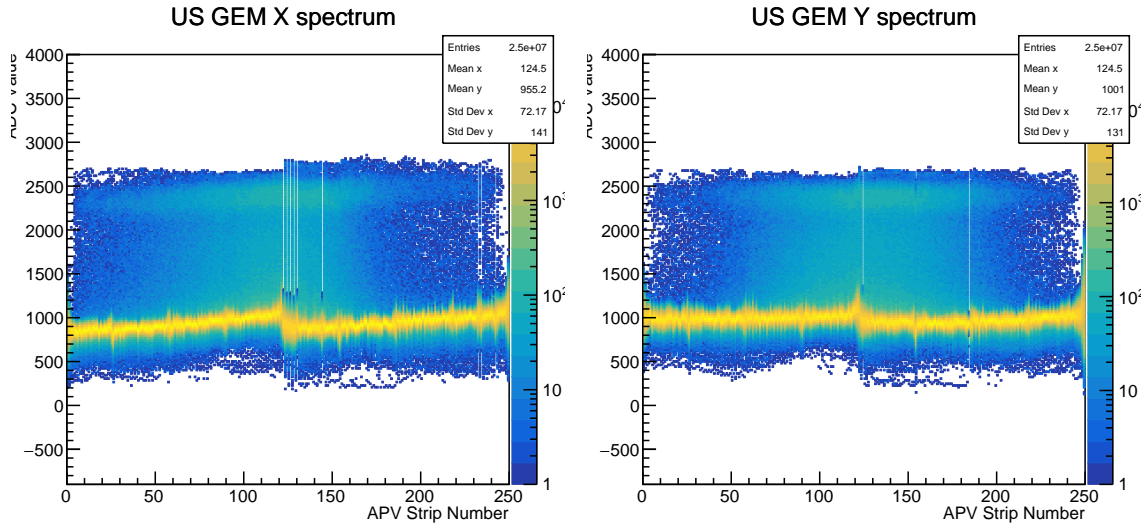


Figure 6.1. ADC spectrum of US GEM plane before implementing noise subtraction routine for x-axis (left) and y-axis (right).

There is a prominent peak near the center of the APV strip numbers for an ADC value of 2000-3000. This occurrence may correspond to the beam traversing through the center of the GEMs and resulting in significant energy deposition near the center. Conversely, a flat background at an ADC value of around 1000 can be observed, which corresponds to the pedestal originating from the digitized value of the voltage baseline. This background is primarily caused by two factors - the common fluctuations of ADC data from event to event (common mode) and the constant offset in individual channels (pedestal).

6.3.1 Common-mode Subtraction

Common mode subtraction is a data pre-processing technique that involves removing common mode noise from the recorded signals. In GEM detectors, the common mode noise arises due to fluctuations in the baseline signal level across multiple channels of the readout electronics, i.e. all channels of an APV. This noise can obscure the signal of interest and reduce the detector's overall sensitivity and resolution. The process of Common Mode Subtraction involves removing the fluctuations in the av-

erage ADC readings of all channels in a given event, which are not part of any cluster and are observed across events for each APV, from the raw data.

The common-mode noise observed in the GEM detector data is attributed to a feature of the APV. This noise observed in the APV chip may be due to the fact that it takes a 25-ns snapshot of the 128 analog signals and sends this as a sequence or "frame" of 128 analog values over the analog cable to the MPD. This cable can have its own noise fluctuations, which could then affect all of the channels of the same frame collectively, resulting in the observed common-mode noise. The process of common mode subtraction is a crucial step in the analysis of GEM data obtained using APV-25 cards. This step is necessary due to the fact that all 128 channels within a single APV-25 card exhibit fluctuations in amplitude that are uniform across all channels and time samples, as depicted in Figure 6.2. These fluctuations cannot be considered electronic noise, as they can be effectively corrected through the measurement of the group shift of all channels event-by-event.

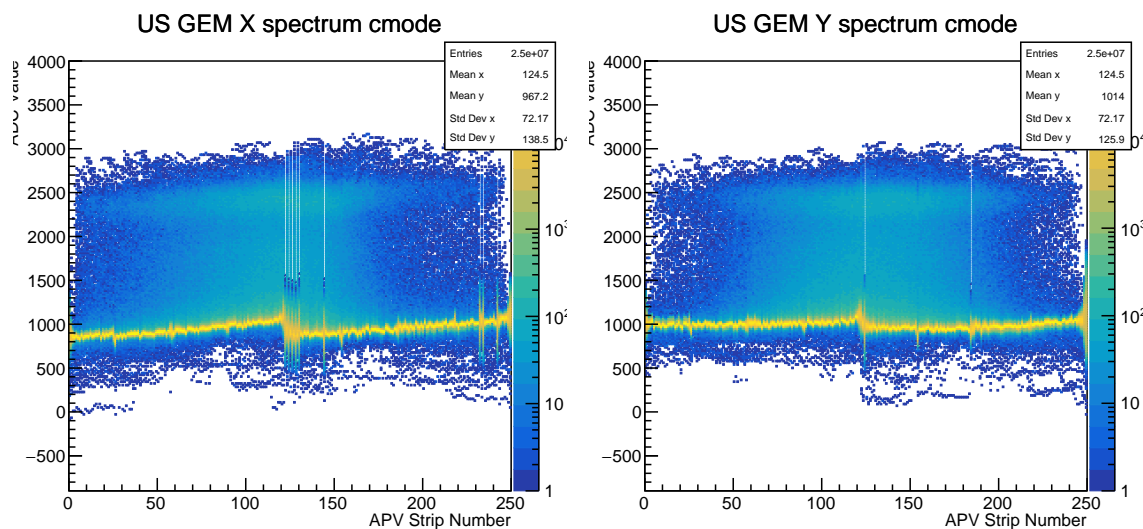


Figure 6.2. ADC spectrum of US GEM plane after subtracting common mode for x-axis (left) and y-axis (right).

To determine the "common-mode" noise, one needs to calculate the CM_{ADC} value per event, averaged over all channels of an APV (up to 128) that did not participate in any cluster. This ensures that only those strips that are supposed to show the pedestal value are taken into account in the averaging. In this process, raw ADC is plotted as a function of APV channel for a single event. To eliminate channels that fired, the APV values are then sorted from high to low, and a suitable cut in ADC value is identified to remove the firing channels. The preferred method orders the list of 128 values and omits the highest and lowest ones before averaging. The remaining channels are used to build the average CM_{ADC} value for each event.

$$CM_{ADC}(i) = \frac{1}{N} \sum_{i=1}^N y_i \quad (6.3.1)$$

where, CM_{ADC} is the Common Mode, N is the total number of channels in a specific event that are not part of any cluster, y_i is the ADC reading of the i -th channel in a specific event that is not part of any cluster.

An average of event-by-event CM_{ADC} values is then obtained for many events, represented by $\langle CM_{ADC} \rangle$. This is one single value per APV card. It is necessary to iterate through the event loop once to obtain event-averages. These event-averages are then applied in the second loop for event-by-event common mode (CM) correction. Then the common mode fluctuation per event is calculated as,

$$CM(i) = CM_{ADC}(i) - \langle CM_{ADC} \rangle \quad (6.3.2)$$

6.3.2 Pedestal Subtraction

Pedestal subtraction is a common pre-processing technique used to remove the baseline signal or "pedestal" level from the recorded signals. The pedestal level is the average signal level observed in a channel when no particles are passing through the

detector. In GEM detectors, the pedestal level can vary between different channels due to variations in the readout electronics or other factors, leading to differences in baseline signal levels across the channels.

Pedestal subtraction involves measuring the pedestal level for each channel by averaging the signal level over a certain number of events in which no particles are passing through the detector. The average value is then subtracted from each individual signal in that channel, effectively centering the baseline around zero. This process allows for a more accurate measurement of the signals of interest, as the pedestal level is no longer contributing to the recorded signal. Pedestal subtraction is typically performed after common mode subtraction and before other signal processing and analysis techniques are applied.

The process involves plotting the raw ADC and common-mode subtracted ADC as a function of the APV channel for multiple events. For each APV channel, the raw ADC and common-mode subtracted ADC spectrum (1D-histogram) are plotted for multiple events. The plot is then updated by suppressing channels that fired. The peak of the pedestal is identified as the location of the maximum value in the histogram, not the mean value. This value is denoted as $PED(j)$, where j is the APV channel number, and there are 128 such channels.

The Gaussian sigma of the pedestal peak is identified to determine the noise level of the channel. If the peak is Gaussian with mean at 0, then $\sigma = RMS$ value, otherwise $RMS > \sigma$. The formula for the pedestal value of APV channel j can be expressed as:

$$PED(j) = \operatorname{argmax}_x h_j(x) \quad (6.3.3)$$

This represents the pedestal value for APV channel j as the argument x that maximizes the histogram $h_j(x)$ of the raw ADC and common-mode subtracted ADC values over many events.

Figure 6.3 displays the histogram of the ADC distribution following pedestal subtraction. Notably, the yellow band, which was initially centered around ADC values of 800-1000, has now shifted towards 0. This shift can be attributed to baseline correction. However, the baseline is still broadened by the common mode fluctuations not yet corrected for.

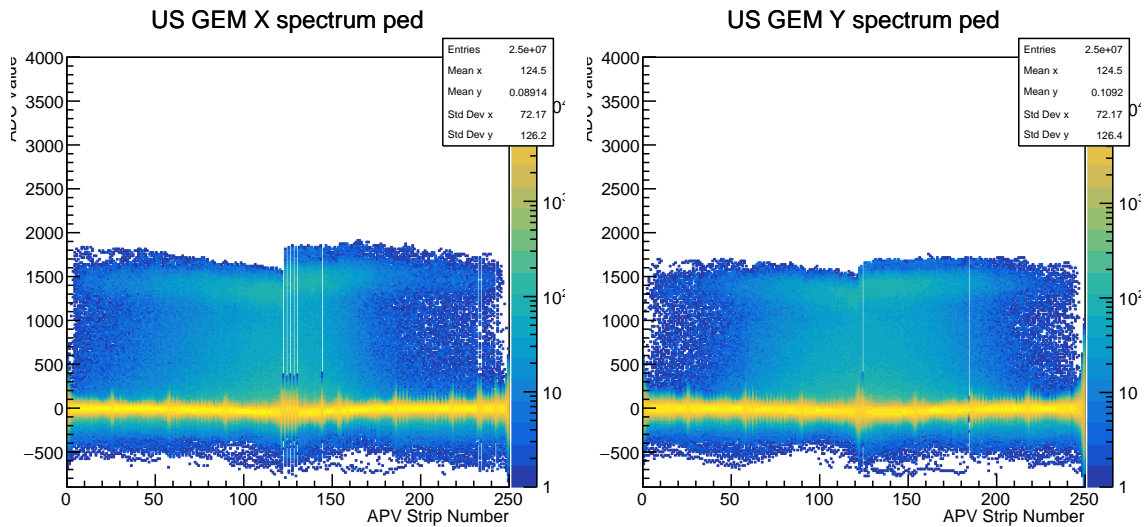


Figure 6.3. ADC spectrum of US GEM plane after pedestal subtraction for x-axis (left) and y-axis (right).

6.3.3 Background Corrected Data

In summary, to obtain corrected ADC readings for an event i on an APV channel j the following steps are performed: The raw ADC value is denoted as $raw_{ADC}(i, j)$.

- The common-mode corrected ADC value before pedestal subtraction is calculated as,

$$cm_{ADC}(i, j) = raw_{ADC}(i, j) - CM(i) \quad (6.3.4)$$

where $CM(i)$ is the common-mode noise value for event i .

- The pedestal-subtracted ADC value before common-mode correction is denoted as,

$$ped_{ADC}(i, j) = raw_{ADC}(i, j) - PED(j) \quad (6.3.5)$$

where $PED(j)$ is the pedestal value for each event j .

- Finally, the common-mode corrected and pedestal-subtracted ADC value is denoted as,

$$ADC(i, j) = raw_{ADC}(i, j) - CM(i) - PED(j) \quad (6.3.6)$$

Figure 6.4 illustrates the common-mode and pedestal subtracted ADC spectrum for the X-axis and Y-axis of the US GEM plane. It is evident that the yellow band has become narrower and is now centered around zero. This confirms the successful application of appropriate pre-processing techniques.

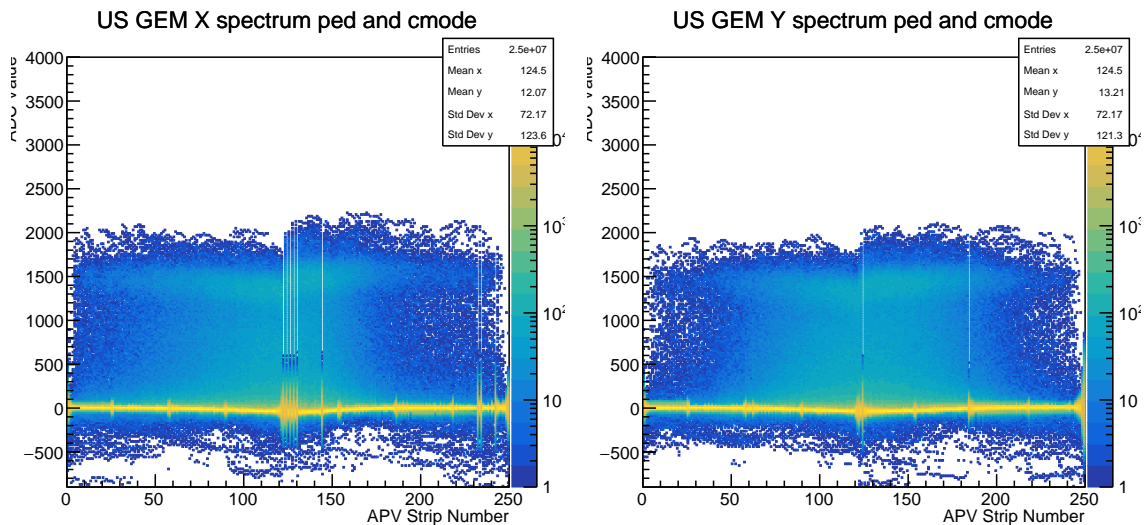


Figure 6.4. ADC spectrum of US GEM plane after subtracting common-mode noise and pedestal for x-axis (left) and y-axis (right).

It's important to note that both the common-mode noise value $CM(i)$ and the pedestal value $PED(j)$ require an average over many events to obtain good accuracy. Processing at least 10,000 events, and ideally 30,000-50,000 events, is recommended to achieve stable averages.

Furthermore, it's essential to perform common-mode correction and pedestal determination on a run-by-run basis since these values can drift over time. The COOKER

can perform two loops over the run. The first loop is used to obtain the channel-averages and event-averages that are needed to calculate the common-mode noise value $CM(i)$ and the pedestal value $PED(j)$. These values are then used in the second loop to perform the common-mode correction and pedestal determination for each event and channel.

This approach also ensures that the common-mode noise value and pedestal value are accurate and stable before being applied to the data in the second loop.

6.4 Channel masking

Channel masking is a technique used in GEM detectors to exclude certain channels from the data analysis process. Channel masking is typically used to exclude channels that are not functioning properly ("dead") or that are producing spurious signals ("hot") due to noise or other sources of interference. It is an important technique for ensuring the accuracy and reliability of GEM detector data. By excluding channels that are producing problematic, uninformative or unreliable signals, selective channel masking allows for more accurate analysis and interpretation of the remaining data.

Channel masking involves identifying the channels that need to be excluded and marking them as "masked" channels. We should first identify the hot/dead channels by analyzing the data and looking for channels with anomalously high or low signals. To identify these problematic channels in analysis code, the number of times each strip registers a signal is recorded, and a distribution of these frequencies is generated as shown in Figure 6.5. This distribution provides activity levels of individual channels. By studying the distribution, it's possible to identify hot channels, which exhibit an unusually high firing rate, or dead channels, which show little to no activity.

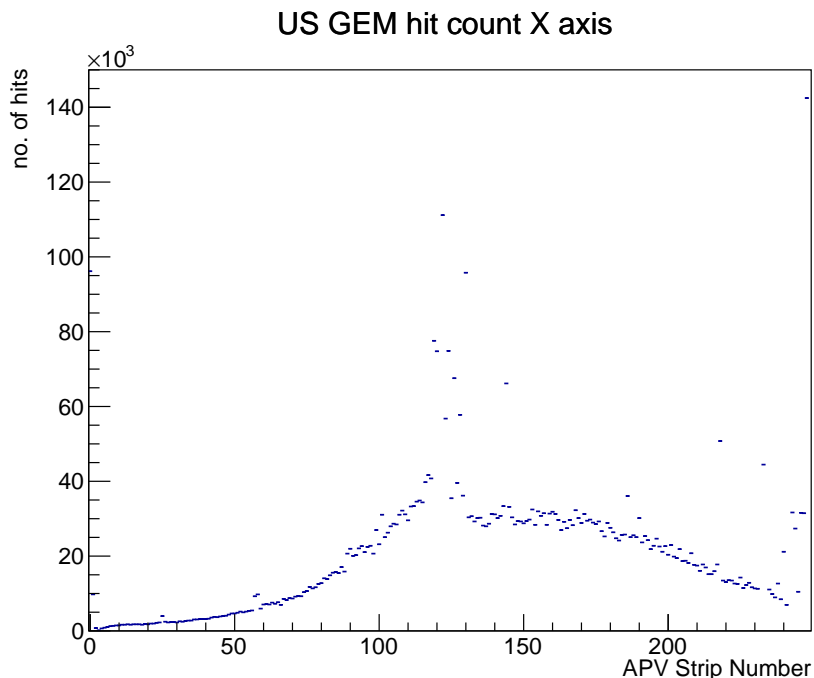


Figure 6.5. Distribution of hit counts for each strip along the X-axis of the US GEM detector.

To mask or exclude certain channels from the analysis, we can manually create an XML file and enter the channel numbers that need to be masked. For example, the first line will mask the channel 122 on X axis of GEM 0, i.e. US GEM similarly, the fifth line will mask the channel 133 on Y axis of 4TH GEM.

```
<deadchannels id="0">0,122,X,122</deadchannels>
<deadchannels id="1">0,124,X,124</deadchannels>
<deadchannels id="9">0,124,Y,124</deadchannels>
<deadchannels id="10">0,184,Y,184</deadchannels>
<deadchannels id="11">1,133,Y,133</deadchannels>
<deadchannels id="12">2,58,X,58</deadchannels>
```

The XML file can then be used by COOKER to skip the masked channels during data processing. Once a channel is masked, its data is excluded from further

analysis, allowing the remaining channels to be analyzed without the influence of the problematic channel.

Figure 6.6 depicts common-mode and pedestal subtracted ADC spectrum on the left side, while on the right side, the hot channels are flagged using the XML file in the same spectrum.

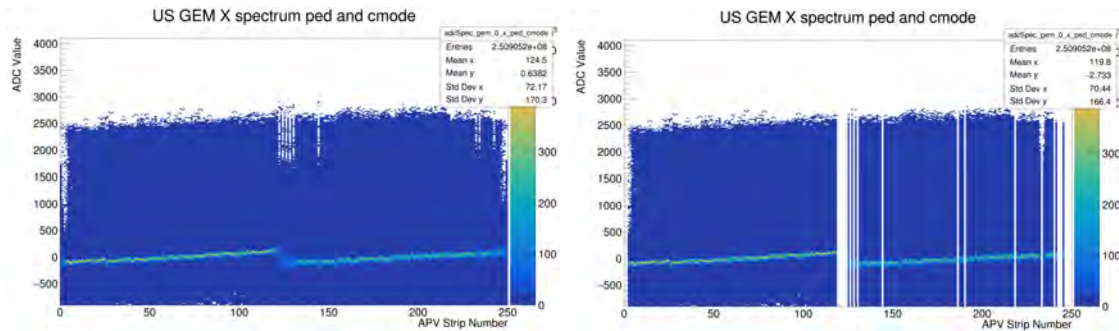


Figure 6.6. Common-mode and pedestal subtracted ADC distribution of X-axis of US GEM (left) Vs. flagged hot channels in the same ADC distribution (right).

6.5 Cross-talk Suppression

Cross-talk is an unwanted effect that can occur in GEM detectors, where a signal on one channel of a readout system induces a signal on another channel. Cross-talk can occur due to various reasons such as capacitive coupling between adjacent channels, or reflections from the readout electronics. Cross-talk can lead to false signals, signal distortion, and reduced signal-to-noise ratio, which can negatively impact the performance of the detector. Cross-talk suppression is an important technique for improving the performance of GEM detectors, especially in MUSE experiment where high precision and low noise are required.

Cross-talk can make strips appear noisier and create fake clusters. When cross-talk occurs between neighboring strips, the induced signals can add to the noise of the original signal. This additional noise can make it more difficult to distinguish

the real signal from the noise and can increase the uncertainty in the measurement. Moreover, cross-talk can create fake clusters, which are clusters of signals that do not correspond to real charge deposition events in the detector. These fake clusters can be mistaken for real clusters, leading to incorrect measurements of the position and energy.

6.5.1 Identification

A higher signal on ch_i can induce signals on $ch_{i\pm 1}$ and $ch_{i\pm 2}$ on the APV. This suggests that there is some form of crosstalk between these channels. One possible mechanism for this crosstalk could be capacitive coupling between adjacent channels on the readout board.

When a charge is collected on one channel (ch_i) of the APV, it can induce a capacitive coupling on the adjacent channels ($ch_{i\pm 1}$ and $ch_{i\pm 2}$) due to their close proximity. This coupling can lead to a small signal being induced on these adjacent channels, even if no charge was collected there. The magnitude of this induced signal would depend on various factors such as the strength of the charge collected on the original channel, the distance between adjacent channels, and the capacitance between them.

We can evaluate 128x128 matrix of correlations of each channel pair for each APV card using Pearson's correlation coefficient.

The formula for Pearson's correlation coefficient (r) is:

$$r_{xy} \approx \frac{\sum_{i=1}^n (x_i - \bar{x})(y_i - \bar{y})}{\sqrt{\sum_{i=1}^n (x_i - \bar{x})^2 \sum_{i=1}^n (y_i - \bar{y})^2}} \quad (6.5.1)$$

where x_i and y_i are the i -th event of x and y , respectively, \bar{x} and \bar{y} are the sample means of x and y , n is the number of events. Note that this gets the matrix of the

Pearson correlation coefficient for all pairs of channels within each APV card, but not across different APV cards or detectors.

The Pearson correlation coefficient measures the linear relationship between two variables. If the value of r is close to 1, it indicates a strong positive correlation, meaning that as one variable increases, the other variable also tends to increase. If the value of r is close to -1, it indicates a strong negative correlation, meaning that as one variable increases, the other variable tends to decrease. If the value of r is close to 0, it indicates a weak or no correlation between the two variables.

The algorithm uses nested loops to iterate over the GEMs, APV cards, and channels in the system. It calculates the sum and square sum of the channel data and the product of pairs of channel data, using pedestal and common mode corrections. These values are then used to calculate the correlation coefficient for each channel pair and filled into a histogram.

As depicted in the Figure 6.7, The adjacent strips exhibit correlation due to the presence of real clusters, where clusters span across 3-4 strips. These correlations represent the desired signal and should be preserved. However, cross talk introduces unwanted correlations in the form of off-set diagonal bands at ± 32 and ± 64 channels. The ± 32 bands appear as greenish and are positively correlated, while the ± 64 bands appear as bluish and are negatively correlated. To suppress cross talk in the data set, we can utilize the information about the correlation patterns between adjacent strips and the off-set diagonal bands on the APV chip.

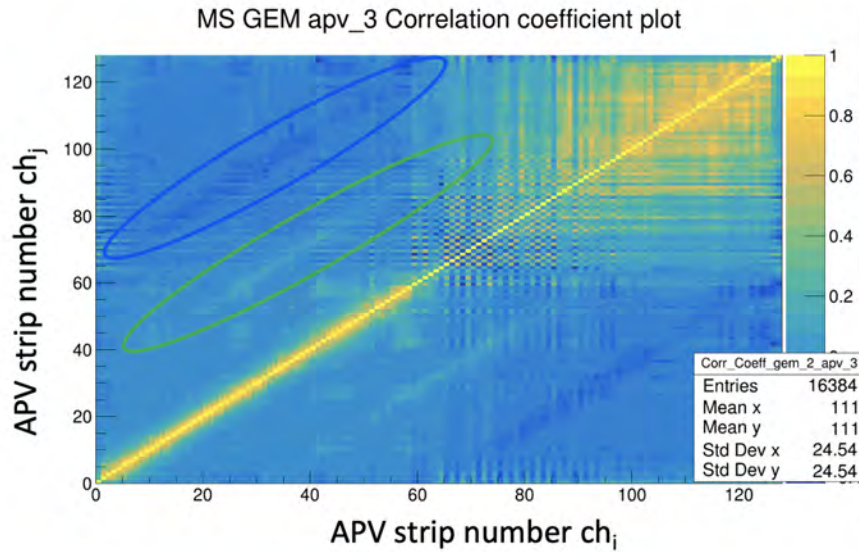


Figure 6.7. Example plot of correlation coefficient values of r_{xy} for 3rd APV card of MS GEM element. The values filled indicate the strength of correlation between ch_i and ch_j within the same APV card.

6.5.2 Suppression

Crosstalk can be a significant issue as it can lead to incorrect measurements and distortions in the data as mentioned earlier. Therefore, it is important to understand and mitigate the effects of crosstalk. Literature suggests that cross-talk suppression can be achieved by various methods, such as:

- Physical separation: Physical separation between adjacent channels can reduce cross-talk by minimizing the coupling between them.
- Shielding: The use of shielding materials can reduce the electromagnetic interference that leads to cross-talk.
- Signal shaping: Signal shaping can reduce cross-talk by adjusting the signal waveform to minimize the overlap with the cross-talk signal.
- Electronic balancing: Electronic balancing can reduce cross-talk by compensating for the induced signal in the affected channel with an opposite signal in the adjacent channel.
- Deconvolution: Deconvolution involves estimating and subtracting the cross talk contribution based on the knowledge of cross talk patterns.

In this particular case, considering the presence of cross talk in the form of off-set diagonal bands, we suggest that deconvolution or electronic balancing are the most effective methods for suppressing cross talk.

Deconvolution involves applying mathematical techniques to estimate and subtract the cross talk contribution from the data. It relies on the knowledge of the cross talk patterns and uses this information to deconvolve the data and recover the underlying signals. Deconvolution can be effective in mitigating cross talk effects, especially when the cross talk patterns are well-characterized. However, deconvolution can be computationally intensive and requires a good understanding of the cross talk behavior.

Electronic balancing involves compensating for the induced signal in the affected channel by introducing an opposite signal in the adjacent channel. By carefully adjusting the amplitudes and phases of the signals, electronic balancing can effectively cancel out the cross talk and minimize its impact on the measurements. This approach is especially useful in situations where physical separation or shielding is not feasible or sufficient to completely eliminate cross talk.

Cross talk can be effectively suppressed using another approach. It involves masking the ± 1 and ± 2 neighboring channels, effectively removing their contribution to the data analysis. By disregarding these immediate neighbors, the influence of cross talk can be significantly reduced. This approach may result in a loss of resolution and accuracy, as well as a reduction in the overall quality of the data. Furthermore, if there are any subtle correlations or patterns in the neighboring channels that are not solely due to cross talk, masking them would prevent their detection in analysis.

6.6 Cluster Finder Algorithms

Cluster finding is a fundamental task in GEM data analysis to determine the precise location of a real hit. Once the noise subtraction procedures have been per-

formed, the ADC spectra obtained from the GEM detector can be utilized to search for potential hit candidates. In the small area where a charged particle interacts with the GEM detector, a cluster of APV channels will exhibit ADC values that are substantially higher than those of other channels in the detector. Such selection of hit candidates is a critical aspect of the cluster finding process, as it involves identifying the most promising data points or "hits" that are likely to be part of a cluster.

Various cluster finding algorithms have been used. The first two hit candidate selection techniques have been developed and used in the past which was adopted from OLYMPUS experiment. The latter methods are recently integrated to GEM data analysis to find the optimum cluster finding algorithm.

1. The cluster finder developed by J. Diefenbach for the OLYMPUS experiment -

This uses a technique that involves fitting neighboring strips in 1D with a Gaussian function. The amplitude and integral of the fit are evaluated, and the correlation in X and Y is used to identify the (x,y) value of a 2D cluster. However, this approach is limited by several issues, including variations in cluster shape, gain, and efficiency per strip, which can lead to reduced efficiency in identifying clusters.

2. The cluster finder developed by B. Henderson for the OLYMPUS experiment -

This method identifies the (x,y) value of a 2D cluster by finding the maximum sum of ADC values of strips in X and Y. A pad of 5x5 strips is taken about the center (x,y), and the ADC values for all 25 are summed up or averaged (if pedestals are already subtracted). The 5x5 averages and variances are evaluated as a function of x and y, and a valid cluster is identified if the 5x5 average ADC is greater than 3x (5x?) that variance. The ADC-weighted average (centroid) of $\{x,y\}$ is then evaluated for the cluster location. Compared to v1, this cluster

finder is much more robust, as it goes directly to 2D, avoids Gaussian shape assumptions, and can still find a cluster even if some strips are masked

3. The Clustering by fast search and find of density peaks (CENsus) method by I. Lavrukhin -

This density-based clustering algorithm method was introduced by Alex Rodriguez and Alessandro Laio in 2014. It involves finding cluster centers or density peaks, which are defined as points with a high density of neighbors, and assigning points to the nearest density peak based on their density and distance. The algorithm does not require the number of clusters to be known in advance and can handle clusters of varying shapes and sizes.

4. K-Means Clustering by S. Reagan -

To solve the problem using K-Means clustering (ex: $K=2$), the first step is to randomly allocate two centroids. These centroids are initially not the central point of the data set but act as reference points. Next, the distance between each point and the two centroids is measured, and each point is assigned to the centroid with the shortest distance. The centroids are then repositioned to the actual centroid of their respective clusters, and the process of calculating distances and repositioning centroids continues until the algorithm converges and the final clusters are obtained. Once the algorithm has converged, the centroid repositioning stops, and we have the two clusters with their respective centroids.

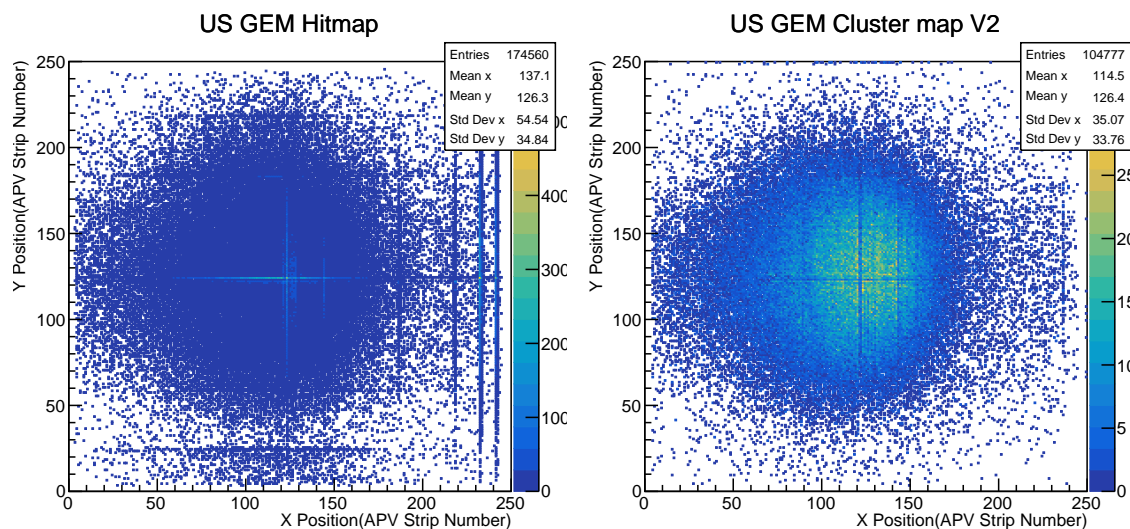


Figure 6.8. Histogram of cluster distribution map for US GEM element - using CENSus method (left) and K-Means clustering method (right).

On the left side, a histogram of the cluster map for a US GEM element is shown using the CENSus method. The histogram provides a visual representation of the distribution of clusters obtained through the CENSus method. While on the right side, a histogram of the cluster map for the same US GEM element is displayed, but this time using the K-Means clustering method. The K-Means clustering method groups the data points into clusters based on similarity, aiming to minimize the intra-cluster variance.

6.7 Detector Alignment Studies

Alignment studies are an important part of the detector characterization process to ensure their optimal performance. By aligning the GEM detectors accurately, one can maximize their sensitivity and efficiency in detecting charged particles or photons.

Alignment studies typically involve the precise positioning and calibration of the GEM detectors within the experimental setup. The goal is to achieve an optimal geometric arrangement, where the active areas of the detectors are properly aligned with the regions of interest or the particle trajectories.

The alignment process usually consists of several steps:

1. Mechanical alignment: This step involves positioning the GEM detectors within the experimental setup, ensuring their proper orientation and alignment with other detector components. This may involve careful adjustment of mounting brackets, supports, or positioning stages.
2. Position calibration: Once the detectors are mechanically aligned, their positions need to be calibrated accurately. This can be done using reference markers or known positions within the experimental setup. Precise measurements and adjustments are made to achieve the desired positions.
3. Performance verification: After the alignment process, it is crucial to verify the performance of the GEM detectors. This is typically done by using calibration sources or known particle beams to measure the detector's response, spatial resolution, and efficiency. These measurements can help identify any residual misalignments or performance issues that need to be addressed.

Note that alignment studies are iterative processes, and it may require multiple iterations to achieve the desired alignment accuracy. A survey was conducted by PSI survey group to take precise measurements of GEM detectors with respect to the MUSE setup.

Three types of data was collected for the alignment studies of GEM detectors within the same room coordinate frame. The horizontal and vertical offsets of the cross hairs give relative displacements, the 3D locations provide absolute spatial positions, and the evaluation of various points on the kapton foil helps to obtain more data points. A comprehensive understanding of the detector's alignment, positioning, and response characteristics within the experimental setup can be acquired by analyzing these data together.

1. Horizontal and vertical offsets of the cross hairs:

This provides relative displacements from a predefined reference position in the room coordinate frame. These offsets help determine the precise positioning of the detectors or other components relative to the reference point.

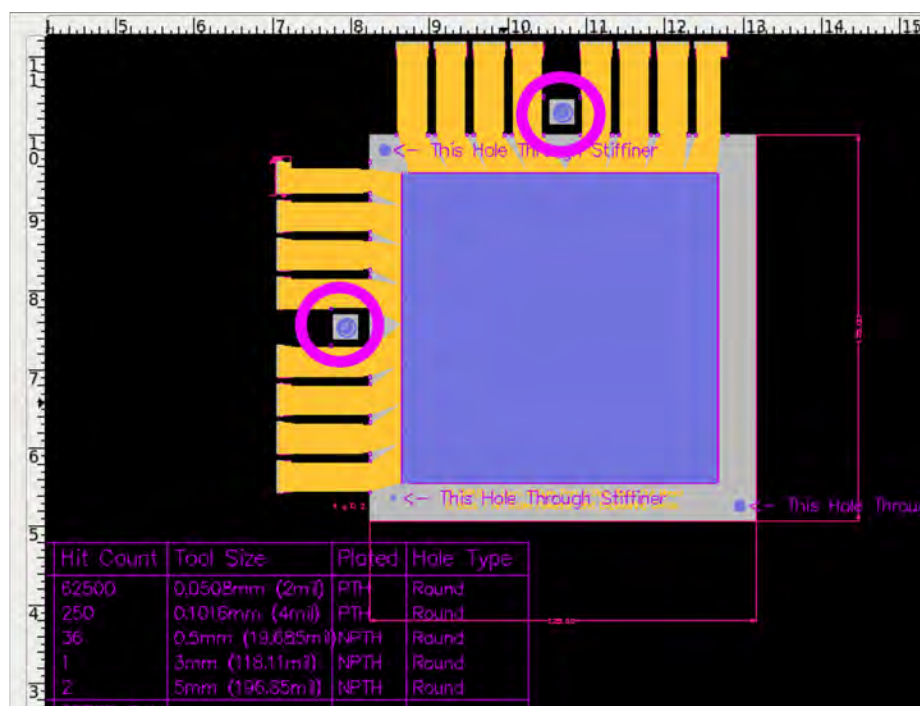


Figure 6.9. The horizontal and vertical cross-hairs on a GEM plane is visually emphasized with a purple circular outline.

2. 3D locations of cross hairs:

This refers to their positions in the three-dimensional coordinate system of the experimental setup. This includes their x, y, and z coordinates, which determine their spatial locations in the room. By measuring and evaluating the 3D positions of the cross hairs, you can assess the alignment and positioning accuracy of the detectors or other objects relative to the room coordinate frame.

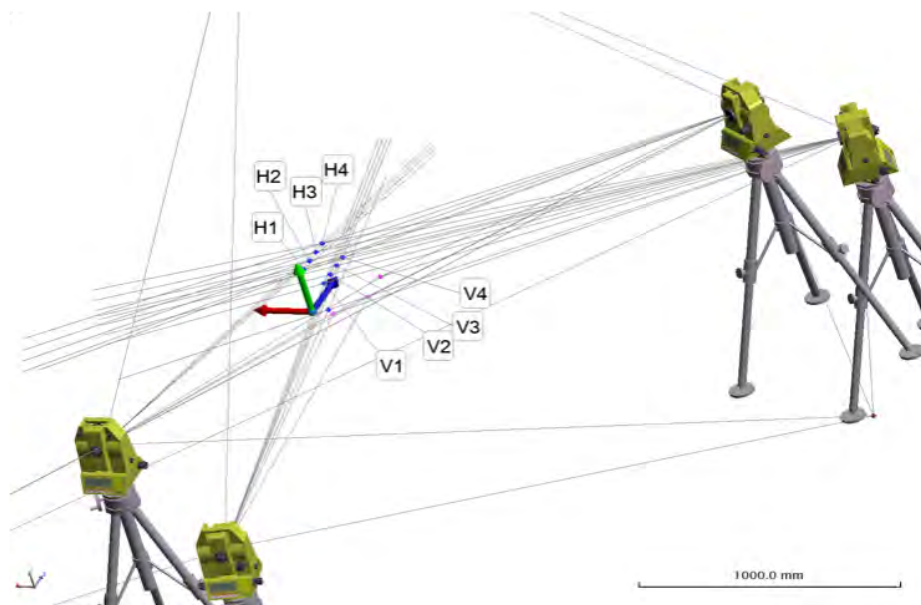


Figure 6.10. A visual representation illustrating the measurements conducted to obtain x, y, and z positions. The figure showcases the survey employed to calculate the precise coordinates of observed points in 3D space.

3. Various points on the kapton foil of the readout layer of each GEM:

GEM detectors typically consist of multiple layers, including a readout layer made of kapton foil. This layer contains various points of interest that are relevant for the detector's performance evaluation.

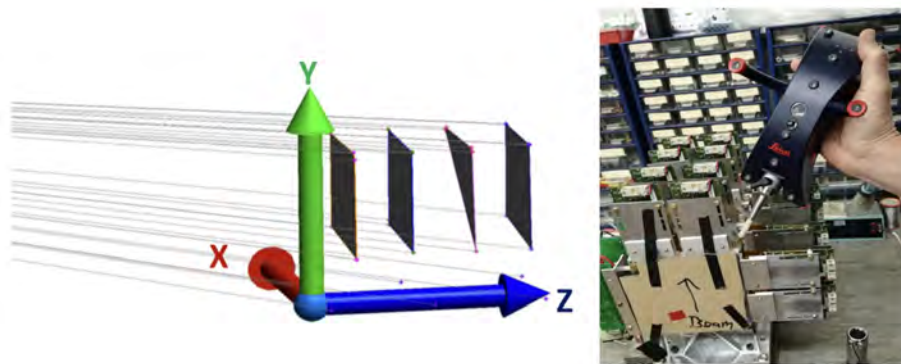


Figure 6.11. A picture illustrating the use of a handheld device for obtaining spatial coordinates of multiple points on a Kapton layer.

The alignment strategy involves a multi-step process to align the local GEM frame with the telescope frame and then align the telescope frame within the MUSE frame.



Figure 6.12. A figure illustrating a sequence of frames from left to right: local frame, telescope frame, and MUSE frame.

First, the local GEM frame is aligned with the telescope frame using a series of transformations. This includes a translation to move the origin of the local GEM frame to the origin of the surveyed telescope frame, as well as three rotations around the X, Y, and Z axes to adjust the orientation. The transformation is represented by the matrix $T R_Y R_X R_Z$, where T represents the translation and R_X , R_Y , R_Z represent the rotations.

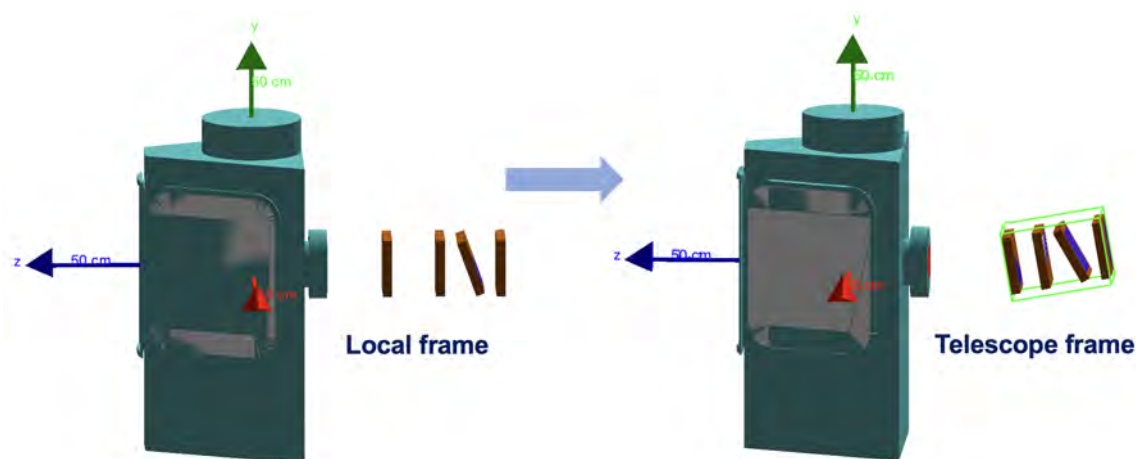


Figure 6.13. Geant4 illustration of the local frame and telescope frame in relation to the MUSE target. The illustration depicts the coordinate orientation, where the z-axis aligns with the beam direction, the y-axis points upwards, and the x-axis extends out of the plane.

Once the alignment between the local GEM frame and the telescope frame is achieved, the next step is to align the telescope frame within the MUSE frame. This is done by utilizing the survey of the base plate reflectors in the MUSE frame. The positions and orientations of the base plate reflectors are measured, providing reference points within the MUSE frame. The transformation matrix $T R_Y R_X R_Z$ is then used to align the telescope frame with the MUSE frame, taking into account both the position and orientation adjustments required.

By combining these alignment steps, the local GEM frame is ultimately aligned with the MUSE frame. This alignment enables accurate positioning and orientation of the GEM detectors within the MUSE frame, ensuring their proper functioning and compatibility with the experimental setup. The alignment parameters obtained from the survey and minimization process can be directly incorporated into the simulation code, Geant4, allowing for realistic and precise particle tracking and analysis within the aligned frames. The transformation matrix, used for aligning the local frame to the telescope frame and subsequently to the MUSE frame, was calculated and incorporated into the alignment strategy by Tanvi Patel, from Hampton University.

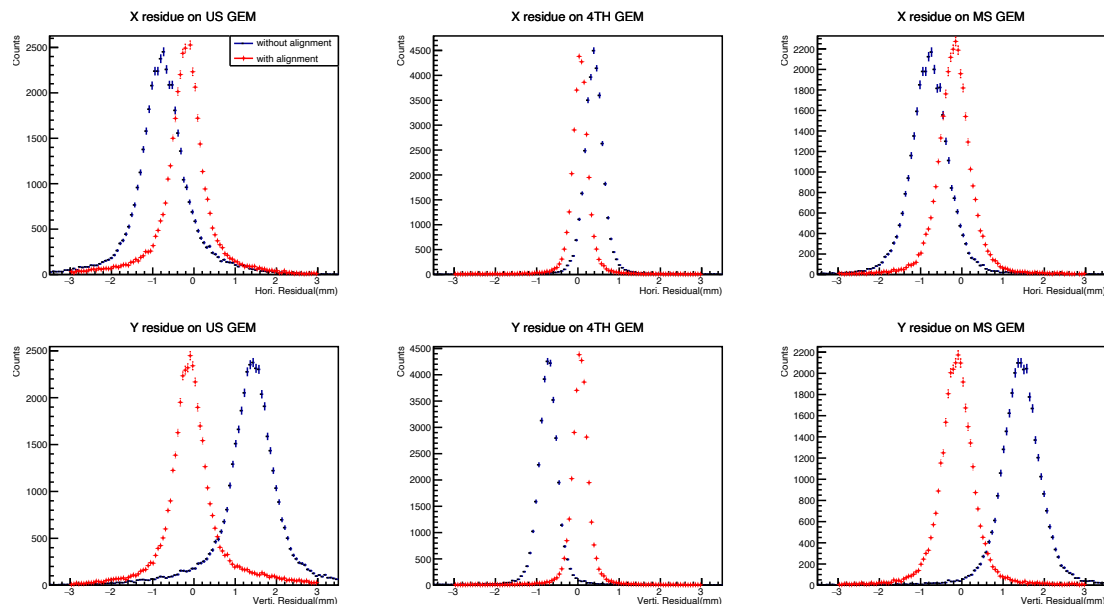


Figure 6.14. The histograms displaying track residuals of a 3 GEM setup before (blue) and after (red) alignment procedures along the X and Y axes for the US, 4TH, and MS GEMs highlighting the improved alignment accuracy achieved through the alignment procedures, validating the successful transformation of coordinates across the different frames of reference

As shown in Figure 6.14, the histograms show the track residuals of a 3 GEM setup before and after alignment procedures along the X and Y axes for the US, 4TH, and MS GEMs. The histograms provide valuable insights into the effectiveness of the alignment procedures by illustrating the centered distribution of the track residuals after alignment (red). This centered distribution indicates the successful transformation of coordinates from the local frame to the telescope frame and further to the MUSE frame.

The geometric information of the MUSE experiment is efficiently managed using a graphic description markup language (gdml) generated by the MUSE Geant4 package. The gdml file preserves essential details regarding the experiment's geometry and alignment. For incorporating alignment corrections, Geant4 messenger files play a crucial role, enabling direct adjustments as needed.

To ensure consistency and accuracy throughout the simulation and analysis processes, the COOKER code relies on the gdml source for analysis. By utilizing this shared data set of alignment and geometry, the simulation and analysis procedures maintain uniformity, reducing the risk of discrepancies and enhancing the reliability of the results obtained. This approach facilitates efficient data management and facilitates an accurate portrayal of the MUSE experiment's behavior, laying the groundwork for reliable analysis with multiple detectors.

6.8 Study of GEM Efficiencies

The efficiency of a GEM detector plane refers to its ability to detect and record charged particle hits passing through the detector. It is calculated as the ratio of the number of detected hits to the number of expected hits based on the trajectory of the charged particle passing through the detector.

The GEM efficiencies were calculated for both the three GEM and four GEM configurations, considering two scenarios: with and without a beam hodoscope. The inclusion of a beam hodoscope provides additional position information about the incoming particle beam. By comparing the efficiency values obtained for low and high rates in these different setups, an informed decision can be made regarding the optimal GEM setup for the MUSE experiment. The efficiency values obtained under varying conditions will shed light on the performance and robustness of each configuration, ultimately guiding the selection of the most suitable GEM setup to ensure accurate and reliable physics data analysis in the MUSE setup.

6.8.1 Three GEM vs. Four GEM Configuration

In this study, we explore and compare the efficiency of two different configurations: a three GEM setup and a four GEM setup. By examining the efficiency of these

two configurations, we aim to understand the impact of the number of GEM planes on the overall detection capabilities. This analysis will provide valuable insights into the optimal design of detector systems for precise and efficient particle track reconstruction for MUSE experiment.

In first setup, we have used three GEM detectors to measure the position of charged particles passing through them as shown in Figure 6.15. By analyzing the hit positions of two of the three planes, we have reconstructed the trajectory of the charged particle and projected it onto the third GEM plane. The projected position and the actual hit position on the third GEM plane were then compared to evaluate the performance of the GEM detectors.

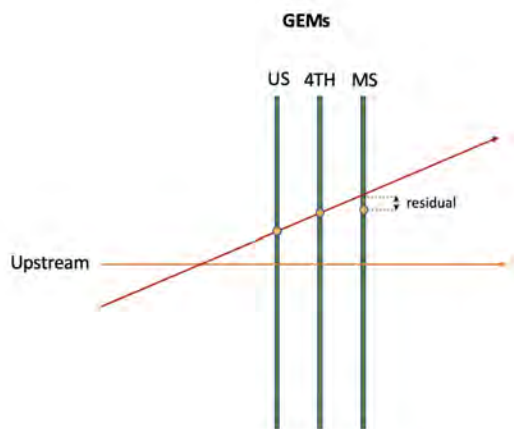


Figure 6.15. Schematic representation of a hit passing through gem detector setup consisting of three planes and a track formed by two detectors projected onto the third plane. Residuals between the measured positions of the track and the expected positions are examined for precise track reconstruction.

In the algorithm to find the detector efficiencies, we applied several conditions and constraints when creating tracks. First, we ensured that the cluster positions used to reconstruct the particle trajectory were inside the active area of the detectors. This was important to eliminate any spurious data points or outliers that may have been caused by noise or other factors. Second, we only considered the maximum charge

cluster for each detector when reconstructing the particle trajectory. This was done to minimize the effects of noise and to improve the accuracy of the reconstructed trajectory. By selecting only the cluster with the highest charge, we ensured that the most significant and reliable data points were used in the reconstruction of the particle trajectory. Then we imposed that the actual cluster be inside the vicinity of ± 10 mm range to the projected track location. The efficiency can be calculated by,

$$\epsilon = \frac{\text{No. of tracks projected on 3rd GEM with fiducial cuts}}{\text{No. of tracks projected on 3rd GEM [when GEM 1 \& 2 have at least one cluster]}} \quad (6.8.1)$$

Track selection is common to both numerator and denominator; however additional constraints are to be fulfilled for the numerator entries. The condition for fiducial cuts is that the projection falls within the acceptance region, i.e active area of the detector. Additionally, there is a requirement to apply a cut on the track-vs-hit residual within a defined vicinity, which is 10 mm in this case.

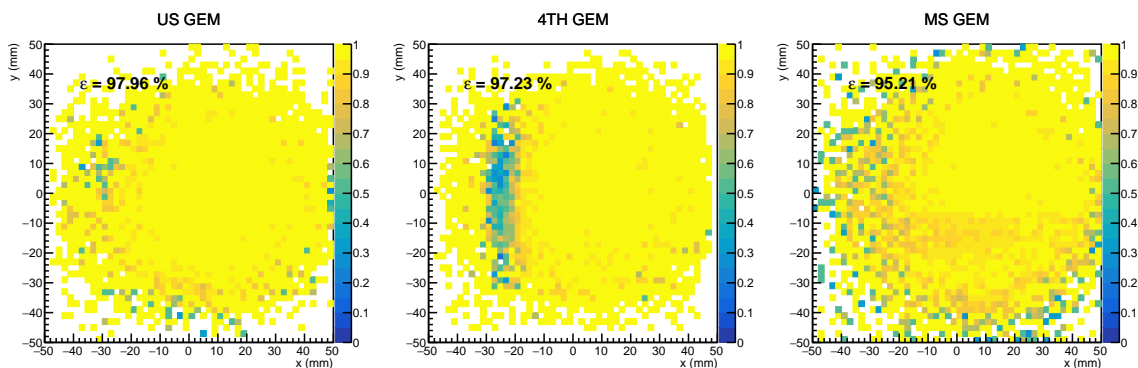


Figure 6.16. Efficiency of US, 4TH and MS planes for 2 of 3 GEMs; Low rate run 100 kHz, 100k events.

Figure 6.16 shows the efficiency plots of X (mm) vs Y (mm) for US, 4TH and MS GEM detectors. The efficiency maps are 2D histograms obtained from the ratio of two 2D histograms for the distributions of candidate tracks with (numerator) and

without (denominator) additional constraints to probe the third GEM. It provide a spatial representation of the detection efficiency across the detector surface. These plots showcase how the efficiency of the detectors varies as a function of the position of incident particles. Each point on the plot corresponds to a specific location on the detector surface. The efficiency value associated with each point represents the proportion of incident particles that are successfully detected at that particular position. Efficiency values are represented using a color scale, where darker shades of yellow corresponds to higher efficiency and darker shades of blue corresponds to lower efficiencies.

Overall, the efficiency values are in the range of 95-97% but there are some blue spots scattered closer to edge of the detectors, where more prominent inefficient spot visible on the 4TH GEM detector. We will further analyze these inefficiencies in section 6.8.2.

Next, we extended our investigation to include four GEM detectors to measure the position of charged particles passing through them as shown in Figure 6.17. Using the hit positions of three of the four planes, we reconstructed the trajectory of the charged particle and projected it onto the fourth GEM plane by applying the least square fit method. The least square fit method provides an optimal solution to minimize the sum of the square of residuals between the measured positions and the predicted positions of the charged particle.

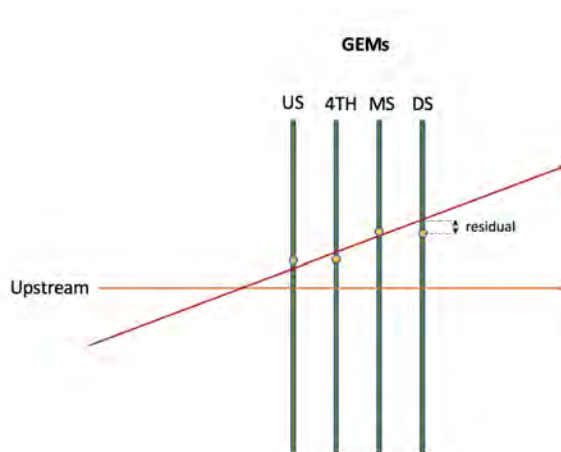


Figure 6.17. Schematic representation of a hit passing through gem detector setup consisting of four planes and a track formed by three detectors projected onto the fourth plane. Residuals between the measured positions of the track and the expected positions are examined for precise track reconstruction.

Figure 6.18 shows the efficiency plots of X (mm) vs Y (mm) for US, 4TH and MS and DS GEM detectors. Notably, similar inefficient regions are observed on the edges of all detectors. Specifically, a distinct blue spot is visible on the efficiency plot of the 4TH GEM detector. Additionally, the DS GEM element exhibits an efficiency of 90%, which is comparatively lower than the other three detectors. These observations highlight spatial variations in the detection efficiency within the four GEM detectors, with certain regions exhibiting reduced efficiency compared to others. This lower efficiency suggests that the DS GEM element may have certain characteristics or conditions that lead to a reduced probability of successfully detecting incident particles in that particular region. The lower efficiency observed in the DS GEM element compared to the other three detectors could also be linked to the effects of multiple scattering. A possible source of false inefficiency is random triggers in combination with noisy GEM hits generating false track candidates. We will conduct further investigations by imposing stringent conditions to evaluate these inefficiencies. We aim to validate whether the identified inefficiencies are inherent limitations of the detector system or if they are artifacts caused by external factors.

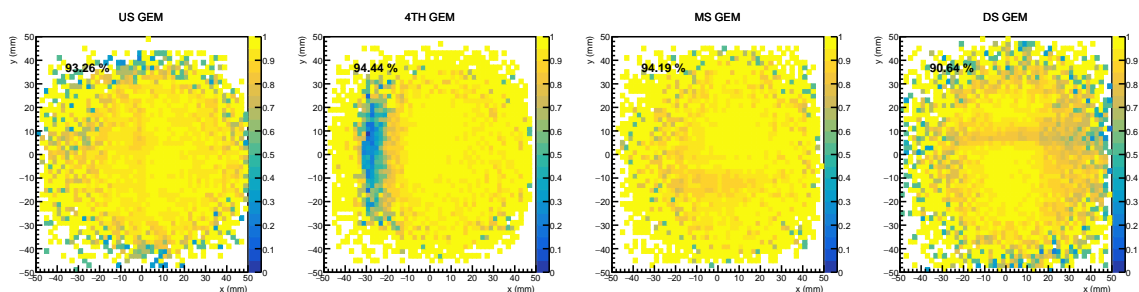


Figure 6.18. Efficiency of US, 4TH, MS and DS planes for 3 of 4 GEMs; Low rate run 100 kHz, 100k events.

6.8.2 Three GEM vs. Four GEM Configuration in the Presence of BH Hits

The beam hodoscope detector is positioned upstream of the GEM detector. The BH detector can be used to provide additional information about the charged particles passing through the detector system. In this section, to calculate the efficiencies of the GEM detectors, a specific condition was applied to the analysis. Specifically, only events where BH planes C and D had one in-time hit and correlation of projected GEM track with BH hit location were used for efficiency calculations. This ensured that the charged particle passed through the BH detector and was subsequently detected by the GEM detectors. For events meeting this condition, two GEM elements were used to project the track to the other GEM element in 2-of-3 GEM configuration as shown in Figure 6.19. This allowed for improved accuracy and precision in the measurement of the charged particle's position and trajectory. By using information from both the BH and GEM detectors, the overall efficiency of the detector system could be calculated and evaluated. This provides a more comprehensive analysis of the performance and efficiency of the GEM detectors by cleaning up the set of candidate tracks. The condition applied to the analysis ensured that only events with a clear and unambiguous detection of the charged particle were used for efficiency calculations.

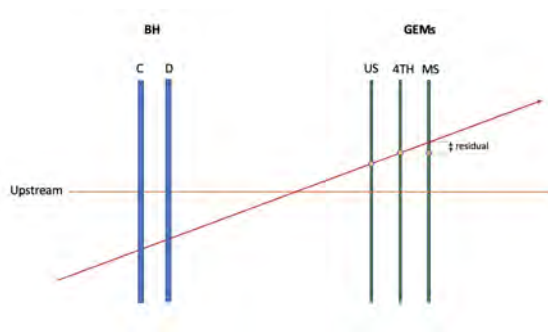


Figure 6.19. Schematic illustrating a hit passing through 3 GEM detector planes with the condition that the particle had passed through BH planes when in-time hits = 1.

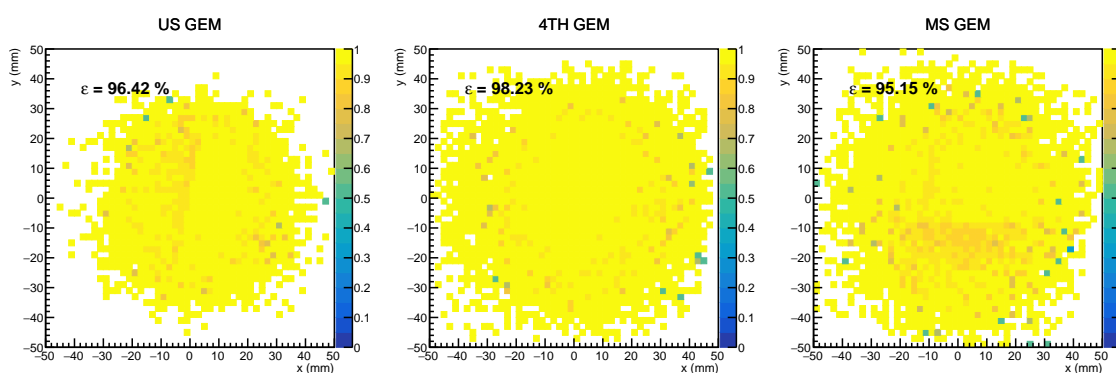


Figure 6.20. Efficiency of US, 4TH and MS planes for 2 of 3 GEMs with BH; Low rate run 100 kHz, 100k events

The procedure of incorporating the track from two GEM detectors and utilizing BH has yielded significant improvements in efficiencies. If we observe the plots shown in Figure 6.20, this procedure has effectively minimized the presence of scattered blue spots, which were previously observed in the efficiency plots in Figure 6.16. In addition to the efficiency improvement, it has been observed that the number of events has decreased. This reduction can be attributed to the implementation of a cut condition that includes only BH in-time hits, effectively eliminating scattered blue spots, indicative of regions with lower detection efficiency. This selective process allows for a more focused analysis, emphasizing the desired events of interest for the GEM detectors.

We repeated the same process for 3-of-4 GEM detectors configuration as depicted in Figure 6.21.

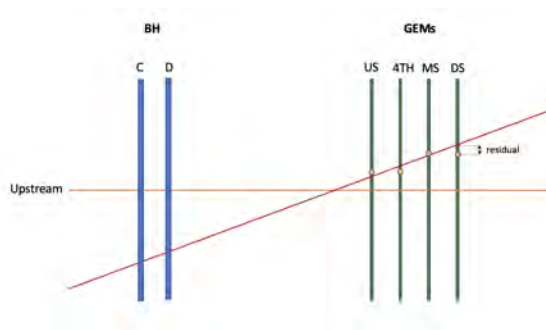


Figure 6.21. Schematic illustrating a hit passing through 4 GEM detector planes with the condition that the particle had passed through BH planes when in-time hits = 1.

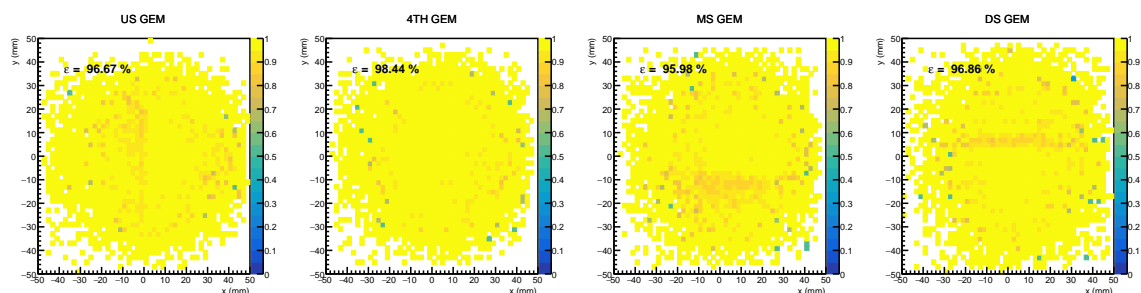


Figure 6.22. Efficiency of US, 4TH, MS and DS planes for 3-of-4 GEMs with BH; Low rate run 100 kHz, 100k events

As expected, the procedure of incorporating the track formed by three GEM detectors and utilizing BH information in 3-of-4 GEM detector setup has led to significant improvements in efficiencies as shown in Figure 6.22, resulting in minimized scattered blue spots compared to 3-of-4 GEM case shown in Figure 6.18.

A crucial step in the efficiency analysis process involves verifying the correlation between the tracks generated using the 3-of-4 GEM detectors and the actual hit positions obtained from the Beam Hodoscope. To ensure this alignment, histograms are employed, allowing for a comprehensive examination. The histograms serve as a

valuable tool in assessing the consistency and accuracy of the track reconstruction process, validating the correspondence between the GEM detector measurements and the precise hit positions provided by the Beam Hodoscope.

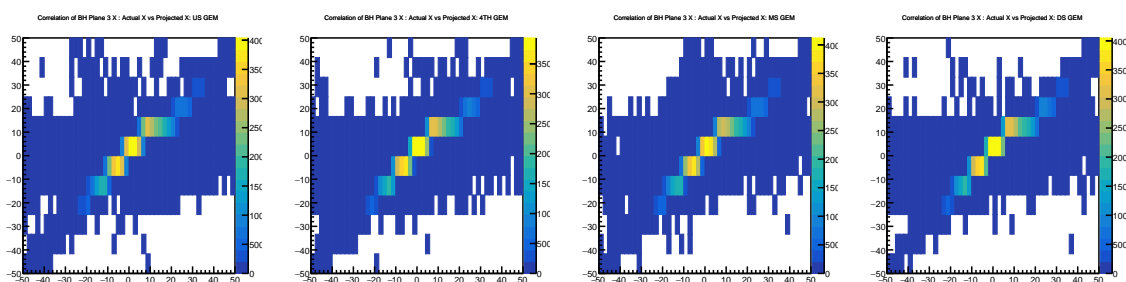


Figure 6.23. Correlation between actual hit position and projected hit position of Beam Hodoscope plane 2; Low rate run 100 kHz, 100k events

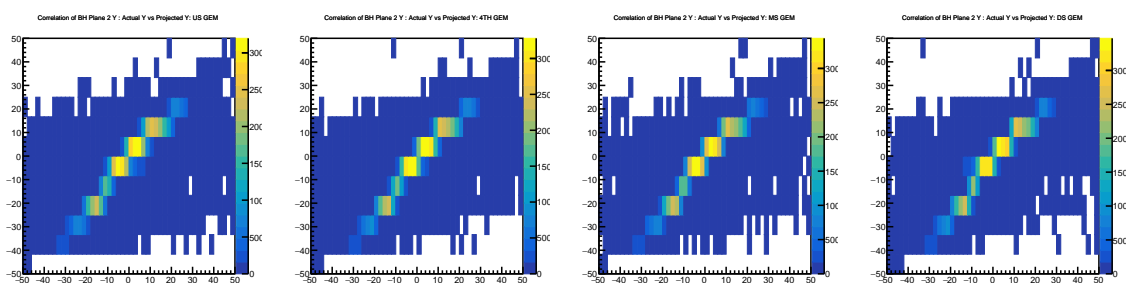


Figure 6.24. Correlation between actual hit position and projected hit position of Beam Hodoscope plane 3; Low rate run 100 kHz, 100k events

In Figure 6.23, correlation plots for beam hodoscope plane 2 are depicted. The tracks, generated using the 4th, MS, and DS detector planes, are projected onto the BH plane in the first histogram. Each histogram corresponds to a specific combination of detectors used to construct the tracks. The Y-axis represents the actual hit positions, while the X-axis represents the projected hit positions. The plot reveals a strong correlation, indicating excellent track reconstruction accuracy. The robust correlation between the actual and projected hit positions validates the reliability

and precision of the track reconstruction process. Similarly, in Figure 6.24, correlation plots for beam hodoscope plane 3 are shown. The strong correlations observed across the histograms further confirm the accuracy of efficiency analysis.

Furthermore, we conducted the same analysis of the efficiency plots under high-rate beam conditions at 2.2 MHz. The efficiency plots are presented in ascending order from the least constraining setup to the most stringent setup, namely: 2-of-3, 2-of-3 with BH information, 3-of-4, and 3-of-4 with BH information. By comparing these different setups, we can evaluate the impact of increasing constraints on the detection efficiency.

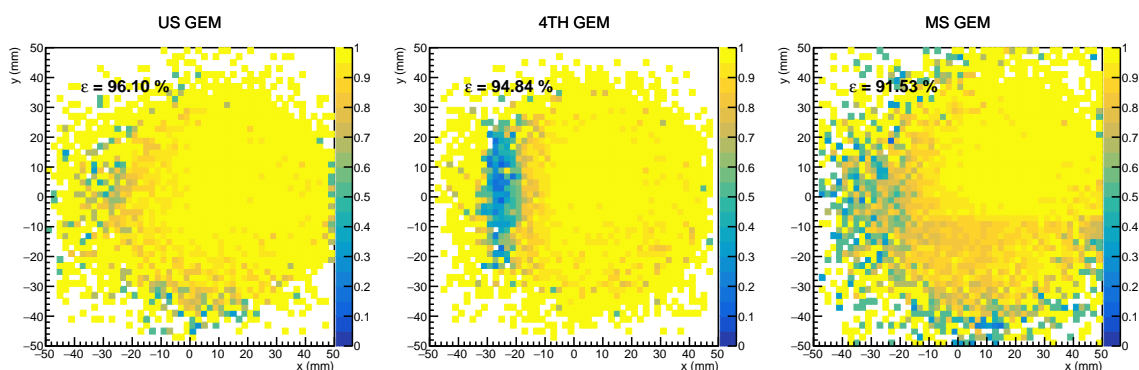


Figure 6.25. Efficiency of US, 4TH, MS and DS planes for 2 of 3 GEMs; High rate run 2.2 MHz, 100k events.

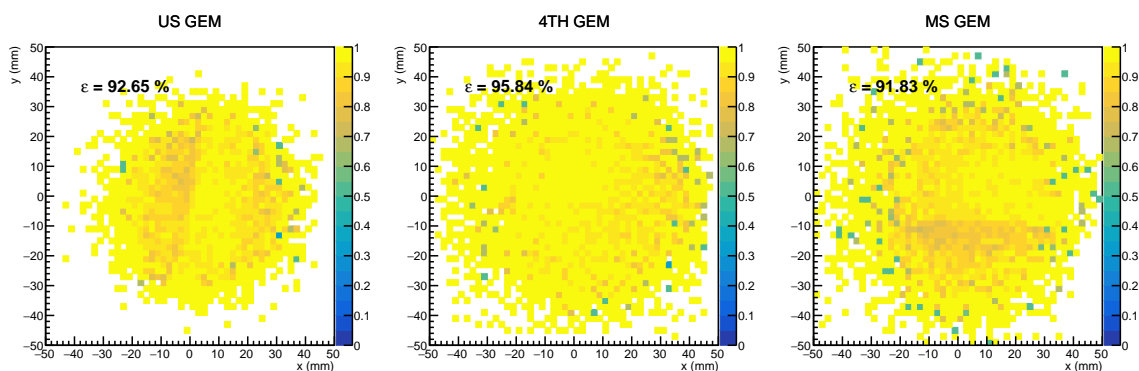


Figure 6.26. Efficiency of US, 4TH and MS planes for 2 of 3 GEMs with BH; High rate run 2.2 MHz, 100k events.

The 2-of-3 setup, where at least two out of three detectors must detect the particle, represents a relatively less stringent requirement. The addition of BH information further refines the detection process in the 2-of-3+BH setup.

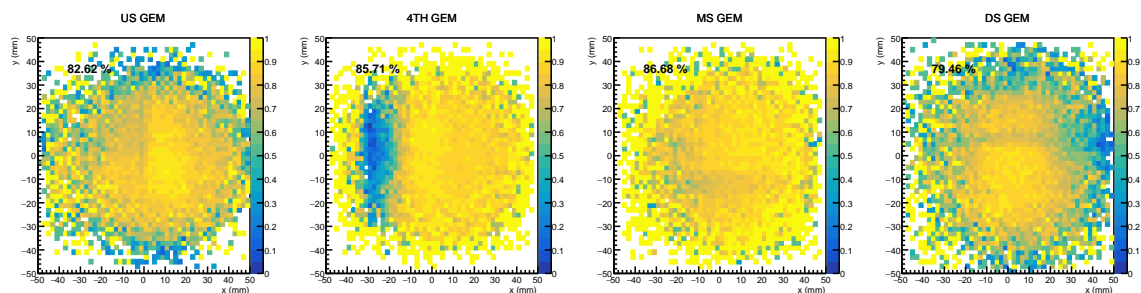


Figure 6.27. Efficiency of US, 4TH, MS and DS planes for 3 of 4 GEMs; High rate run 2.2 MHz, 100k events.

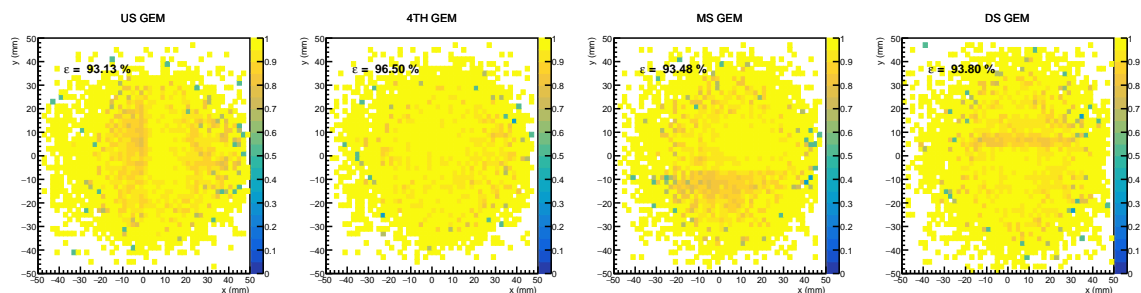


Figure 6.28. Efficiency of US, 4TH, MS and DS planes for 3 of 4 GEMs with BH; High rate run 2.2 MHz, 100k events.

Moving on to the 3-of-4 setup, where at least three out of four detectors must detect the particle, we observe increased constraints. Finally, the 3-of-4+BH setup incorporates BH information to further enhance the detection performance in the most stringent configuration.

6.9 Results

By examining the efficiency plots in the above order, we can observe the gradual improvements in detection efficiency as the constraints are tightened. The results are shown in Table 6.1.

Table 6.1

Efficiency Values for Low and High Rate Runs for Each Case

	Low Rate				High rate			
	US	4TH	MS	DS	US	4TH	MS	DS
2 of 3 GEMs	97.96	97.23	95.21	–	96.10	94.84	91.53	–
2 of 3 GEMs with BH	96.42	98.23	95.15	–	92.65	95.84	91.83	–
3 of 4 GEMs	93.26	94.44	94.19	90.64	82.62	85.71	86.68	79.46
3 of 4 GEMs with BH	96.67	98.44	95.98	96.86	93.13	96.50	93.48	93.80

For low-rate scenarios, the efficiencies of the 2-of-3 configuration with BH constraint are comparable to those of the 3-of-4 configuration with BH constraint. This suggests that both setups perform similarly in terms of particle detection and tracking.

However, in high-rate scenarios, the 2-of-3 configuration with BH constraint exhibits lower efficiencies compared to the 3-of-4 configuration with BH constraint. This discrepancy highlights the importance of additional measurement points provided by the fourth GEM detector, which serves to improve the detection and tracking of charged particles passing through the system. Furthermore, with per-plane efficiencies reaching approximately 94% at high rates, the use of three GEMs for track reconstruction yields an overall tracking efficiency of around 83% ($0.94^3 \approx 83\%$). The resulting 17% loss in efficiency can be significantly recovered with a four-GEM setup, where the requirement of any three out of the four GEMs to form a track leads to an improved tracking efficiency of approximately 99.5% ($(1-0.17^3) \approx 99.5\%$).

In an ideal scenario, the reconstructed tracks of particles should accurately align with the locations where hits are expected to occur in the detection system. However, in the efficiency plots, the presence of blue spots indicates potential inefficiencies in the detection process. These blue spots represent regions where the reconstructed tracks of particles would point to locations where hits should not occur.

The presence of these blue spots suggests the possibility of misalignment or discrepancies between the reconstructed tracks and the actual hit positions. This misalignment can result from various factors such as inaccuracies in the track reconstruction algorithm, unreliable cluster position extraction, errors in cluster finder algorithms, non-uniformities in the detector response, or the presence of background noise or unwanted signals.

However, when incorporating the BH constraint, these blue spots are minimized, and the efficiencies of the detection system significantly increase. The BH constraint provides additional information that helps refine the track reconstruction process. By imposing the BH constraint, the detection system becomes more selective, considering only the in-time hits that are consistent with the beam trajectory. This helps filter out background noise and unrelated signals, reducing the occurrence of blue spots that indicate potential inefficiencies. As a result, the efficiencies of the detection system improve, as the reconstructed tracks now align more closely with the actual hit positions.

To effectively clean the candidate tracks and remove any potential false detections, it is recommended to impose an in-time condition and establish a correlation with the BH bars. The in-time condition involves considering only the hits that occur within a specific time window relative to the beam arrival time. By enforcing this condition, background noise and unrelated signals that may fall outside the designated time range can be filtered out, ensuring that only genuine particle tracks are retained for further analysis.

In addition to the in-time condition, establishing a correlation with the BH bars can provide valuable information for track verification. The BH bars provide position measurements of the beam particles, allowing for the comparison and alignment of the detected tracks with the expected beam trajectory. By correlating the detected tracks with the BH bar information, false tracks can be identified and eliminated, enhancing the overall reliability of the reconstructed tracks.

By imposing both the in-time condition and utilizing the correlation with the BH bars, the cleaning process effectively removes fake tracks or false detections, resulting in a more accurate and trustworthy data set for analysis. This approach ensures that only genuine particle tracks are considered for track reconstruction. Therefore, the utilization of the BH constraint plays a crucial role in improving efficiencies and minimizing the occurrence of inefficient spots.

By using three GEM detectors, we can reduce the amount of material in the active area of the detector system while still maintaining an adequate measurement point density. This can help to minimize the effects of multiple scattering, as the reduced amount of material means that there are fewer interactions that can cause deflection of the charged particle.

However, when considering the four GEM detector configuration, additional benefits emerge. By using four GEM detectors, we can increase the probability of detecting charged particles passing through the detector system by increasing the number of measurement points. The inclusion of a fourth GEM detector serves to minimize the risk of missing a charged particle, which otherwise can result in a loss of important experimental data.

Considering both advantages, it can be concluded that the four GEM detector setup is preferable. It not only provides the benefits of reducing material effects on multiple scattering but also improves the overall detection efficiency by offering increased redundancy and minimizing the chances of missing charged particles.

CHAPTER 7

CONCLUSION AND DISCUSSION

7.1 GEM Detector Construction for DarkLight@ARIEL Experiment

The DarkLight@ARIEL experiment aims to shed light on the mysteries of dark matter by investigating the existence of a mediator for a potential new interaction between our observable world and the dark sector. This mediator, known as the dark photon or A' , is a prime candidate for understanding the nature and properties of dark matter. The experiment focuses on the X17 particle, a hypothetical fifth force carrier with a mass of around $17 \text{ MeV}/c^2$, which has been suggested by anomalies observed in recent experiments.

The experimental setup utilizes a high-intensity electron beam from the Advanced Rare IsotopE Laboratory (ARIEL) e-linac at TRIUMF to collide with a tantalum target. By measuring the scattering process of electrons and detecting the subsequent decay of the dark photon into electron-positron pairs, the experiment aims to explore the kinematic region associated with the proposed fifth force carrier.

The projected scope of the DarkLight@ARIEL Experiment demonstrates its potential sensitivity and reach in the search for the dark force carrier. With 1000 hours of beam time, the experiment can probe the upper portion of the proposed fifth-force parameter space. By focusing on the 17 MeV region, the experiment has the potential to discover the proposed particle or set strict limits on its interaction with ordinary matter.

The DarkLight experiment is set to commence with commissioning scheduled for 2024 and physics data taking planned for 2025. As part of the experimental setup, GEM detectors are utilized as particle tracking detectors.

During our research, we have focused on the development and improvement of the NS2 technique, which has shown great promise in GEM construction. Our efforts have resulted in an enhanced version of the NS2 method, providing numerous advantages over conventional assembly methods. It is noteworthy that the upgraded NS2 method boasts minimal material in the active area of the GEM detectors. This design improvement has been achieved through iterative collaboration between our research group and CERN, ensuring the optimization of the detector's performance.

To aid in the visualization and simulation of the GEM detectors, 3D illustrations have been generated. These illustrations can be utilized in Geant4 simulations or Monte Carlo simulations for more accurate modeling of particle interactions and detector responses in the future.

As part of this work, we have successfully produced eight new GEM elements. These elements underwent rigorous gas tightness tests and high voltage tests using nitrogen to ensure their operational integrity. Furthermore, three GEM detectors were shipped to Sendai, Japan for use in the ULQ2@ELPH experiment. Preliminary testing of these detectors has demonstrated their operability and functionality in detecting particles.

During the testing and validation phase, five of the GEM detectors were evaluated at Jefferson Lab and the detectors underwent gas testing procedures to ensure their functionality and performance in the intended experimental environment. Additionally, two detectors that required repairs while in Sendai were subsequently sent back to CERN for necessary refurbishment. The repaired detectors were received back from CERN in the fall of 2022 and are currently undergoing testing at LERF at Jefferson Lab. These gas tests and high voltage tests are essential for verifying the detectors' functionality and validating their readiness for the DarkLight experiment. Finally the detectors will be read out with an improved DAQ system adapted

from the MUSE experiment and tested with Sr-90 source and cosmic rays to evaluate efficiencies.

With the ongoing testing and validation process, we anticipate utilizing four of the GEM detectors in the DarkLight experiment at ARIEL in the spring of 2024 for phase I. The selection of these four detectors is based on their successful performance during testing and their suitability for the specific experimental requirements.

These achievements highlight the progress made in GEM detector development for the DarkLight experiment. The improved NS2 method offers enhanced performance and reliability, making it a promising technique for future particle tracking applications. With the successful production and testing of GEM elements, we are confident in the readiness and effectiveness of the GEM detectors for the upcoming DarkLight experiment.

Moving forward, further research and development will continue to refine the GEM detectors and optimize their performance. The valuable insights gained from these efforts will contribute to the overall success of the DarkLight experiment, enabling precise particle tracking and providing crucial data for studying fundamental physics phenomena.

7.2 GEM Data Analysis for MUSE Experiment at PSI

The proton's charge radius has been a subject of intense investigation due to discrepancies between measurements from muonic hydrogen and electron-based methods. Despite the consistent results obtained from nuclear scattering and spectroscopy, the precise measurement of the proton's charge radius using muonic hydrogen Lamb shift revealed a significant discrepancy.

The proton radius puzzle, arising from the 7σ difference between electronic and muonic measurements, remains unresolved due to the lack of existing data with the required precision. To address this challenge, the MUSE experiment has emerged with

the aim of simultaneously measuring the elastic scattering cross-sections of $\mu^\pm p$ and $e^\pm p$. This groundbreaking approach allows for a direct and highly precise comparison between elastic scattering of electrons and muons with protons, surpassing previous limitations at lower values of Q^2 .

Furthermore, the MUSE experiment will investigate the effects of two-photon exchange (TPE) at sub-percent levels with unprecedented accuracy by examining cross-section differences between positively and negatively charged particles. This comprehensive study will provide invaluable insights into the proton's charge radius and shed light on the fundamental properties of the composite particle.

Through the efforts of the MUSE experiment, we anticipate making significant advancements in our understanding of the proton's charge radius puzzle. The precise and direct measurements facilitated by this experiment have the potential to reconcile the discrepancies between previous muonic and electronic measurements, leading to a more comprehensive and accurate characterization of the proton's internal structure.

The MUSE experiment has progressed according to the proposed timeline. One month of scattering data was collected in 2022, and approval was granted for five months of beamtime in 2023. Subsequent years, from 2024 to 2025, are dedicated to production of data taking, with six months per year allocated for this purpose. The analysis of physics data is ongoing, spanning the period from 2023 to 2026.

GEM detectors play a vital role in the MUSE experiment as particle tracking detectors. To ensure accurate and reliable data analysis, various pre-processing techniques have been implemented for GEM data. These include adjusting the number of samples read, improving compilation time, and generating diagnostic plots for detailed analysis.

One of the challenges faced is the presence of false clusters that can generate erroneous tracks, leading to detector inefficiencies. To mitigate this issue, it is crucial to identify and address hot/dead channels before applying cluster finding algorithms.

Additionally, the influence of cross-talk, which can induce fake clusters, is monitored by plotting correlation coefficients for each channel. While efforts have been made to suppress cross-talk, further development of more complex algorithms may be necessary for its complete removal.

Two cluster finding algorithms, based on higher neighbor density and nearest neighbor approaches, have been utilized in the evaluation of GEM detector efficiencies. Efficiencies have been assessed for both 2-of-3 and 3-of-4 GEM detector configurations, with and without the BH constraint.

Notably, the results obtained from the 3-of-4 GEMs with the BH constraint have highlighted the presence of false inefficiencies. This discovery suggests the potential for further improvement by refining the data selection process and utilizing cleaner samples by integrating information from BH.

In conclusion, the MUSE experiment has made significant progress in data collection and our group has made notable contributions to the collaboration by providing manpower in data collecting and maintaining GEM detectors. Our efforts have been dedicated to refining the pre-processing techniques for GEM data. Adjustments aiming to improve the compilation time and implementation of numerous diagnostic plots has enhanced the ability to evaluate and diagnose potential issues in the data. By addressing false clusters, mitigating cross-talk effects, and optimizing the cluster finding algorithms, the overall performance of the GEM detectors can be improved.

The identification of false inefficiencies through the assessment of 4 configurations have been evaluated. To better assess efficiencies, the combination of in-time hits and correlation with the BH data has proven to be beneficial. This approach provides a more comprehensive understanding of the detection system's performance and helps identify potential inefficiencies.

The discussion surrounding the choice between three GEM detectors and four GEM detectors in the MUSE experiment revolves around the trade-off between ma-

terial reduction and improved detection efficiency. With three GEM detectors, the amount of material in the active area of the detector system is minimized, resulting in fewer interactions that can cause deflection of charged particles. This reduction in material helps mitigate the effects of multiple scattering, enhancing the accuracy of particle tracking. However, the four GEM detector configuration offers additional advantages. By increasing the number of measurement points, the probability of detecting charged particles passing through the system is significantly enhanced. Considering both the reduction of material effects on multiple scattering and the increased detection efficiency provided by the fourth GEM detector, the four GEM detector setup emerges as the preferable choice. It strikes a balance between minimizing scattering effects and maximizing detection capabilities. By incorporating the additional GEM detector, the system benefits from increased redundancy, reducing the risk of missing charged particles and improving overall detection performance.

These developments contribute to the overall success and scientific significance of the MUSE experiment by ensuring high-quality data analysis and precise detection of particles.

REFERENCES

- [1] R. Gilman, E. J. Downie, G. Ron, S. Strauch, A. Afanasev, A. Akmal, J. Arrington, H. Atac, C. Ayerbe-Gayoso, F. Benmokhtar, N. Benmouna, J. Bernauer, A. Blomberg, W. J. Briscoe, D. Cioffi, E. Cline, D. Cohen, E. O. Cohen, C. Collicott, K. Deiters, J. Diefenbach, B. Dongwi, D. Ghosal, A. Golos-sanov, R. Gothe, D. Higinbotham, D. Hornidge, Y. Ilieva, N. Kalantarians, M. Kohl, B. Krusche, G. Kumbartzki, I. Lavrukhin, L. Li, J. Lichtenstadt, W. Lin, A. Liyanage, W. Lorenzon, K. E. Mesick, Z. E. Meziani, P. Mo-hanmurthy, P. Moran, J. Nazeer, E. Piasetzsky, R. Ransome, R. Raymond, D. Reggiani, P. E. Reimer, A. Richter, T. Rostomyan, P. Roy, A. Sarty, Y. Shamai, N. Sparveris, N. Steinberg, I. Strakovsky, V. Sulkosky, A. S. Tadepalli, and M. Taragin. Technical design report for the paul scherrer in-stitute experiment r-12-01.1: Studying the proton "radius" puzzle with μp elastic scattering, 2017.
- [2] Fabio Sauli. The gas electron multiplier (gem): Operating principles and appli-cations. *Nuclear Instruments and Methods in Physics Research Section A: Accelerators, Spectrometers, Detectors and Associated Equipment*, 805:2–24, 2016. Special Issue in memory of Glenn F. Knoll.
- [3] Fabio Sauli. Gem detectors - 20 years of developments and applications., oct 2016. <https://indico.cern.ch/event/574840/>.
- [4] Marco Villa, Serge Duarte Pinto, Matteo Alfonsi, Ian Brock, Gabriele Croci, Eric David, Rui de Oliveira, Leszek Ropelewski, Hans Taureg, and Miranda van Stenis. Progress on large area gems. *Nuclear Instruments and Methods in Physics Research Section A: Accelerators, Spectrometers, Detectors and Associated Equipment*, 628(1):182–186, 2011. VCI 2010.

- [5] D. Abbaneo et al. Overview of large area triple-gem detectors for the cms forward muon upgrade. *Nuclear Instruments and Methods in Physics Research Section A: Accelerators, Spectrometers, Detectors and Associated Equipment*, 845:298–303, 2017. Proceedings of the Vienna Conference on Instrumentation 2016.
- [6] A. J. Krasznahorkay, M. Csatlós, L. Csige, Z. Gácsi, J. Gulyás, M. Hunyadi, I. Kuti, B.M. Nyakó, L. Stuhl, J. Timár, T.G. Tornyai, Zs. Vajta, T. J. Ketel, and A. Krasznahorkay. Observation of anomalous internal pair creation in ^8Be : A possible indication of a light, neutral boson. *Phys. Rev. Lett.*, 116(4):042501, Jan 2016.
- [7] A. J. Krasznahorkay, M. Csatlos, L. Csige, J. Gulyas, M. Koszta, B. Szihalmi, J. Timar, D. S. Firak, A. Nagy, N. J. Sas, and A. Krasznahorkay. New evidence supporting the existence of the hypothetical x17 particle. arXiv:1910.10459v1 [nucl-ex], 2019.
- [8] The DarkLight Collaboration, E. Cline, R. Corliss, J. C. Bernauer, R. Alarcon, R. Baartman, S. Benson, J. Bessuille, D. Ciarniello, A. Christopher, A. Colon, W. Deconinck, K. Dehmelt, A. Deshpande, J. Dilling, D. H. Dongwi, P. Fisher, T. Gautam, M. Gericke, D. Hasell, M. Hasinoff, E. Ihloff, R. Johnston, R. Kanungo, J. Kelsey, O. Kester, M. Kohl, I. Korover, R. Laxdal, S. Lee, X. Li, C. Ma, A. Mahon, J. W. Martin, R. Milner, M. Moore, P. Moran, J. Nazeer, K. Pachal, T. Patel, T. Planche, M. Rathnayake, M. Suresh, C. Vidal, Y. Wang, and S. Yen. Searching for new physics with darklight at the ariel electron-linac, 2022.
- [9] Michael Staib, Bryant Benson, Kondo Gnanvo, Marcus Hohlmann, and Amilkar Quintero. Thermal stretching of large-area gem foils using an infrared heating method. 04 2011.

- [10] Randolph Pohl, Aldo Antognini, François Nez, Fernando D. Amaro, François Biraben, João M. R. Cardoso, Daniel S. Covita, Andreas Dax, Satish Dhawan, Luis M. P. Fernandes, Adolf Giesen, Thomas Graf, Theodor W. Hänsch, Paul Indelicato, Lucile Julien, Cheng-Yang Kao, Paul Knowles, Eric-Olivier Le Bigot, Yi-Wei Liu, José A. M. Lopes, Livia Ludhova, Cristina M. B. Monteiro, Françoise Mulhauser, Tobias Nebel, Paul Rabinowitz, Joaquim M. F. dos Santos, Lukas A. Schaller, Karsten Schuhmann, Catherine Schwob, David Taqqu, João F. C. A. Veloso, and Franz Kottmann. The size of the proton. *Nature*, 466:213–216, 2010.
- [11] J. C. Bernauer, P. Achenbach, C. Ayerbe Gayoso, R. Böhm, D. Bosnar, L. Debenjak, M. O. Distler, L. Doria, A. Esser, H. Fonvieille, J. M. Friedrich, J. Friedrich, M. Gómez Rodríguez de la Paz, M. Makek, H. Merkel, D. G. Middleton, U. Müller, L. Nungesser, J. Pochodzalla, M. Potokar, S. Sánchez Majos, B. S. Schlimme, S. Širca, Th. Walcher, and M. Weinriefer. High-precision determination of the electric and magnetic form factors of the proton. *Phys. Rev. Lett.*, 105:242001, Dec 2010.
- [12] W. Xiong, A. Gasparian, H. Gao, D. Dutta, M. Khandaker, N. Liyanage, E. Pasyuk, C. Peng, X. Bai, L. Ye, K. Gnanvo, C. Gu, M. Levillain, X. Yan, D. W. Higinbotham, M. Meziane, Z. Ye, K. Adhikari, B. Aljawrneh, H. Bhatt, D. Bhetuwal, J. Brock, V. Burkert, C. Carlin, A. Deur, D. Di, J. Dunne, P. Ekanayaka, L. El-Fassi, B. Emmich, L. Gan, O. Glamazdin, M. L. Kabir, A. Karki, C. Keith, S. Kowalski, V. Lagerquist, I. Larin, T. Liu, A. Liyanage, J. Maxwell, D. Meekins, S. J. Nazeer, V. Nelyubin, H. Nguyen, R. Pedroni, C. Perdrisat, J. Pierce, V. Punjabi, M. Shabestari, A. Shahinyan, R. Silwal, S. Stepanyan, A. Subedi, V. V. Tarasov, N. Ton, Y. Zhang, and Z. W. Zhao. A small proton charge radius from an electron–proton scattering experiment.

Nature, 575:147–150, 2019.

- [13] Aldo Antognini, François Nez, Karsten Schuhmann, Fernando D Amaro, François Biraben, João M R Cardoso, Daniel S Covita, Andreas Dax, Satish Dhawan, Marc Diepold, Luis M P Fernandes, Adolf Giesen, Andrea L Gouvea, Thomas Graf, Theodor W Hänsch, Paul Indelicato, Lucile Julien, Cheng-Yang Kao, Paul Knowles, Franz Kottmann, Eric-Olivier Le Bigot, Yi-Wei Liu, José A M Lopes, Livia Ludhova, Cristina M B Monteiro, Françoise Mulhauser, Tobias Nebel, Paul Rabinowitz, Joaquim M F dos Santos, Lukas A Schaller, Catherine Schwob, David Taqqu, João F C A Veloso, Jan Vogelsang, and Randolph Pohl. Proton structure from the measurement of 2s-2p transition frequencies of muonic hydrogen. *Science*, 339:417–420, 2013.
- [14] Axel Beyer, Lothar Maisenbacher, Arthur Matveev, Randolph Pohl, Ksenia Khabarova, Alexey Grinin, Tobias Lamour, Dylan C. Yost, Theodor W. Hänsch, Nikolai Kolachevsky, and Thomas Udem. The rydberg constant and proton size from atomic hydrogen. *Science*, 358:79–85.
- [15] Hélène Fleurbaey, Sandrine Galtier, Simon Thomas, Marie Bonnaud, Lucile Julien, François Biraben, François Nez, Michel Abgrall, and Jocelyne Guéna. New measurement of the 1s – 3s transition frequency of hydrogen: Contribution to the proton charge radius puzzle. *Phys. Rev. Lett.*, 120:183001, May 2018.
- [16] N. Bezginov, T. Valdez, M. Horbatsch, A. Marsman, A. C. Vutha, and E. A. Hessels. A measurement of the atomic hydrogen lamb shift and the proton charge radius. *Science*, 365(6457):1007–1012, 2019.
- [17] Eite Tiesinga, Peter J. Mohr, David B. Newell, and Barry N. Taylor. CODATA recommended values of the fundamental physical constants: 2018. *Rev. Mod.*

Phys., 93:025010, Jun 2021.

- [18] Ethan Cline. *Understanding the Paul Scherrer Institute's PiM1 beamline for MUSE*. PhD thesis, Rutgers, The State University of New Jersey, 2019.
- [19] Robert Hofstadter. Electron scattering and nuclear structure. *Rev. Mod. Phys.*, 28:214–254, Jul 1956.
- [20] K Nakamura and. Review of particle physics. *Journal of Physics G: Nuclear and Particle Physics*, 37(7A):075021, jul 2010.
- [21] F. Sauli. Gem: A new concept for electron amplification in gas detectors. *Nuclear Instruments and Methods in Physics Research Section A: Accelerators, Spectrometers, Detectors and Associated Equipment*, 386(2):531–534, 1997.
- [22] B. Abi et al. Measurement of the positive muon anomalous magnetic moment to 0.46 ppm. *Phys. Rev. Lett.*, 126:141801, Apr 2021.
- [23] Jonathan L. Feng, Bartosz Fornal, Iftah Galon, Susan Gardner, Jordan Smolinsky, Tim M. P. Tait, and Philip Tanedo. Protophobic fifth-force interpretation of the observed anomaly
$$\frac{m_p}{m_n} - \frac{m_{p'}}{m_{n'}} = \frac{m_p}{m_n} - \frac{m_{p'}}{m_{n'}} + \frac{m_p}{m_n} - \frac{m_{p'}}{m_{n'}} + \dots$$
 transitions. *Physical Review Letters*, 117(7), aug 2016.
- [24] Jonathan L. Feng, Bartosz Fornal, Iftah Galon, Susan Gardner, Jordan Smolinsky, Tim M. P. Tait, and Philip Tanedo. Particle physics models for the 17 MeV anomaly in beryllium nuclear decays. *Physical Review D*, 95(3), feb 2017.

- [25] L. Csige D. Firak J. Gulyás Á. Nagy N. Sas J. Timár T.G. Tornyai A.J. Kraszna-horkay, M. Csatlós. On the $x(17)$ light-particle candidate observed in nuclear transitions. *Acta Physica Polonica B*, 50:675–684, 2019.
- [26] Kondo Gnanvo, Nilanga Liyanage, Vladimir Nelyubin, Kiadtisak Saenboonruang, Seth Sacher, and Bogdan Wojtsekhowski. Large size gem for super bigbite spectrometer (sbs) polarimeter for hall a 12gev program at jlab. *Nuclear Instruments and Methods in Physics Research Section A: Accelerators, Spectrometers, Detectors and Associated Equipment*, 782:77–86, 2015.
- [27] Michael Tytgat, Andrey Marinov, Nikolaos Zaganidis, Y Ban, Jigang Cai, Hsien-Hao Teng, A Mohapatra, T Moulik, Marcello Abbrescia, Anna Colaleo, G. Robertis, F. Loddo, M Maggi, S Nuzzo, Salvatore Tupputi, Luigi Benussi, Stefano Bianco, Davide Piccolo, and Michael Staib. Construction and performance of large-area triple-gem prototypes for future upgrades of the cms forward muon system. *Journal of Instrumentation*, 7, 11 2011.
- [28] H. Gao and M. Vanderhaeghen. The proton charge radius. *Reviews of Modern Physics*, 94(1), jan 2022.
- [29] Peter J. Mohr, Barry N. Taylor, and David B. Newell. Codata recommended values of the fundamental physical constants: 2010. *Rev. Mod. Phys.*, 84:1527–1605, Nov 2012.
- [30] R. Gilman, E. J. Downie, G. Ron, A. Afanasev, J. Arrington, O. Ates, F. Benmokhtar, J. Bernauer, E. Brash, W. J. Briscoe, K. Deiters, J. Diefenbach, C. Djalali, B. Dongwi, L. El Fassi, S. Gilad, K. Gnanvo, R. Gothe, D. Higginbotham, R. Holt, Y. Ilieva, H. Jiang, M. Kohl, G. Kumbartzki, J. Lichtenstadt, A. Liyanage, N. Liyanage, M. Meziane, Z. E. Meziani, D. G. Middleton, P. Monaghan, K. E. Myers, C. Perdrisat, E. Piasetzsky, V. Punjabi, R. Ran-

- some, D. Reggiani, P. Reimer, A. Richter, A. Sarty, E. Schulte, Y. Shamai, N. Sparveris, S. Strauch, V. Sulkosky, A. S. Tadepalli, M. Taragin, and L. Weinstein. Studying the proton "radius" puzzle with μp elastic scattering, 2013.
- [31] Ethan Cline, Jan Bernauer, Evangeline J. Downie, and Ronald Gilman. MUSE: The MUon Scattering Experiment. *SciPost Phys. Proc.*, page 023, 2021.
- [32] A. Gasparian, H. Gao, D. Dutta, N. Liyanage, E. Pasyuk, D. W. Higinbotham, C. Peng, K. Gnanvo, W. Xiong, X. Bai, and the PRad collaboration. Prad-ii: A new upgraded high precision measurement of the proton charge radius, 2020.
- [33] E. Cline, W. Lin, P. Roy, P. E. Reimer, K. E. Mesick, A. Akmal, A. Alie, H. Atac, A. Atencio, C. Ayerbe Gayoso, N. Benmouna, F. Benmokhtar, J. C. Bernauer, W. J. Briscoe, J. Campbell, D. Cohen, E. O. Cohen, C. Collicott, K. Deiters, S. Dogra, E. Downie, I. P. Fernando, A. Flannery, T. Gautam, D. Ghosal, R. Gilman, A. Golossanov, B. F. Halter, J. Hirschman, Y. Ilieva, M. Kim, M. Kohl, B. Krusche, I. Lavrukhin, L. Li, B. Liang-Gilman, A. Liyanage, W. Lorenzon, P. Mohanmurthy, R. Mokal, P. Moran, S. J. Nazeer, P. Or, T. Patel, E. Piasetzky, T. Rauber, R. S. Raymond, D. Reggiani, H. Reid, G. Ron, E. Rooney, T. Rostomyan, M. Schwarz, A. Sneath, P. G. Solazzo, N. Sparveris, N. Steinberg, S. Strauch, V. Sulkosky, and N. Wuerfel. Characterization of muon and electron beams in the paul scherrer institute pim1 channel for the muse experiment. *Phys. Rev. C*, 105:055201, May 2022.
- [34] T. Rostomyan, E. Cline, I. Lavrukhin, H. Atac, A. Atencio, J.C. Bernauer, W.J. Briscoe, D. Cohen, E.O. Cohen, C. Collicott, K. Deiters, S. Dogra, E. Downie, W. Erni, I.P. Fernando, A. Flannery, T. Gautam, D. Ghosal, R. Gilman, A. Golossanov, J. Hirschman, M. Kim, M. Kohl, B. Krusche, L. Li, W. Lin, A. Liyanage, W. Lorenzon, P. Mohanmurthy, J. Nazeer, P. Or, T. Patel,

- E. Piasetzky, N. Pilip, H. Reid, P.E. Reimer, G. Ron, E. Rooney, Y. Shamaï, P. Solazzo, S. Strauch, D. Vidne, and N. Wuerfel. Timing detectors with SiPM read-out for the MUSE experiment at PSI. *Nuclear Instruments and Methods in Physics Research Section A: Accelerators, Spectrometers, Detectors and Associated Equipment*, 986:164801, jan 2021.
- [35] R. Milner et al. The OLYMPUS experiment. *Nuclear Instruments and Methods in Physics Research Section A: Accelerators, Spectrometers, Detectors and Associated Equipment*, 741:1–17, mar 2014.
- [36] P. Roy, S. Corsetti, M. Dimond, M. Kim, L. Le Pottier, W. Lorenzon, R. Raymond, H. Reid, N. Steinberg, N. Wuerfel, K. Deiters, W.J. Briscoe, A. Golosanov, and T. Rostomyan. A liquid hydrogen target for the MUSE experiment at PSI. *Nuclear Instruments and Methods in Physics Research Section A: Accelerators, Spectrometers, Detectors and Associated Equipment*, 949:162874, jan 2020.
- [37] M. F. M. Lutz et al. Physics performance report for panda: Strong interaction studies with antiprotons, 2009.

VITA

Sahara Jesmin Mohammed Prem Nazeer

sarajesmin@gmail.com

Education

Doctor of Philosophy (August 2023),

Physics,

Hampton University, VA

Bachelor of Science in Physics (May 2014),

Physics,

University of Peradeniya, Sri Lanka

Professional Experience

Research Assistant (2014-2023)

Hampton University, Hampton, VA

Temporary Demonstrator (2013-2014)

Faculty of Science, University of Peradeniya, Sri Lanka

Honors and Awards

- JSA Graduate Student Fellowship - (2020-2021)
- DOE Office of Science Graduate Student Research (SCGSR) Fellowship - (2018-2019)
- JSA Graduate Student Travel Award - Oct 2018

Publications

- Ethan Cline, *et al.* Searching for new physics with DarkLight at the ARIEL electron-Linac. *Journal of Physics Conference Series* (Dec 2022)
- Ethan Cline, *et al.* Characterization of muon and electron beams in the Paul Scherrer Institute PiM1 channel for the MUSE experiment. *Phys. Rev. C* 105, 055201 (May 2022)
- Lee S., Corliss R., Friscic I. *et al.* Design and operation of a windowless gas target internal to a solenoidal magnet for use with a megawatt electron beam. *Nuclear Instruments and Methods in Physics, Research Section A939*, 46-54 (2019).
- Xiong, W., *et al.* A small proton charge radius from an electron– proton scattering experiment. *Nature* 575, 147-150 (2019).
- Liyanage, M. Kohl, J. Nazeer, and T. Patel, “Development of gem detectors at hampton university,” (2018). <https://arxiv.org/abs/1803.00132>

Presentations

- ”Efficiency study of GEM detectors for MUSE”. Oral presentation – APS Division of Nuclear Physics April Meeting – Virtual (April 17-20, 2020)
- ”GEM data analysis for the MUSE experiment at PSI” Oral presentation – APS Division of Nuclear Physics Fall Meeting – Virtual (Oct 29- Nov 1, 2020)
- ”A Novel Set of Gas Electron Multiplier Detectors” Oral presentation – APS Division of Nuclear Physics April Meeting – Virtual (April 28-21, 2020)
- ”GEM Detectors for DarkLight Phase 1(c)” – Oral presentation APS Division of Nuclear Physics Fall Meeting – Hawaii (Oct 23-27, 2018)
- ”GEM Detectors for the DarkLight Phase1 Experiment” Oral presentation - APS Division of Nuclear Physics Fall Meeting – Pittsburgh, PA (Oct 25-18, 2017)